

Raman Measurements of Optical Phonon Scattering in Sub-Micron $\text{Si}_{1-x}\text{Ge}_x$ Thin Films

A Dissertation Presented to the
Faculty of the School of Engineering and Applied Science
University of Virginia

In Partial Fulfillment
of the Requirements for the Degree of
Doctor of Philosophy
Mechanical and Aerospace Engineering

Christopher B. Saltontall II
May 2016

APPROVAL SHEET

The dissertation is submitted in partial fulfillment of the
requirements for the degree of

Doctor of Philosophy in Mechanical and Aerospace Engineering

Christopher B. Saltonstall II

This dissertation has been read and approved by the Examining Committee:

Pamela M. Norris, Advisor

Patrick E. Hopkins, Chairman

Jerrold A. Floro

Petra Reinke

Kieth A. Williams

Thomas E. Beechem

Accepted for the School of Engineering and Applied Science:

Pamela M. Norris, Dean
School of Engineering and Applied Science

Abstract

Phonon thermal conductivity is often modeled using the phonon gas model (PGM), which assumes that all normal modes of a material can be described by plane waves (i.e. delocalized and propagating). However, as the translational symmetry of a crystal is broken through the introduction of impurities, dislocation or nanoscaling, the normal modes depart from plane wave-like nature. Allen and Feldman first developed the theory for non-plane wave modes when modeling thermal conductivity showing that with increasing frequency modes become increasingly localized. Localizing modes limits the ability of vibrations to transmit energy through the material, which leads to a reduction of overall measured thermal conductivity. In addition to changing the nature of the vibrational modes in a material, breaking the translation symmetry creates scattering sites that further reduces vibrational thermal conductivity. It is difficult to separate the convoluted effects of scattering and localization in experimental thermal conductivity measurements since most investigations employ the PGM, which only accounts for phonon scattering. The next generation of models to predict thermal transport in disordered and nanoscaled materials will hinge on a detailed understanding of both the nature and behavior of vibrations. Raman spectroscopy is uniquely equipped to study vibrational nature (localization) and behavior (scattering) since they are directly related to the linewidth and asymmetry of the spectral peak of the Raman active mode, respectively. Therefore, Raman spectroscopy is employed to monitor the influence of alloying, nano-scaling and crystal imperfections/dislocations on temperature dependent scattering and localization. While the information gleaned from the optical Raman modes cannot be directly related to thermal conductivities it provides insight into how various material properties influence the combined scattering and localization of vibrations. It is found that breaking the periodicity of a crystal through alloying, nanoscaling or dislocations influences scattering of vibrations more than simply through temperature independent scattering sites. Additionally, breaking translational symmetry of the crystal leads to localization of the modes which is temperature dependent.

This dissertation is dedicated to all of those in my life who supported me through this endeavor. Especially, Harley.

Acknowledgements

One of the most difficult skills in life, that is key to success in graduate school, is the perseverance to overcome obstacles. Those obstacles can come in many forms such as broken lasers, confusing data or a scientific disagreement with your advisor, but all require an intellectual ferocity in order to persevere. However, it takes time in a graduate program to learn how to be patient with the wheel spinning that comes before success. I am grateful to for all of those who generously donated their time and energy helping me learn this invaluable skill.

Thank you Dr. Hopkins, Dr. Reinke, Dr. Floro, Dr. Williams and Dr. Beechem for taking the time to serve on my doctoral committee. Dr. Hopkins took a chance after meeting me for only a few days to me invite to serve as an intern under him at Sandia National Laboratories. There he taught me many things and introduced me to many people (Dr. Beechem, Dr. Serrano, Dr. Peikos and Dr. Rader) who have shaped my knowledge, skills and career. His influence continued as he served as my co-advisor at UVA. I would especially like to thank Dr. Beechem who has regularly worked with me over the past few years as an unofficial advisor and soon to be post-doctoral employer. I must also thank Dr. Reinke, Dr. Floro and Dr. Williams for their insightful discussions of material science and Raman spectroscopy. I would also like to thank Dr. Norris, for seeing my potential as an undergraduate student and hiring me into her lab so many years ago.

While these mentors were instrumental in directing my career, the story of my tenure at UVA was heavily shaped by the day to day support of my lab-mates. My success could not have come with out the comradery of Matthew Bauer, Casey Bauer, Nam Le, Leighann Larkin and Christina Pappas. Matthew and Casey served to set the bar high for success, work ethic and self-improvement, which has continuously motivated me to always work towards a better version of myself. I would also like to thank Nam for his patience and thoughtfulness during our regular impromptu Gedankens. Leighann was integral in the success of this dissertation through XRD measurements of my samples and distracting conversations during much needed breaks. Jatin Amatya also deserves thanks for growing the samples used in this dissertation.

Finally, my family must be showered with gratitude as all successes in my life were only achievable through their support. My parents have always been behind me during each of my many mistakes to prevent me from falling. They also always encouraged me to set my goals as high as I could dream. Robert, my brother, who through his quiet thoughtful presence always served as a reminder to remain grounded. And while they do not share my blood, my warmest thanks go out to my brothers Chris Brown and Mike Coles. They have always been the best friends I could ask for in the best and worst of times.

Nomenclature

$2w_0$	Laser spot diameter
α	Absorption coefficient
$\Delta\epsilon$	Energy uncertainty
Δq	Wavevector uncertainty
δ_p	Penetration depth
ϵ_1	Real component of dielectric function
ϵ_2	Imaginary component of dielectric function
$\frac{1}{\tau}$	Scattering rate
Γ	Raman peak FWHM
Γ -point	Brillioun zone center
Γ^3	Klemens 3-phonon decay model for the Raman linewidth
Γ_0^3	Temperature dependent component of the linewidth for Klemens 3-phonon decay model
Γ^4	4-phonon decay model
Γ_0^4	4-phonon temperature dependent component of the Raman linewidth
Γ_0	Linewidth at 0 cm^{-1} /px resolution
Γ_0^I	Temperature independent component of Raman linewidth
Γ_G	Gaussian component of the Voigt linewidth
Γ_L	Lorentzian component of the Voigt linewidth
Γ_S	Laser spot FWHM
\hbar	Planks constant divided by 2π
κ	Imaginary component of refraction

λ	Wavelength
λ_L	Laser wavelength
∇T	Temperature gradient
ω	Frequency
ω'	Voigt Function integration variable
$\omega(0)$	Optical phonon frequency at Brillouin zone center
$\omega(q)$	Phonon dispersion relation
ω_0	Raman peak position
ω_n	Frequency of the n^{th} normal vibrational mode
ω_{ref}	Reference frequency
ω_{SG}	Si-Ge peak frequency of the SiGe alloy
ω_{SiGe}	Si ₅₀ Ge ₅₀ peak position at room temperature
ω_{Si}	Si peak position at room temperature
ω_{SS}	Si-Si peak frequency of the SiGe alloy
τ	Scattering time
τ_A	mklapp scattering time
τ_B	Boundary scattering time
τ_I	Mass impurity scattering time
τ_U	Umklapp scattering time
θ	Lens/objective collection angle
$\tilde{\epsilon}$	Complex dielectric function
\tilde{n}	Complex index of refraction
ε	Material strain
A	Fit parameter
a	Interatomic spacing
B	Fit parameter
C	Fit parameter

$C(q)$	PCM Fourier Coefficient
C_v	Vibrational specific heat
D	Fit parameter
f	Focal length
G	Gaussian function
h	Planck constant
I_0	Raman peak intensity
I_F	Fano function intensity
I_R	Raman penetration intensity
I_V	Intensity of the Voigt function
I_{BL}	Beer-Lambert Law
I_{PCM}	Phonon Confinement Model intensity
I_{Sim}	Simulated Raman spectrum
k	Vibrational thermal conductivity
k_B	Boltzmann constant
k_{eff}	Effective spring constant
L	Lorentzian function
L_a	Phonon correlation length
l_u	Unit cell length
m	Atomic mass
m_{red}	Reduced mass
N	Number of atoms
n	Real Component of Index of Refraction
N_{base}	Baseline noise
N_{peak}	Peak noise
p	Quantum momentum
Q	Fano asymmetry parameter

q	Phonon wavevector
q_T	Thermal flux
R	Spectrometer resolution
r	Material relaxation
$randn$	Normal distribution random number function
t	Time
T_{ref}	Reference temperature
u	Atomic displacement
v	Phonon group velocity
v_p	Phonon phase velocity
v_s	Sound speed
x	Molar fraction of Ge
z	Film depth
AFM	Atomic force microscopy
CCD	Charge couple device
CNT	Carbon nanotubes
CVD	Chemical vapor deposition
CWP	Cahill-Watson-Pohl
DOF	Depth of field
FWHM	Full width at half maximum
MBE	Molecular beam epitaxy
MEM	Micro-electromechanical systems
NA	Numerical aperture
ND	Neutral density filter
PCM	Phonon Confinement Model
PGM	Phonon Gas Model
QCL	Quantum cascade laser

RBM Radial breathing mode
RPI Relative peak intensity
STM Scanning tunneling microscopy
TED Thermoelectric device

Contents

Nomenclature	iii
1 Introduction	1
1.1 Background	1
1.2 Engineering Applications	4
1.3 Objectives	7
2 Thermal Transport: from the Bulk Crystal to the Disordered Nano-structure	11
2.1 Bulk Crystal	11
2.1.1 Phonons	12
2.1.2 Phonon Gas Model	14
2.1.3 Phonon Scattering	15
2.2 Breaking Periodicity	20
2.2.1 Nanoscaling	21
2.2.2 Disorder	23
3 Raman Spectroscopy	29
3.1 Raman Scattering	29
3.1.1 Disorder and Nanoscaling	32
3.1.2 Resonant Raman	35
3.2 Material Characterization	36
3.2.1 Peak Position	36
3.2.2 Linewidth	39
3.3 Fitting	41
3.4 Raman Experiments	44
3.4.1 Renishaw InVia Spectrometer	45
3.4.2 Raman Penetration Depth	48
3.4.3 Confocality	51
4 Limits of Phonon Linewidth Measurements	54
4.1 Motivation	54
4.2 Experiment	58
4.3 Modeling the Experiment	62
4.3.1 Experimental Theory	62

4.3.2	One Peak (Si)	64
4.4	Results	70
4.4.1	Two Peak (SiGe)	70
4.4.2	Pixelation Error	73
4.5	Conclusions	76
5	Laser Heating of SiGe Alloys	77
5.1	Motivation	77
5.2	Experimental Investigations	79
5.2.1	Fano Resonance	80
5.2.2	Laser Heating	81
5.3	Modeling Laser Heating	90
5.3.1	Model System	90
5.3.2	Laser Heating	92
5.3.3	Solution	92
5.3.4	Raman Simulation	93
5.3.5	Results	94
5.4	Conclusions	98
6	Phonon Scattering in SiGe Alloys	100
6.1	Introduction	100
6.2	Experimental	103
6.2.1	Samples	103
6.2.2	XRD Characterization	105
6.2.3	Raman Measurements	106
6.3	Results	108
6.3.1	Alloy and Dislocation Disorder	109
6.3.2	Size Effects	113
6.3.3	Localization Temperature Trends	116
6.4	Conclusions	119
7	Conclusions	122
7.1	Summary of Conclusions	122
7.2	Suggested Future Studies	125
	References	129

List of Figures

2.1	Silicon dispersion along several high symmetry direction in the Brillouin zone[1]. The density of vibrational states calculated from the dispersion is shown in the right most panel.	12
2.2	(a) (left) Hypothetical 2-dimensional crystal. Dashed lines represent bisections of lines between center atom and nearest neighbors. Red line outlines boundary of unit cell created by bisections. (b) (right) Corresponding lattice in reciprocal space and resulting Brillouin zone in red.	13
2.3	Diagram of various phonon scattering types with corresponding model equations used in the phonon gas model.	16
2.4	Fourier transform of atomic displacements in wavepacket simulation before scattering at interface and after with harmonic or anharmonic potentials at the interface. Anharmonicity causes the incident phonon to split into two phonons after reflecting at the interface indicating inelastic scattering processes, which in turn implies a temperature dependent scattering event.	20
2.5	Diagram of different material phases illustrating spatial and compositional order and disorder.	24
2.6	Thermal conductivity of crystalline and amorphous silicon dioxide and compositionally disordered SiGe alloys[2–4]. Amorphous SiO ₂ shows monotonic glass-like thermal conductivity trends, while the crystalline phase shows typical arching crystalline temperature trends. The SiGe alloys illustrate the flattening effect of alloying.	25
3.1	Energy of an electron during the three spontaneous Raman processes. a) Rayleigh scattering involves the absorption of an photon by an electron to a virtual state (VS), then the spontaneous decay back to ground state yielding an elastically scattered photon. Stokes (b) and anti-Stokes (c) processes involve inelastic scattering of the electron with the vibrational system yielding an energy shifted photon.	30
3.2	(a) Typical Raman spectra of silicon showing both the Stokes and anti-Stokes peaks (not to scale). (b) Temperature dependence of the Stokes peak of silicon. As temperature increases the peak intensity, I_0 , and peak position, ν_0 , decrease while the line width (FWHM), Γ increases.	31

3.3	Raman scattering efficiency versus Ge fraction and wavelength[5]. As the Ge fraction increases, the peak efficiency shifts towards longer wavelengths indicating a narrower band gap.	36
3.4	(a)(left) Harmonic and anharmonic Lennard-Jones potentials with average atomic position (dashed). (b) (right) Frequency vs atomic displacement showing how frequency softens as amplitude of atomic vibration (temperature) increases.	37
3.5	Internal diagram of Renishaw InVia Raman microscope.	45
3.6	(a) Diagram of confocal Raman setup with objective lens (b) and CCD camera chip. The entrance slit of the spectrometer and CCD chip filters out Raman scattered light generated from areas away from the objective focal point.	51
4.1	As the angle at which light is dispersed by the grating increases, the spectral resolution of the spectrometer increases because there are fewer wavelengths per pixel.	55
4.2	(a) The Raman spectra of a 39 nm $\text{Si}_{80}\text{Ge}_{20}$ thin film on Si taken using the 405 nm laser with three grating combinations are shown. We can see that as the resolution of the grating increases the peaks narrow and become more distinct. (b) The Raman spectra of 39 nm $\text{Si}_{80}\text{Ge}_{20}$ thin film on Si taken using the 405, 488 and 514 nm lasers with the 3000 g/mm (-1) grating are shown. As the wavelength decreases, the spatial resolution increases by more than an order of magnitude but the spectral resolution is reduced by a factor of 3.	56
4.3	Change of N/S ratio with changing integration time using Si, 488 nm laser, 50x objective and various grating conditions.	61
4.4	(a) Total FWHM of silicon as a function of spectrometer resolution when using the 405, 488 and 514 nm lasers. (b) Corresponding uncertainties in the FWHM of Si showing how worsened resolution leads to larger uncertainties.	65
4.5	Gaussian and Lorentzian linewidth of simulated and experimental silicon Raman spectra versus resolution.	66
4.6	Simulated and experimental noise of the Si Raman spectrum.	67
4.7	(a) Contour plot of the standard deviation of the Si Lorentzian linewidth vs resolution and noise level. Markers indicate position on the surface of experiment, 405 nm (diamonds), 488 nm (squares) and 514 nm (circles). The uncertainties of the experiment (simulation) are presented next to the markers. (b) Cross section of the contour plot in the noise fraction direction at various values of resolution. (c) Cross section of the contour plot in the resolution direction at various values of noise fraction. Dashed lines show the minimums of the noise and resolution for the Raman system at UVA.	69

4.8	(a) Contour plot of the standard deviation of the SiGe Lorentzian linewidth vs resolution and RPI. Markers indicate position on the surface of experiment, 40 nm film (diamonds), 90 nm film (squares) and 210 nm (triangles). The color indicates the laser wavelength used, 514 nm (green), 488 nm (blue). The uncertainties of the experiment (simulation) are presented next to the markers in units of cm^{-1} . (b) Cross section of the contour plot in the resolution direction at various values of resolution. (c) Cross section of the contour plot in the RPI direction at various values of noise fraction.	71
4.9	(a) Normalized fit FWHM versus normalized resolution showing how resolution biases the fit of the Lorentzian linewidth. The fit FWHM and resolution were normalized by the actual FWHM of the simulation input peak. (b) Two spectra (markers) at high resolution with pixels located at different point on the peaks and their corresponding fit (lines) (c) Two spectra (markers) with pixels located at different locations on the peak at low resolution and their corresponding fits (lines).	74
5.1	Raman spectra of Sample 7, 25% Ge 210 nm thick, using 488 nm laser at various laser powers.	79
5.2	Raman spectra of Sample 7, 25% Ge 210 nm thick, using 405, 488 and 514 nm laser wavelengths at very low laser power.	80
5.3	Raman spectra of (a) 40 nm and (b) 210 nm $\text{Si}_{75}\text{Ge}_{25}$ films at various laser powers. Using the peak position as a temperature metric, the temperature rise of the Si substrate and alloy film are plotted versus laser power for the (c) 40 nm and (d) 210 nm films.	83
5.4	Raman spectra of the Si-Si peak in SiGe alloys with various Ge content and at various laser power.	85
5.5	Fit results of the Si-Si peak.	86
5.6	Peak intensity of the Si (100) Raman spectrum as a function of polarization relative to the (100) crystal direction.	88
5.7	Raman spectra of a 210 nm $\text{Si}_{75}\text{Ge}_{25}$ thin film at various polarizations relative to the crystal orientation for the 405 nm and 488 nm laser at high laser power, 2 and 8 mW, respectively.	89
5.8	FEA model system for laser heating thin film (<u>not</u> drawn to scale). A cylinder with radius $10\mu\text{m}$ and thickness 210 nm was irradiated with a $2\mu\text{m}$ laser beam. Due to the radial symmetry, the system was constructed in 2-dimensions, r and z.	90
5.9	(solid) Raman spectra of the Si-Si peak in SiGe alloys at various temperatures using the 405 nm laser. (dashed) The fit of the peak using a Fano line shape is also shown at each temperature.	91
5.10	Left column plots simulated Raman spectra for various Ge contents at various laser powers. The right column plots the experimental analog.	95
5.11	Temperature profile of 210 nm thick $\text{Si}_{75}\text{Ge}_{25}$ film heated by 52mW 488 nm laser (compare to 13 mW experiment).	96

5.12	Results of the simulated (solid lines) and experimental (diamonds and circles) 488 nm laser heating of 210 nm SiGe films. (a) The temperature profile at various depths of the $x = 0.25$ SiGe film irradiated with 13 mW (52 mW simulated). (b) Peak position of two peak Fano fits to the heated experimental and simulated spectra at various laser powers. (c) Maximum temperature when irradiated at various laser powers. (d) Temperature of experimental and simulated films based on peak position fits.	97
6.1	Diagram of the four sample series investigated in this study (sample numbers in parenthesis) which are also described in Tables 6.1 and 6.2. The dislocation density is qualitatively described by “None”, “Few”, “Some” and “Many”.	104
6.2	XRD reflections of Sample 3 ($d = 202$ nm, $x = 0.18$) and Sample 8 ($d = 210$ nm, $x = 0.19$) in the (a) 004 and (b) 224 directions. These results show the strain relaxation from dislocations in the CVD grown films (Sample 3).	106
6.3	Diagram of the two sample series used to investigate the effects of disorder on scattering rates and localization (sample numbers in parenthesis). The text color corresponds to the data color in the figures in this section.	110
6.4	Room temperature measurements of the Raman (a) linewidth and (b) asymmetry for alloy and dislocation series diagramed in Fig. 6.3.	110
6.5	Temperature (a) independent, Γ_0^I , and (b) dependent, Γ_0^3 , components of the scattering rate extracted from temperature dependent linewidth measurements of the alloy and dislocation series, Fig. 6.3, using the Klemens 3-phonon decay model, Eq. 3.9. Dashed line are the results of the fit for bulk Si(100).	112
6.6	Diagram of the two sample series used to investigate the effects of nanoscaling on scattering rates and localization (sample numbers in parenthesis). The size and dislocation series was grown using CVD while the pure size effects series was grown using MBE. The text color corresponds to the data color in the figures in this section.	114
6.7	Room temperature measurements of the Raman (a) linewidth and (b) asymmetry for size effects series diagramed in Fig. 6.6.	114
6.8	Temperature (a) independent, Γ_0^I , and (b) dependent, Γ_0^3 , components of the scattering rate extracted from temperature dependent linewidth measurements of the size effects series, Fig. 6.6, using the Klemens 3-phonon decay model, Eq. 3.9. Dashed lines are the results of the fit for bulk Si(100).	116
6.9	Localization as a function of temperature for the (a) MBE size effects series, Fig. 6.6, (b) dislocation series, Fig. 6.3, (c) alloy series, Fig. 6.3, and (d) the CVD size and dislocation effects series, Fig.6.6.	117

List of Tables

2.1	Four regimes of phonon transport at various scales. As material scales, d , decrease, boundary scattering and dispersion modifications influence thermal transport.	22
3.1	Penetration depth and complex index of refraction for Si and Si ₈₀ Ge ₂₀ at various wavelengths[6, 7].	50
3.2	Percent of Raman light generated by a cumulative depth at various wavelengths in Si ₈₀ Ge ₂₀ calculated using Eq. 3.18.	50
4.1	The spectral resolutions, in cm ⁻¹ /pix, of three lasers with three different grating types, where the number in parenthesis is the order the grating is operated in. The relative Raman intensities of the 40 nm thin film Si ₇₅ Ge ₂₅ (Sample 5) alloy peak and Si substrate peak is included as an indication of spatial resolution.	57
4.2	Combinations of laser wavelength, grating and sample thickness used for linewidth uncertainty measurements of Si and Si ₇₅ Ge ₂₅ with thicknesses 20, 90 and 210 nm (Samples 5-7). X symbolizes laser wavelength and grating combinations that will not be collected. ✓ indicates laser and grating combinations for which data was collected and the number in parenthesis is the RPI.	59
4.3	Uncertainties of fit experimental and simulated Si fit parameters for the 514 nm 1800 g/mm case.	68
6.1	This table summarizes the samples that will be used in this study. The parenthesis next to the growth method (CVD or MBE) indicate the growth temperature while x indicates the fractional Ge concentration of the alloy film. Each number in the table is the sample number which is used to identify each sample for the discussion.	103
6.2	This table summarizes material properties, film thickness (d), Ge fraction (x) and percent strain relaxation (r). Samples above the dashed line were grown using CVD and below using MBE. The average spacing of dislocations, σ_{dis} , and Ge atoms, σ_{Ge} , is also shown.	106

Chapter 1

Introduction

1.1 Background

In a book titled "The Next Big Thing is Really Small", Jack Uldrich and Dev Newberry discuss how nanotechnology will change the future of business and technology[8]. In this book, they predict that,

"Over the next ten years, the fields of chemistry, physics, material sciences, biology, and computational sciences will converge in a way that will define nanotechnology and impact almost every industry, including computers, semiconductors, pharmaceuticals, defense, health care, communications, transportation, energy, environmental sciences, entertainment, chemicals, and manufacturing. Previously distinct disciplines will also combine: medicine and engineering, law and science, art and physics, etc. This merging will result in developments that are not simply evolutionary; they will be revolutionary."

The nanotechnology that they were referring to is technology developed by manipulating and arranging materials on the atomic scale. This ability will clearly be advantageous for nearly every scientific field and will require the combined effort of each of these fields to implement. For example, advances in nanotechnology for

the medical field will require the fundamental knowledge of physicists, while advances in electrical engineering will require the nano-growth techniques developed by the material scientist. This effect of blurring scientific fields is already being seen in mechanical engineering, among others. Heat transfer, which has traditionally been a macroscopic science entrenched in mechanical engineering, has evolved into the study of fundamental heat particles (phonons) on the nanoscale, which has created a subculture within mechanical engineering made up of scientists with a wide range of backgrounds, from physics and chemistry to material science and mechanical engineering.

In the nanoscale thermal transport field, the fundamental goal is to understand and control thermal energy at the nanoscale. This is particularly important for micro-electronics which make up the majority of consumer electronics, such as smart phones and PCs. Micro-electronics are designed to ideally operate under a stable thermal environment and within a particular temperature range, necessitating the thermal conductivity to be tuned along with the electronic properties during development. Unfortunately, however, thermal conductivity is currently only tunable up to 6 orders of magnitude at room temperature while electrical conductivity is tunable over 20 orders of magnitude.[9] Additionally, nano-structuring the materials that compose the device introduces additional effects for which macroscopic models of thermal conductivity cannot account.

An example of a material that is ubiquitously used in micro-electronics and has the advantage of highly tunable electrical conductivity, but suffers from low thermal conductivity is the silicon-germanium (SiGe) alloy. The first solid state transistors were fabricated using Si, but by alloying Si with Ge, the electron mobility could be strongly enhanced resulting in SiGe alloys replacing Si as the gate in many transistors[10]. However, the relatively low thermal conductivity of SiGe leads to a significant impediment to thermal abatement near where the majority of heat in the transistor is generated. Additionally, as transistor sizes are pushed smaller by a

drive for higher performance micro electronics, the SiGe layers have reached length scales in the 10's of nanometers, adding complication to device modeling.

On the macro-scale, thermal conductivity obeys the Fourier Law, which states that the flux, q_T , applied through a material is proportional to the temperature gradient, ∇T , through the material,

$$q_T = -k\nabla T, \quad (1.1)$$

where the proportionality constant is the thermal conductivity, k [9, 11]. In bulk highly crystalline material systems, the thermal conductivity is often modeled using the phonon gas model (PGM), which treats thermal energy carriers as a gas of particles, phonons. The thermal conductivity is then a function of the energy each particle carries, specific heat (C_v), how fast the particle moves, velocity (v), and the frequency at which it scatters with obstructions, scattering rate ($1/\tau$),

$$k = \frac{1}{3} \int_0^{\omega_{max}} C v^2 \tau d\omega, \quad (1.2)$$

where the integration is over all frequencies, ω . The major assumption of the PGM is that the normal modes of the system can be described mathematically by plane waves, so that the wave vector and velocity are well defined and specific heat and velocity can be extracted from the dispersion relation. Furthermore, it often assumes that imperfections in the periodicity of the lattice can be treated as perturbations accounted for by an additional temperature independent scattering rate term. This assumption is accurate for small perturbations from periodicity. However, as the perturbations become large as in the case of amorphous materials, disordered alloys or nano-scaled materials, the normal modes of the system can no longer be accurately described by plane waves and so the dispersion, wavevectors and group velocities become ambiguous[12]. In order to model systems with such a departure from periodicity, we must develop an understanding for how breaking of periodicity (e.g., impurities, defects, nano-scaling) influences both the plane wave

nature and scattering *behavior* of vibrations.

In the late nineties, Allen and Feldman published their seminal work presenting the first theoretical attempt at accounting for a change in both the nature and behavior of vibrations when modeling thermal conductivity in amorphous silicon[12, 13]. Since then, several studies have built on their initial findings [14–17], but the vast majority of these investigations are theoretical or computational. The reason for this is that experimental thermal conductivity investigations measure the net effect of both changes in nature and behavior of phonons. The results are then modeled using the PGM which lumps any change in thermal conductivity caused by changing material properties into a change in the temperature independent scattering rates. By not being able to separately measure the individual changes to the nature and behavior of vibrations, the effect cannot be deconvolved.

This dissertation aims to advance the understanding of how strong perturbations to the periodicity of a material influence both the nature and behavior of the vibrational system by circumventing the PGM and directly probing vibrational scattering rates and measuring the vibrational departure from plane wave nature, simultaneously, using Raman spectroscopy. The remainder of this chapter will provide a brief overview of microelectronic systems which can be advanced through a better understanding of nano-scale thermal transport and will conclude by outlining the dissertation work in subsequent chapters.

1.2 Engineering Applications

Modern electronic devices are engineered such that they perform a specific operational purpose. They meet this purpose by manipulating the flow of pertinent energy carriers through material layers and across interfaces. As we push the limits of miniaturization in these devices, the interface density increases and material layers reach nano-scale thicknesses. No matter the energy carrier, this increase in

interface density increases the scattering events of the carrier outside the coherent regime. At the same time, nano-scaling leads to film thicknesses near the mean free paths of carriers causing significant changes in the material properties when compared to bulk.

The most pressing motivation for understanding the effect of nano-scaling on energy carriers is the need to keep pace with nanoscaling and increasing transistor densities in microelectronics[18, 19]. The consequence of increased transistor densities is increased power density, which in turn results in an unwanted temperature rise due to waste heat. Since a device's lifetime and reliability are significantly reduced for even small increases in operational temperature, it is imperative that this thermal energy is properly abated[20, 21]. In the past, thermal abatement was an after thought during the design process and was left to a thermal engineer to manage through secondary measures such as heat sinks. However, as transistors have reached nanoscale sizes, power densities have reached limits where the efficacy of secondary measures is limited, which has led to the inability to keep pace with Moore's Law[22]. This has motivated device engineers to begin accounting for thermal transport in device design.

The main issue with modeling nanoscaled systems is that Fourier's law and the PGM are no longer applicable[9, 23]. As material layers in transistors reach length scales comparable to the mean free path of energy carriers, interfaces between material layers become the dominant scattering mechanism and thus the major contributor to thermal resistance. Additionally, nano-structuring breaks the periodicity of crystals resulting in vibrations that are no longer plane wave-like. The plane wave nature of the modes is further diminished when materials used for device layers have large degrees of disorder, such as in an alloy or amorphous material. Since the PGM is based on a planewave description of phonons, the nanoscaling and disorder reduces the accuracy of the PGM for predicting thermal transport through devices.

Another device that is limited due to thermal concerns is the THz quantum

cascade laser. The quantum cascade laser (QCL) is a major advance in laser technology which has pushed the limits of coherent single wavelengths far into the infrared region. QCLs are particularly advantageous in the field of IR spectroscopy, where a finger print region used for identification of compounds exists[24]. Traditional IR spectroscopy methods are based on a non-coherent broad band light source that requires the data to be post-processed with Fourier transform techniques. A coherent light source allows for remote sensing while the single wavelength source removes the need for post processing. These advantages open opportunities for remote sensing applications such as measuring atmospheric compositions and monitoring environments for harmful compounds. However, the major limitation of QCLs is that they generate significant levels of waste heat and require complex cryogenic cooling systems for operation.

Quantum cascade lasers are based on electrons cascading down a series of discrete electron energy levels contained in a series of quantum wells separated by tunneling layers, which form a superlattice[25–28]. The laser operates by applying a bias across the device which injects electrons into the active region. Once an electron enters the first quantum well it decays from the excited state to the ground energy level emitting a photon. Then through a resonant tunneling process, the ground state electron moves through the boundary layer into the next quantum well where it will repeat the process. The resonant tunneling process is mediated by the emission of an optical phonon into the boundary region, which generates waste heat from a large non-equilibrium population of optical phonons[27, 29, 30]. Optical phonons are particularly deleterious because of their low group velocities and high scattering rates, which make it difficult to remove the resulting thermal energy effectively. For these reasons, QCLs must be operated at cryogenic temperatures. Understanding of how the optical phonons scatter and decay into high thermal conductivity acoustic modes will be crucial for improving thermal abatement and in turn enabling the devices to be used on a wider range of applications where cryogenic temperatures are not

feasible.

Conversely, some applications require a reduction in the device thermal conductivity. Thermoelectric devices (TEDs) are designed to take advantage of the Seebeck effect to convert a temperature gradient into a usable voltage. With the global push for energy efficiency, thermoelectrics have become attractive for reclaiming waste heat in both industrial processes and consumer products. In the U.S., more than 50% of energy consumed to generate electricity in power plants is lost as waste heat while more than 30% waste heat is generated in automobiles[31]. Several industries are beginning to implement thermoelectrics as a way to recycle this waste heat. For example, the automotive industry employs TEDs on high temperature automobile components to reclaim waste heat and charge hybrid vehicles[32].

The major limitation of TEDs is the relatively low efficiency compared to the device cost. The figure of merit in thermoelectrics, a measure of device efficiency, is proportional to the electrical conductivity while inversely proportional to the thermal conductivity. The two main techniques for improving thermoelectric performance are to either develop a new material or alloy with high electron mobility and low thermal conductivity (such as SiGe alloys), or nanostructure a current material in a way that will reduce the thermal conductivity while minimally affecting the electrical conductivity (such as in a superlattice). Thus, advances in these systems will hinge on a detailed understanding of thermal transport both in the material as well as across interfaces.

1.3 Objectives

The overarching goal of this dissertation is to investigate and advance the understanding of the fundamental principles, which govern vibrational physics. There are two regimes in which vibrational transport studies can be categorized:

transport in materials and at interfaces between materials. To fully understand vibrational physics and in turn use these principles to predict thermal transport in complex devices, we must understand vibrational behavior in both of these regimes. The work performed over the course of this Ph.D. has touched on both regimes and can be divided into two thrusts.

The first thrust of studies completed during this Ph.D. focused on theoretical investigations of phonon transport across interfaces between dissimilar materials. Several studies were performed to study phonon scattering at interfaces while varying several properties, such as interface adhesion, interface impurities and material properties[33–37]. The results of these studies have led to significant advances in the understanding of phonon physics at interfaces and have prompted several questions about phonon physics in material layers providing motivations for the second thrust. The second thrust, which includes the topics covered in this dissertation, shifts to experimental work investigating phonon physics in nanostructured materials. The first study developed an experimental technique based on Raman spectroscopy for measuring temperature profiles of micro-electromechanical systems (MEMS)[38], while subsequent works have investigated thermal transport in two phase nano-structured carbon systems[39, 40].

The final work, covered by this dissertation, studies the effects of breaking translational symmetry on phonon behavior and nature. Of primary focus will be the less well understood transition regime between fully periodic and fully disordered/amorphous. Such knowledge will aid in advancing the understanding of phonon physics so that the next generation of models can be developed to predict thermal transport in non-periodic material systems. Work is also performed to address accurately measuring phonon properties using Raman spectroscopy in sub-micron thin films. These topics are divided in the following chapters:

- *Chapter 2 - Thermal Transport; from the Bulk Crystal to the Disordered Nano-structure*

This chapter aims to familiarize the reader with thermal transport in solid state systems. The discussion begins with the periodic crystalline system and then addresses complexities arising from imperfections in the crystal and disorder.

- *Chapter 3 - Raman Spectroscopy*

Raman spectroscopy will be the primary tool used to probe phonon physics in this work. This chapter will describe the fundamentals of Raman scattering and what physical insights can be extracted from the Raman spectrum.

- *Chapter 4 - Limits of Phonon Linewidth Measurements*

The spectra of SiGe thin films on Si substrates yield a spectrum with two partially overlapping peaks; one due to the alloy thin film and the other the substrate. This chapter addresses the complexities of separating the two spectra while retaining low uncertainties in the measured spectral parameters.

- *Chapter 5 - Laser Heating of SiGe Alloys*

The linewidth of the Raman spectrum can be influenced by the probing laser through optical heating. In nanoscaled Si, the incident laser power has led to changes in the shape of the Raman spectrum beyond the linewidth. This chapter attempts explain why these changes are observed in SiGe thin films through both experimental and computational methods.

- *Chapter 6 - Phonon Scattering and Localization in $Si_{(1-x)}Ge_x$ Thin Films*

Phonon behavior and nature is characterized in nanoscaled SiGe thin films using Raman spectroscopy. The germanium content, dislocation density and film thickness are systematically varied to gain insight into phonon physics in non-periodic systems. Techniques developed to minimize uncertainties in Chapter 4 are employed. Temperature dependent scattering rate measurements are fit to different scattering rate models to elucidate the effects of changing material parameters on phonon scattering.

- *Chapter 7 - Conclusions*

The scientific contributions and conclusions of this dissertation are summarized.

Chapter 2

Thermal Transport:

from the Bulk Crystal to the Disordered Nano-structure

This chapter describes the physical nature of thermal transport. The first section outlines the physics of thermal conductivity from first principles, including how phonons are considered and how they interact with their environment. I then present how imperfections to the periodic lattice are handled in the perturbation approximation. The current understanding of phonon physics in amorphous materials is then discussed. Finally, the transition regime between fully crystalline and fully disordered/amorphous is addressed.

2.1 Bulk Crystal

In bulk periodic non-metallic crystals, thermal transport is treated in an analogous manner as gas transport or diffusion, where the energy carrying particles are phonons instead of gas molecules. The model ubiquitously used to predict phonon thermal transport is the phonon gas model (PGM). The PGM has been successfully used to predict thermal transport in a wide variety of bulk crystalline materials. This section briefly outlines the background physics of the PGM including the definition of a phonon.

2.1.1 Phonons

Thermal transport in non-metallic condensed matter is driven by the transfer of vibrational energy through a material. In semi-infinite defect free crystals, this vibrational energy is transferred by what are called phonons[11, 41, 42]. Before detailed discussions of thermal transport can be had, an understanding of some basic principles of phonons must be developed. This section presents those principles in preparation for the following sections discussing phonon thermal transport and scattering.

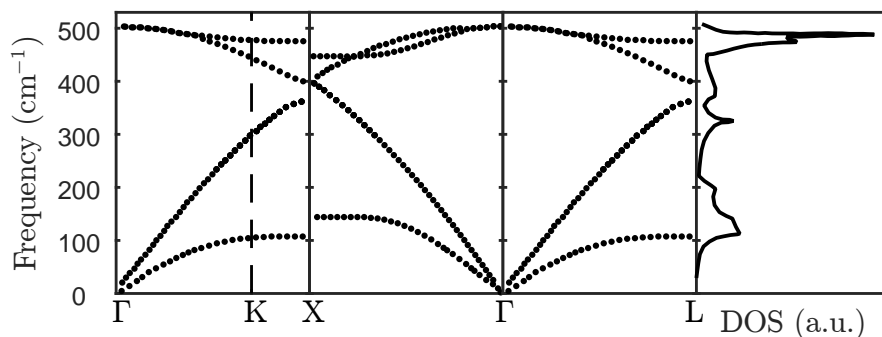


FIGURE 2.1: Silicon dispersion along several high symmetry direction in the Brillouin zone[1]. The density of vibrational states calculated from the dispersion is shown in the right most panel.

A crystal can be roughly modeled by treating atoms in the crystal as point masses and the interactions between the atoms as springs. In any system of springs and masses, a system of equations describing the forces on each atom can be written using classical Newtonian equations. The eigenvectors and eigenenergies of the system of equations can be solved for yielding the atomic displacements, u , and frequencies, ω , of each normal vibrational mode in the system. There are $3N$ normal modes in the system, where N is the number of atoms in the system. In a perfect semi-infinite crystal, these modes can be very accurately described by plane waves,

$$u(x, t) = \exp(i(qx - \omega t)) \quad (2.1)$$

which have a characteristic frequency (eigenenergy) and wavevector, $q = 2\pi/\lambda$,

where λ is the wavelength, x is spatial coordinate and t is time. The important consequence of the plane wave result is that all the modes are delocalized and propagating, meaning energy from a normal mode can be transmitted throughout the entire crystal. Additionally, a wavevector is only definable in a planewave. Not all combinations of wavevectors and frequencies are allowed, and the allowed frequency and wavevector combinations are described by the dispersion relation. Unlike photons, a phonon dispersion is not linear, in general, and is often very complex, as is the case for crystalline Si[43] shown in Fig. 2.1. Additionally, phonons have both a maximum wavevector and frequency (i.e., cutoff frequency) unlike photons. The maximum wavevector arises from the minimum phonon wavelength that is possible in a discrete medium and defines the Brillouin zone edge.

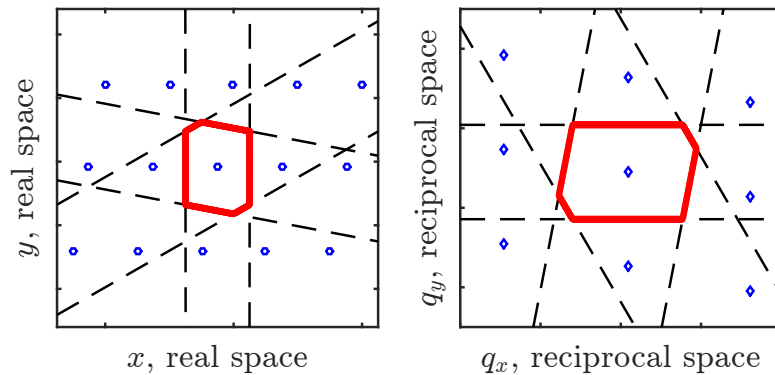


FIGURE 2.2: (a) (left) Hypothetical 2-dimensional crystal. Dashed lines represent bisections of lines between center atom and nearest neighbors. Red line outlines boundary of unit cell created by bisections. (b) (right) Corresponding lattice in reciprocal space and resulting Brillouin zone in red.

In a perfect crystal, a unit cell can be defined which is the smallest unit of the crystal that can be repeated an infinite number of times to reproduce the infinite crystal, as shown in 2-dimensions in Fig. 2.2(a). The Brillouin zone is the unit cell in reciprocal space and defines the maximum wavevector in each crystallographic direction, as shown for 2-dimensions in Fig. 2.2(b). This maximum wavevector in each direction is inversely proportional to the width of the unit cell in that direction, l_u , i.e., $q \propto 1/l_u$. For a crystal where the unit cell is made up of one atom, i.e., basis

$= 1$, then the unit cell width is just equal to the interatomic spacing, a . However, in the case of a unit cell that contains more than one atom, i.e., basis > 1 , the unit cell width is larger and thus the Brillouin zone is smaller than the basis $= 1$ case.

The Brillouin zone and dispersion describe the normal modes of the system, however, these normal modes are not phonons. A phonon is a quanta of energy that exists within a normal mode. The normal modes can be thought of as harmonic oscillators with mass equal to the reduced mass of the unit cell, m_{red} , and effective spring constant, k_{eff} , with characteristic frequency $\omega_n = \sqrt{k_{eff}/m_{red}}$. The energy levels, defining the amplitude of oscillation, of a quantum harmonic oscillator are discretized so that each energy level is separated by $\hbar\omega_n$, where \hbar is Planck's constant divided by 2π . A phonon is a quantum particle of energy equal to $\hbar\omega_n$ within a normal mode. Therefore, when energy is transferred between normal modes it must happen in discrete quanta, resulting in phonons having both particle and wave characteristics.

2.1.2 Phonon Gas Model

Due to the particle-like behavior of phonon interactions, phonon thermal transport is most often modeled using a physical description analogous to that used in gas transport[9, 11, 41, 42]. Following simple kinetic theory arguments, the phonon gas model for predicting frequency dependent phonon thermal conductivity, $\kappa(\omega)$, can be written as,

$$\kappa(\omega) = \frac{1}{3}C_v(\omega)v^2(\omega)\tau(\omega), \quad (2.2)$$

where $C_v(\omega)$ is the specific heat, $v(\omega)$ is the phonon group velocity and $1/\tau(\omega)$ is the phonon scattering rate which is related to the mean free path, $l = v\tau$. The PGM assumes that the dispersion is well defined and that it remains roughly unchanged with the introduction of imperfections to the lattice. It also assumes that the imperfections do not change the planewave nature of the normal modes and only affect the scattering

behavior of the modes. For crystalline systems, the dispersion is relatively easy to calculate using lattice dynamics, which in turn can be used to calculate the phonon group velocity and specific heat. However, understanding of scattering rates is in its infancy making scattering rate calculations much more complicated.

Phonon scattering rates can be determined from first principles calculations such as density functional theory (DFT)[44, 45], from molecular dynamic (MD) simulations[46] or empirically from fits to experimental data[47, 48]. Both MD and DFT are computationally expensive methods, which are not necessarily accessible to the experimentalist. Additionally, DFT calculations are of a super cell with a size limited by computational resources, which results in discretized phonon modes and suppressed long wavelength modes. MD simulations, suffer from the same problems as DFT calculations, and are based on classical forces rather than the quantum mechanical principles that govern phonon physics. The most computationally simple method to determine τ is to fit Eq. 2.2 to a set of temperature dependent thermal conductivity data. However, this requires an assumption of the form of the model. Since the group velocity and specific heat can be calculated directly from the phonon dispersion, a form of the scattering rates must assumed.

2.1.3 Phonon Scattering

Three types of scattering events are most commonly considered when employing the PGM: boundary, phonon-phonon and impurity scattering[9, 11, 41, 42], depicted in Fig. 2.3. Boundary scattering is an elastic process, which is a result of phonons impinging on the physical boundaries of the finitely sized crystal[49]. This can be at grain boundaries or at interfaces between different materials. Impurity scattering results from scattering of phonons with perturbations of the periodic lattice, such as with mass impurities or bonding perturbations[50]. In real crystals, examples of such impurities could be dopants, isotopes, dislocations or disordered regions. For each of these scattering types, simple models have been derived to describe the frequency

and temperature dependence.

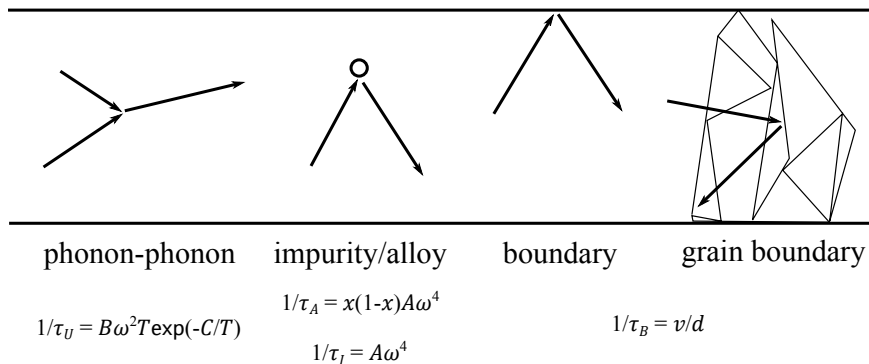


FIGURE 2.3: Diagram of various phonon scattering types with corresponding model equations used in the phonon gas model.

In a perfectly periodic bulk non-metallic crystal, the only scattering events possible are between phonons[42]. Phonon-phonon scattering is an inelastic process caused by anharmonic interactions by which a phonon may decay into multiple lower energy phonons or multiple phonons may combine to create a phonon of higher frequency[51, 52]. Phonon-phonon scattering can be divided into two categories: normal scattering, which conserves crystal momentum (wavevector) and energy and Umklapp scattering which does not conserve momentum. Since Umklapp scattering does not conserve momentum, it is a major contributor to thermal resistance in pure or nearly pure crystals, and is the reason for the decrease in thermal conductivity in highly crystalline materials above ~ 10 K. Umklapp scattering occurs when two or more phonons combine resulting in a phonon with a wavevector that falls outside of the Brillouin zone which flips the sign of the resulting momentum vector. Both types of phonon-phonon scattering events are driven by anharmonicity in the potential energy between atoms. As temperatures increase and modes become more populated, the oscillatory amplitude of the modes increase leading to an increased expression of anharmonic behavior. Therefore, phonon-phonon scattering in a crystal is temperature dependent, and has been

functionally modeled as,

$$\frac{1}{\tau_U} = B\omega^2 T \exp(-C/T), \quad (2.3)$$

where B and C are both parameters extracted from fits of the PGM to temperature dependent thermal conductivity data¹.

Boundary scattering only depends on the frequency at which a phonon encounters a boundary. Therefore, the boundary scattering rate is directly proportional to the ratio of the phonon velocity and the limiting dimension of the crystal in which the phonon exists[48, 55],

$$\frac{1}{\tau_B} = \frac{v(\omega)}{d}. \quad (2.4)$$

So, as the limiting dimension of a material decreases, phonons are scattered more often leading to a reduction in thermal conductivity.

In 1955, assuming low temperature, i.e., a harmonic system and a Debye dispersion, Klemens[50] used perturbation theory to derive a temperature independent equation for the scattering of impurities with a 4th order frequency dependence. This has remained the assumed dependence for scattering with impurities and in alloys, and typically the formula,

$$\frac{1}{\tau_I} = A\omega^4 \quad (2.5)$$

is used as the impurity scattering rate, where A is a fitting parameter gleaned from fits to temperature dependent thermal conductivity data. This scattering rate is extended to the case of alloys by multiplying by the fractional compositions of the alloy components[56]. In the case of a two element alloy, e.g. $\text{Si}_{(1-x)}\text{Ge}_x$,

$$\frac{1}{\tau_A} = x(1-x)A\omega^4 \quad (2.6)$$

¹The forms of the scattering rate equations presented in this section have been derived through a variety of methods and have several forms[53–55]. For simplicity, only one form for each is presented.

where x is the molar composition of the element B and $1 - x$ is the composition of element A.

While the simplicity of these scattering rate equations makes them wieldy, this simplicity comes from derivations under very specific and special cases making their application limited. Boundary scattering was derived using kinetic theory which treats each phonon as a hard sphere thus forcing elastic scattering and in turn temperature independent trends. Alloy and impurity scattering rates were derived under harmonic conditions with an assumed Debye dispersion. The harmonic condition forced the scattering to be elastic and temperature independent while the Debye dispersion is responsible for the ω^4 frequency dependence. Furthermore, the Klemens impurity scattering rate equation was derived using perturbation theory which is only applicable to very small perturbations of the system. Only the Umklapp scattering rate was derived assuming anharmonic potentials, leading to the temperature dependence.

The importance of dispersion considerations is illustrated in the derivation of impurity/alloy scattering of optical phonons. The frequency dependence of Eq. 2.6 suggests that optical phonon scattering is dominated by alloy type scattering in SiGe alloys[48]. However, the Debye dispersion used during this derivation does not describe the optical phonon dispersion well. If the Debye dispersion in the Klemens derivation is replaced with a linear dispersion ($\omega = -v_p q + \omega(0)$) to approximate the optical phonon dispersion, the impurity scattering rate becomes,

$$\frac{1}{\tau} = \frac{a^3}{4\pi G} \left(\frac{\Delta m}{m} \right)^2 \frac{\omega^2(\omega - \omega(0))^2}{v_p^3}, \quad (2.7)$$

where a is the interatomic spacing, G is the number of atoms in the semi-infinite crystal, m is the mass, Δm is the mass difference between the impurity mass and normal mass, $\omega(0)$ is the optical phonon frequency at the Γ -point and v_p is the phase velocity. Note that this equation is identical to the mass impurity scattering rate

derived by Klemens, if we set $\omega(0) = 0$ since we have recovered the Debye dispersion. Equation 2.7 no longer has an ω^4 dependence and instead is dependent on both the frequency and the difference between the frequency and the Γ -point frequency. The dependence can be rewritten as ω^2/λ^2 using the linear dispersion relationship and $q = 2\pi/\lambda$ where λ is the phonon wavelength, which shows that the scattering rate is equally dependent on both frequency and wavelength. Additionally, several other works have highlighted the importance of correctly describing the dispersion in phonon transport[57–59].

In a recent unpublished study², my co-authors and I investigated the impact of anharmonicity on phonon scattering across a boundary using wave packet simulations. In our case, we simulated the scattering of a single phonon at the interface between two different harmonic materials with either a harmonic or anharmonic interface. Figure 2.4 plots the Fourier transform of the atomic displacements in the test cell before interface scattering and after with harmonic and anharmonic interface potentials. In the harmonic case, we see that the single phonon splits into two phonons, one transmitted and one reflected, with equal frequency but different wavevector indicating elastic scattering. In the anharmonic case, the phonon scatters into the same two wavevectors as the harmonic case, but a third phonon also results indicating inelastic scattering. A similar result was observed for scattering with an impurity mass. The degree of this inelastic scattering is dependent on both the magnitude of the anharmonic potential term and the amplitude of the atomic oscillation. Since the amplitude of oscillation depends on the phonon population, which is temperature dependent, impurity and boundary scattering should exhibit a temperature dependence in contrast to the predictions of Eqs. 2.4 and 2.5.

With the limited ability of Eqs. 2.3-2.6 to describe temperature and frequency trends of phonon scattering, there is a need for a direct probe of phonon scattering.

²Presented at Spring MRS 2013, N. Le, C. Saltonstall, P. Norris, abstract: V7.22

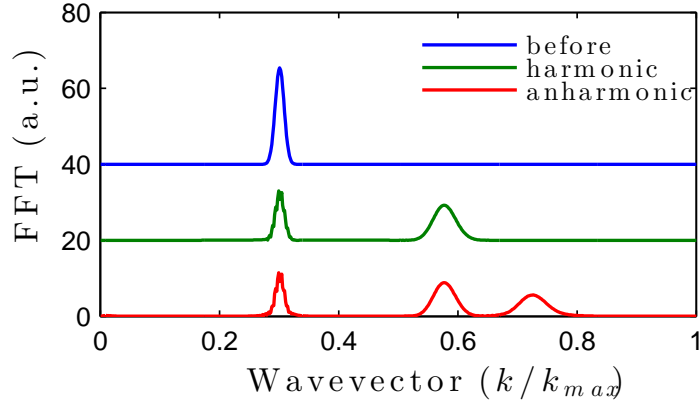


FIGURE 2.4: Fourier transform of atomic displacements in wavepacket simulation before scattering at interface and after with harmonic or anharmonic potentials at the interface. Anharmonicity causes the incident phonon to split into two phonons after reflecting at the interface indicating inelastic scattering processes, which in turn implies a temperature dependent scattering event.

In response, this study experimentally investigates the temperature and frequency trends of impurity, alloy and boundary scattering of optical phonons in SiGe alloys using Raman spectroscopy. The results will be used to help elucidate phonon behavior in a variety of environments in an effort to improve our ability to predict and tune thermal transport.

2.2 Breaking Periodicity

In real applications, materials rarely have properties consistent with the theoretical conditions described above. Especially, with the current miniaturization trend of electronics, materials are often applied in nanoscale forms. Additionally, many materials do not fall into the category of crystalline and so their normal modes cannot be described by plane waves making the application of the PGM questionable[15, 16, 60].

2.2.1 Nanoscaling

At the nanoscale, the physics that governs bulk thermal transport breaks down. Fourier’s law for heat conduction no longer holds because material length scales reach mean free path lengths of the primary energy carriers. When this happens, the phonon gradient can no longer be well defined, similar to the problem of rarefied gas flow. Under these conditions, thermal transport deviates significantly from the Fourier Law and the thermal conductivity is no longer an intrinsic property of the material but depends on the material size[48].

There are several regimes where nanoscaling influences thermal transport, each of which affects transport through a different mechanism as outlined in Table 2.1[55]. These regimes can be bounded by the average thermal phonon mean free path, l , and the average thermal phonon wavelength, λ_0 . The average mean free path in Si at room temperature has been calculated using several methods to yield values from 41 to 300 nm. The thermal phonon wavelength (1.4 nm in Si at room temperature) can be roughly calculated using $\lambda_0 = hv_s/k_B T$, where h is Plank’s constant, k_B is the Boltzmann constant and v_s is the sound speed.

When the limiting dimension of the crystal is much larger than the mean free path of the thermal phonons, the bulk condition is met and the PGM and Fourier’s law accurately describe phonon transport. As the material scale is reduced below the mean free path but much greater than the thermal wavelength, boundary scattering begins to play a significant role in the overall scattering rate. Further reduction in the material size to near the phonon wavelength begins to modify the dispersion through quantum confinement, by reducing the size of the Brillouin zone and flattening the dispersion branches. This strongly reduces thermal conductivity by increasing boundary and Umklapp scattering while also reducing the phonon group velocities[55, 61–65]. This reduction in acoustic phonon thermal conductivity also results in optical phonons contributing to a higher fraction of the total thermal conductivity[66]. The transition between bulk and modified dispersion (regime 2 to

TABLE 2.1: Four regimes of phonon transport at various scales. As material scales, d , decrease, boundary scattering and dispersion modifications influence thermal transport.

Regime	Scale	Phonon Dispersion	Scattering Processes
1.	$d \gg l$	bulk	τ_U, τ_I
2.	$\lambda_0 \ll d \leq l$	bulk	τ_U, τ_I, τ_B
3.	$\lambda_0 \leq d \ll l$	modified	τ_U, τ_I, τ_B
4.	$d < \lambda_0$	modified	ballistic transport

3) does not occur sharply and is not well understood. So, the effect of dispersion modification will likely be observed over a wide range of material scales at various strengths in addition to boundary scattering. At the smallest scales, where the material sizes are below the phonon wavelength, thermal conductivity becomes quantized[67].

Several studies have also shown that localized vibrational modes are formed at surfaces and interfaces which can trap vibrational energy[27, 68–71]. Additionally, these localized modes reduce the plane wave like nature of thermal transport in nanoscaled material leading to a reduction in the overall thermal conductivity. As the size of a material is reduced, these localized modes contribute to a larger fraction of the vibrational spectrum leading to significantly reduced thermal conductivity.

Current transistor technology employs materials with dimensions in the tens of nanometers[72], which is well in to regime 2 where boundary scattering is important and approaches regime 3 where the dispersion begins to be modified. These modifications significantly alter phonon transport making it difficult to design and model devices from a thermal perspective. As was previously mentioned, thermal issues are currently hindering the advance of many electronic devices, therefore, it is imperative for the design of nanoscaled devices that we have a detailed understanding of how nanoscaling influences both the scattering and dispersion on phonons.

2.2.2 Disorder

In addition to nanoscaling, the periodic structure of a material can be broken through the introduction of disorder either through compositional disorder caused by impurities or alloying, or spatial disorder as in amorphous materials. In any case, the influence of the disorder causes a reduction in thermal conductivity when compared to the periodic case, which can also lead to a change in temperature trends[73–75]. Moreover, the changes in thermal conductivity temperature trends depend on the type of disorder. Several models have been developed to describe thermal transport in each of the mentioned disorder types[15, 16, 44, 71, 75–78]. The main theories are that disorder influences the mean free path (scattering rate) of phonons[75–77] or that it modifies the phonon structure itself[15, 16, 71, 78]. However, the exact mechanism for changes in thermal conductivity is still controversial and the transition from one disorder type to another is not well understood.

Structurally, disorder can be classified as either compositional disorder or spatial disorder. Spatial disorder is defined as disorder where the periodicity of the lattice is destroyed, Fig 2.5 b). This may be at levels from disperse dislocations to nanograined structures to completely amorphous materials. Compositional disorder results when the periodic lattice of the crystal remains intact, while the arrangement of atomic species on that lattice is disordered, Fig 2.5 c). Examples are crystalline alloys such as SiGe or impurity disorder where very small fractions of impurities replace atoms in a crystal such as in KBr-KCN or in substitutionally doped semiconductors. Note that alloys can also be ordered, so that they have periodic arrangement of atoms in both space and composition[79, 80], Fig. 2.5 d). Additionally, this order can vary continuously and is quantified by an order parameter. Both of these disorder types result in changes to thermal conductivity temperature trends, but in very different ways.

There are three thermal conductivity temperature trends that result from the introduction of disorder: impurity, alloy and glassy types, shown in Fig. 2.6. In a

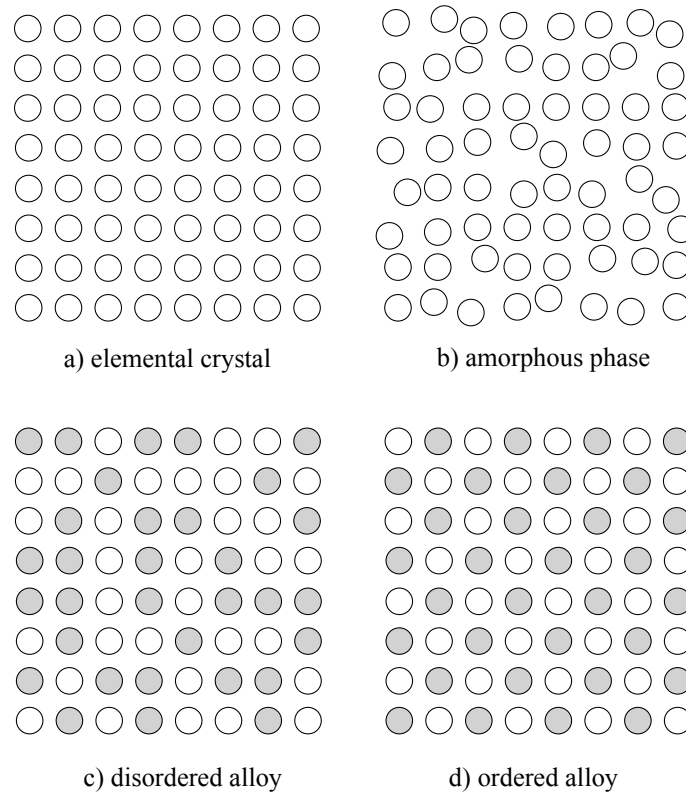


FIGURE 2.5: Diagram of different material phases illustrating spatial and compositional order and disorder.

crystalline material, the thermal conductivity increases at low temperature due to an increase in specific heat and around 10 K, the temperature trend begins to decrease as a consequence of Umklapp scattering. Impurity trends occur when a periodic crystal contains small levels of imperfections due to dislocations or impurity masses. Impurity disorder results in a reduction of thermal conductivity (usually less than a factor of 10) over all temperatures but does not change the overall temperature trend. Impurity disorder is well handled by the PGM through a temperature independent impurity scattering rate term, Eq. 2.5, and no perturbation to the specific heat or group velocities[77]. Alloy trends occur when significant levels of impurity atoms are introduced to a system so that the new system must be considered a new material. These changes are adequately handled using the PGM and Vegard's law for the dispersion of the two materials along with

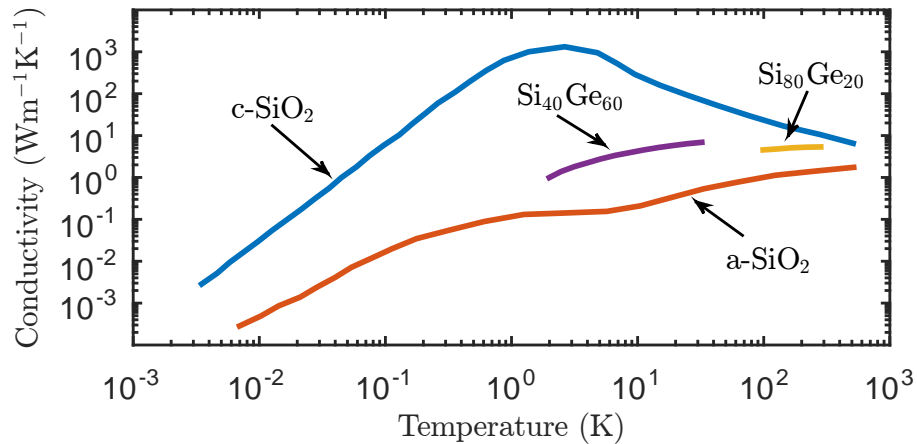


FIGURE 2.6: Thermal conductivity of crystalline and amorphous silicon dioxide and compositionally disordered SiGe alloys[2–4]. Amorphous SiO_2 shows monotonic glass-like thermal conductivity trends, while the crystalline phase shows typical arching crystalline temperature trends. The SiGe alloys illustrate the flattening effect of alloying.

an alloy scattering rate term, Eq.2.6[48, 81]. Alloy disorder results in a large (greater than a factor of 10) reduction in thermal conductivity and flattens the temperature trend due to the temperature independence of alloy scattering. The final case of glassy materials occurs when either the system is spatially disordered (amorphous) or when a material is alloyed in very specific ways[82]. This case is not well handled by the PGM because the vibrational modes cannot be well described by planewaves, so that the dispersion, group velocity and wavevectors are ambiguous[12].

In glassy materials, the thermal conductivity departs wildly in both trend and magnitude from crystalline counterparts. Eucken first observed in 1911 that thermal conductivity for glassy materials was orders of magnitude lower than the crystalline phase and that it increased monotonically with temperature with a plateau around 10 K as opposed to the arching trend in the crystalline phase[83]. Additionally, all glasses have nearly the same thermal conductivity regardless of chemical composition. Kittel presented the first explanation for the glassy conductivity behavior, by showing that the phonon mean free path is dominated by the spacing of geometric disorder and so

is nearly constant in any type of amorphous material[73]. This idea was extended by Slack, who also assumed that the mean free path must be constant, but that it could be no less than one phonon wavelength or the vibrational mode was not defined in the crystal[84]. Using this assumption along with the PGM, he derived an equation for the thermal conductivity of glassy materials. Following arguments from Einstein's description of thermal conductivity of solids[85], Cahill, Watson and Pohl (CWP) argued that the actual minimum mean free path of a phonon is one half the wavelength resulting in the ubiquitously cited minimum thermal conductivity model[75, 82]. The interpretation of the CWP model is that the phonons approach a limit where they can be thought of as localized weakly coupled harmonic oscillators, where the energy diffuses through the material by transferring energy between adjacent oscillators. The main problem with the CWP model is that it does not describe the thermal conductivity of the plateau region around 10 K and below.

The thermal conductivity of glasses was simultaneously being studied using an alternate view point; spatial disorder destroys the planewave nature of phonons. In 1949, Kittel proposed the idea that the normal modes diverge from planewave nature as disorder is introduced into a sample[73]. In 1971, Zeller and Pohl, discovered a contribution to the low temperature specific heat of glassy materials not observed in crystalline phases[86]. They attributed this anomalous low temperature specific heat to low frequency localized modes caused by disorder in the amorphous phase. A year later, Anderson *et al.* proposed the idea of tunneling states where atoms in the amorphous phase can sit at more than one local minimum in the crystal potential leading to vibrational modes caused by the atoms tunneling from one local minimum to another[87]. A similar result was found in KBr alloyed with KCN[88]. The CN^- ions replace Br^- in the alloy, and since CN^- can be oriented in several directions at the Br^- site with equal energy, a "librational" mode, similar to the tunneling modes described by Anderson *et al.*, is formed resulting in a glass like thermal conductivity.

In 1999, Allen *et al.* combined the idea of localized modes with the phonon

diffusion idea of Slack and CWP. They redefined phonons in amorphous materials as vibrons, which do not necessarily have a planewave structure[12]. They then defined three regimes of vibrons which have distinctly different nature and behavior: propagons, diffusons and locons[12, 13, 89, 90]. Propagons were defined as low frequency modes with planewave like nature, i.e. non-localized and propagating. Diffusons were defined as mid-frequency partially localized modes that propagate through the system, i.e. diffusing vibrations. Locons were defined as high frequency localized, non-propagating modes. Using these definitions, locons were ignored for thermal transport since they could not move through the material. However, the propagons and diffusons were treated as two different but parallel conduction channels. Propagons dominate thermal transport at low temperature below 10 K and around 10 K diffusons begin to significantly contribute to thermal transport. The transition between the two leads to the observed plateau in glassy thermal conductivity near 10 K. This idea is in agreement with the CWP thermal diffusion concept and explains the disagreement at very low temperatures.

Recently, the notion of non-planewave modes influencing thermal transport in disordered and nanostructured systems has gained traction in systems other than glassy or amorphous materials. Estreicher has shown that localized surface modes in nanowires trap phonon energy[71]. At the same time, they showed that imperfections/defects in a crystal do not scatter phonons like hard sphere elastic scattering[78]. Instead, defects create spatially localized modes (SLM) around the defects which trap thermal energy and reduce thermal conductivity. A similar result was found by Yamamoto and Watanabe using non-equilibrium Green's function methods (NEGF)[91]. This new concept of thermal transport, has made it difficult to justify the use of the PGM for non-periodic systems. With that in mind, Lv and Henry have very recently bypassed the PGM entirely and employed Green-Kubo methods to calculate thermal conductivity of crystalline and amorphous materials to study in effects of localizing modes[15, 16].

With the new understanding of how changes in the periodicity of a material introduce spatially localized modes rather than simple scattering sites, it is important to understand how scattering rates and localized modes evolve with changing material properties, e.g., impurities and size. This information will be useful for understanding how the localized and bulk-like modes interact so that more accurate models can be developed to predict thermal transport in complex systems.

In response, this study uses Raman spectroscopy to probe both the scattering rate and the localization of optical phonons in SiGe alloy thin films with varying compositions, thicknesses and dislocations with the aim of understanding how each property influences both the nature and behavior of thermal vibrations. The following chapter introduces Raman spectroscopy and how it can be used to probe a variety of material properties and extract information about phonon physics.

Chapter 3

Raman Spectroscopy

The primary tool used in the studies presented here is Raman spectroscopy. Raman spectroscopy is a laser based, non-invasive, non-contact technique used to probe the population of Raman active phonons in a material. The measured population results in characteristic line shapes of the Raman peaks, which can be used to extract certain properties of the material, such as stress, temperature, and phonon scattering rates[92]. This chapter outlines the Raman process and how a Raman spectrum can be used to extract physical properties of a material.

3.1 Raman Scattering

The Raman technique uses a narrow wavelength laser source focused on the sample as the probe[93]. When light impinges on the surface of a Raman active material a photon may be absorbed by an electron in the material exciting it out of its ground state. If the energy of the photon happens to closely match the energy of an allowed electronic transition, then the electron will be excited into a higher energy quantum state and the result will be a special case of Raman spectroscopy called resonant Raman, which will be discussed later. In spontaneous Raman spectroscopy, the incident photon energy does not match the energy of an electronic

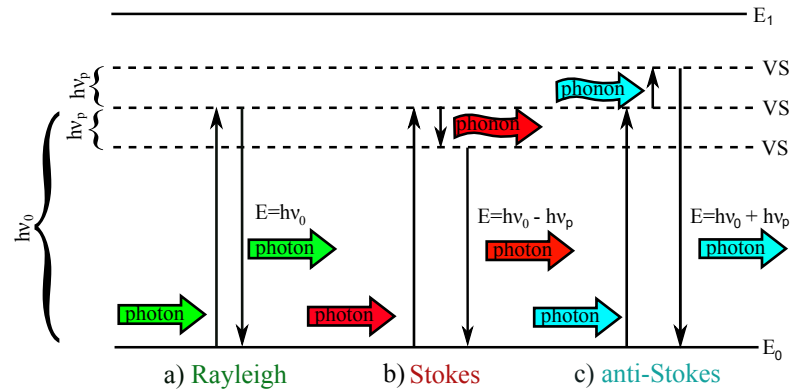


FIGURE 3.1: Energy of an electron during the three spontaneous Raman processes. a) Rayleigh scattering involves the absorption of a photon by an electron to a virtual state (VS), then the spontaneous decay back to ground state yielding an elastically scattered photon. Stokes (b) and anti-Stokes (c) processes involve inelastic scattering of the electron with the vibrational system yielding an energy shifted photon.

transition and the electron will be excited into what is termed a virtual state[93, 94]. A virtual state is disallowed by quantum mechanical postulates, but can be momentarily populated by the perturbation of the system from an outside force, e.g. a laser. The most probable outcome of this excited state is that the electron decays back down to its original ground state emitting a photon of the same energy as the laser in a random direction, Fig. 3.1(a). This process is termed Rayleigh scattering and dominates the light scattered from the material surface. Alternatively, the excited electron may interact with the vibrational system of material causing it to gain or lose energy. When that energy shifted electron decays back down to its ground state the photon emitted will be shifted by the energy transferred to or from the vibrational system. Raman light that has lost energy is termed Stokes shifted, Fig. 3.1(b), and light that has gained energy is termed anti-Stokes, Fig. 3.1(c). This vibrationally shifted light can then be collected, separated into each wavelength by a spectrometer and measured by a detector. The resulting spectrum will have the Stokes and anti-Stokes peaks shifted symmetrically on either side of the Rayleigh line, as is shown for the simple case of silicon in Fig. 3.2(a).

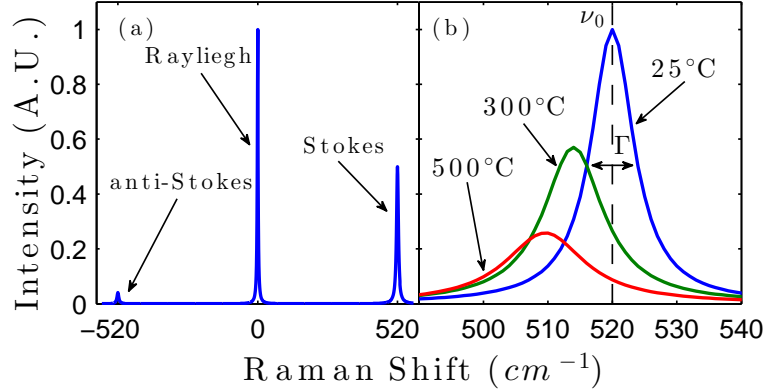


FIGURE 3.2: (a) Typical Raman spectra of silicon showing both the Stokes and anti-Stokes peaks (not to scale). (b) Temperature dependence of the Stokes peak of silicon. As temperature increases the peak intensity, I_0 , and peak position, ν_0 , decrease while the line width (FWHM), Γ increases.

Not all vibrational modes are Raman active and only modes that satisfy both conservation and selection rules¹ can be probed using Raman spectroscopy[93, 95, 96]. There are two conservation rules that must be obeyed in the Raman scattering process: momentum and energy conservation. When a vibration scatters with an electron and some of the electron energy is transferred to the vibrational system, the transferred momentum must be conserved along with the energy. At the quantum level, the momentum, p , is defined by the wavevector of the quantum particle, $p = \hbar q$ [97]. As discussed in Section 2.1, a phonon wavevector ranges from 0 to π/a , and is inversely proportional to the wavelength. The unit cell length of most materials is on the order of 4-5 Å while the wavelength of visible Raman light is on the order of 5000 Å. The wavevector of the incoming laser light is therefore much smaller than the maximum phonon wavevector. So, in order to satisfy the conservation of momentum condition, Raman spectroscopy can only probe vibrations with very small wavevectors, i.e. zone center, Γ -point modes[96]. For simple systems like Si, there are only two triply degenerate modes at the Γ -point, three for the acoustic modes and three for the optical modes, see Fig. 2.1[43]. Since acoustic modes have nearly zero energy close to the zone center, electron-phonon scattering of acoustic modes will not

¹Polarization can also impact scattering[93], but this is outside the scope of this work.

result in an observable Raman shift of the incident light. On the other hand, optical modes have a non-zero frequency at the Γ -point and so are able to shift the energy of the incident light sufficiently far to be observed as a second peak in the spectrum. For these reasons, only the zone center, optical modes are observed in spontaneous Raman scattering of periodic structures².

Even if conservation of momentum and energy rules are satisfied, a mode is only visible in the Raman spectrum if it also obeys symmetry selection rules. In infrared absorption spectroscopy, light is directly absorbed by the vibrations through a coupling to the dipole moment of the material. Therefore, only vibrations that change the dipole moment of the crystal are IR-active[95]. The Raman process on the other hand involves the scattering and energy shift of light through a coupling with the polarizability. Therefore, only vibrations that have a symmetry which induce a change in the polarizability are Raman active[93–95]. In centrosymmetric materials, IR-active modes are those that have an asymmetric motion, while Raman-active modes are those that have a symmetric motion. The details of how to determine which modes obey symmetry selection rules is outside the scope of this work, but in periodic crystals and in molecules with point group geometries, activities can be determined using group theory[95, 96].

3.1.1 Disorder and Nanoscaling

The previous discussion describes the selection rules for individual molecules or crystals with a high degree of translational symmetry. However, when the translational symmetry of the crystal is reduced through introduction of disorder or by nanoscaling the material, selection rules change, allowing modes not observed in the Raman spectrum of the periodic structure to be present[98, 99]. The exact mechanism for this is controversial[99], but results from changes in the symmetry of

²This is only true for first order Raman scattering, which is the focus of the work presented in this dissertation.

vibrations which allows for a change in the polarizability during the vibration of the mode. Therefore, modes that were not originally Raman active in the periodic system will be observed in the Raman spectrum of the non-periodic system.

In nanoscaled systems, the conventional theory is that nanoscaling confines modes resulting in a relaxation of selection rules so that modes away from the zone center can be probed[100–102]. Richter first proposed that modes away from the zone center contributed to the Raman spectrum of nanoscaled systems with a decaying magnitude as the distance from the zone center increased[100]. The distance in q -space that can be probed, Δq , is related to the geometry of the nanoscaled system and magnitude of the limiting dimension, d . For simplicity, and somewhat arbitrarily, he chose a Gaussian function as the q -space weighting function, resulting in $\Delta q = A/d$, where Δq is the Gaussian width and A is a proportionality constant that varies based on geometric arguments. The result of probing modes away from the zone center is an asymmetry of the Raman peaks due to the slope of the dispersion curves. This asymmetry is often used as a metric of phonon confinement and to quantify the size of nano-structures[103–111].

When investigating the evolution of the Raman spectra in disordered carbon, Ferrari and Robertson considered the nano-crystalline phase an intermediate between the fully crystalline and fully disordered phase[98]. As carbon transitions from graphite to amorphous carbon, the Raman spectrum evolves from a single narrow peak to multiple peaks and eventually to a spectrum that is very similar to the vibrational density of states. A similar result is found for nano-crystalline[103, 112, 113] and amorphous tetrahedral semiconductors[114]. Since the nanocrystalline phase is on the amorphization trajectory, they attributed the changes in the Raman spectrum from graphite to amorphous carbon as being due to a similar confinement induced breakdown of selection rules as for the nanoscaled case addressed by Richter[100]. This implies that amorphization–spatial disordering–localizes vibrational modes to small domains in disordered materials.

With the theory that changes in the graphite spectrum are due to confinement of modes, they used changes in the relative peak intensities of graphite peak, G-peak, and one of the disorder induced peaks, D-peak, to quantify crystallite size in nanocrystalline graphite.

Following similar arguments used by Richter, and Ferrari and Robertson, several groups used the asymmetry observed in Raman spectra of spatially ordered, compositionally disordered alloys as a measurement of effective crystallite size or phonon correlation length, L_a [115, 116]. At the same time, other studies challenged these conclusions and asserted that modes were not localized due to alloying since the periodic lattice remained intact[117–119]. Instead, it was concluded that the asymmetry is a result of a distribution of frequencies being observed in the Raman spectrum due to the distribution of bonding environments in the disordered alloy[117]. Since then, several studies have shown that alloying localizes Raman active vibrations, thus reducing the correlation length, lending support to the prior conclusion that asymmetry in the Raman spectra of alloys is related to the phonon correlation length[120–122].

In nanoscaled or nanocrystalline materials, the phonon correlation length is well defined and represents the crystal or grain size. However, in alloys or disordered materials, the phonon correlation length is more ambiguous. In ion irradiated samples the phonon correlation length is considered the distance between disordered regions[123, 124]. And the distance between disordered regions defines the special extent of the mode[100]. In dilute alloys or doped materials, this concept is tenable. However, in highly alloyed materials, the spacing between impurities becomes smaller than the wavelength of the mode. At this level, the distance between the disorder sites and phonon correlation length are not equal. Instead, the phonon correlation length describes the phonon spatial extent, which could be larger than the spacing of the alloying species.

3.1.2 Resonant Raman

In addition to nanoscaling and disorder, the selection rules of Raman scattering can be affected by the Raman probing wavelength. As briefly discussed in Section 3.1, resonant Raman scattering occurs when the incident photon energy is close to the energy of an electronic transition[93–95]. In this case, a ground state electron is excited into an allowed energy state. When an electron is excited, it changes the bonding structure of the molecule or crystal. Any vibrational mode whose eigenvector contains motion along the perturbed bond, will have an enhanced interaction with the excited electron. If those modes are Raman active, then the signal of those modes will be augmented and in some cases, modes that are not normally Raman active will be observed in the Raman spectrum.

The radial breathing modes (RBM) in carbon nanotubes (CNTs) are examples of modes that are often probed using resonant Raman techniques[125–127]. Depending on the probing wavelength used, the number of RBM peaks observed and their frequencies change. This is due to different electron transitions being excited, which leads to an enhancement of different RBMs. Therefore, a variety of modes that are not Raman active can be probed by changing the wavelength of the incident light. A similar effect is seen in Si[128] and SiGe alloys[5], except the enhancement is most pronounced in modes that are already Raman active. Therefore, the Raman cross section, or scattering efficiency, can be varied by changing the wavelength of the probing light source.

Picco[5, 129] recently measured the Raman cross section of SiGe alloys as a function of composition and wavelength, Fig. 3.3. He showed that as the germanium content increased, the peak resonance shifted to lower energy wavelengths. He attributed this shift to a change in the direct electron band gap with composition. Therefore, as the band gap reduces, lower energy light can excite an electron from the valence band to the conduction band leading to resonant Raman scattering. In Chapter 4, different wavelengths will be used to collect Raman spectra and

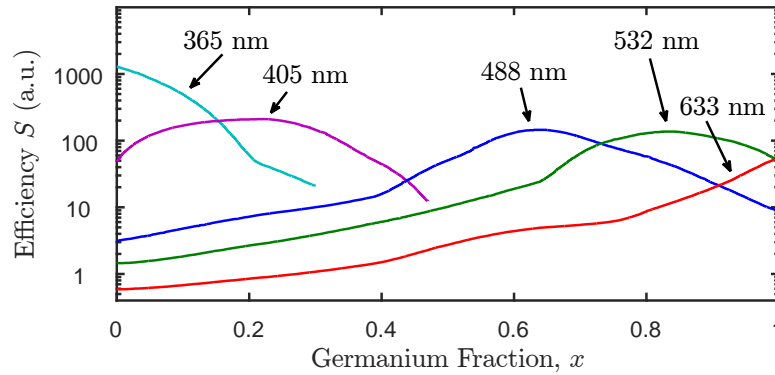


FIGURE 3.3: Raman scattering efficiency versus Ge fraction and wavelength[5]. As the Ge fraction increases, the peak efficiency shifts towards longer wavelengths indicating a narrower band gap.

knowledge of resonant Raman spectroscopy will be important for interpreting some of the results.

3.2 Material Characterization

Practically, each peak in a collected Raman spectrum can be described by the peak position, ω_0 , linewidth, Γ , peak intensity, I_0 , and in some cases, asymmetry by fitting to a representative function, such as a Lorentzian or Voigt, Fig. 3.2(b). Each one of these parameters is sensitive to a different physical property or to a set of material properties, such as temperature, composition, strain, disorder and sample size. Through proper calibration and fitting the Raman spectrum can be used to quantify these properties. This section discusses the background physics for why each peak parameter is sensitive to a particular property and how to use the Raman spectrum to probe the property of interest.

3.2.1 Peak Position

The peak positions in the Raman spectrum is a function of sample temperature[92, 130]. As temperature increases, the amplitude of oscillation of the atoms increases.

In a harmonic system, no change in the Raman spectrum would be observed since frequency does not change with amplitude of oscillation. However, as the amplitude of oscillation increases in an anharmonic system, the curvature of the potential changes, leading to a change in the frequency of the vibrations as shown in Figs. 3.2(b) and 3.4. Simultaneously, the average atomic position changes leading to thermal expansion and a further shift in vibrational frequency.

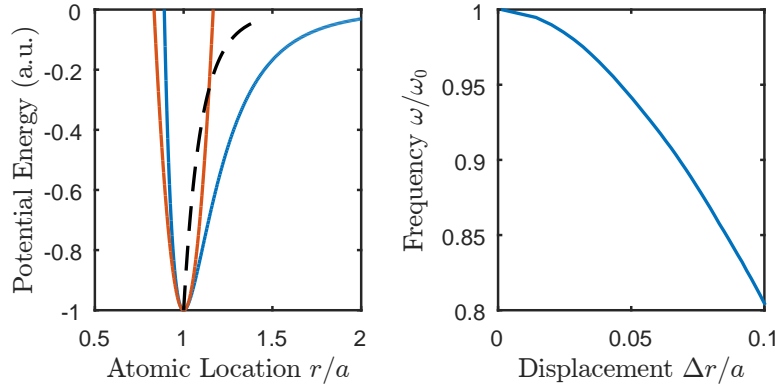


FIGURE 3.4: (a)(left) Harmonic and anharmonic Lennard-Jones potentials with average atomic position (dashed). (b) (right) Frequency vs atomic displacement showing how frequency softens as amplitude of atomic vibration (temperature) increases.

Using the peak position as a metric, temperature can be measured with Raman spectroscopy[38, 92, 130]. At room temperature and above, the peak frequency of the many semiconductors is proportional to sample temperature[113, 131–136],

$$\omega(T) = A(T - T_{ref}) + \omega_{ref}, \quad (3.1)$$

where A is a calibration constant, ω_{ref} is the measured peak position at reference temperature, T_{ref} , often room temperature. The calibration constant can be obtained by measuring the peak position of the material of interest as a function of temperature ($A = -0.022 \text{ cm}^{-1}/\text{K}$ for Si[130]). The peak position can then be used to measure the temperature of devices fabricated with the calibrated material.

Similarly, the peak position is dependent on the strain in the sample due to anharmonicity in the inter-atomic bonds[92, 130, 137]. Strain in a material forces

atoms away from their equilibrium positions. This causes them to rest at a different positions in the potential field which in general have a different curvature and thus force constant than equilibrium. A change in force constant in turn causes a shift in the frequency of the normal modes of the system, which is observed in the Raman spectra as a change in the peak positions. The Raman peak position shifts proportionally to the material strain so that the peak position as a function of strain and temperature is,

$$\omega(T, \varepsilon) = A(T - T_{ref}) + D\varepsilon + \omega_{ref}, \quad (3.2)$$

where D is a calibration constant for strain.

The Raman spectrum can also be used to quantify the composition of alloys[138–140]. As an elemental crystal is alloyed, the alloying species introduces a shift in peak positions through changes in the average mass and force constant. At the same time, the new species alters the phonon dispersion which can lead to additional peaks appearing in the Raman spectrum. The relative peak positions or the relative intensities of the peaks can be used as metrics to quantify both composition and strain simultaneously in alloys.

Since the exact form of the interatomic potentials is unknown, the peak position and intensity trends with composition are often calibrated to X-ray diffraction (XRD) data[138]. For example, the peak positions of the Si-Si and Si-Ge like modes in SiGe alloys follow the following empirical trends with Ge composition, x , and strain, ε ,

$$\omega_{SS} = \omega_{Si} - 70.5x - 830\varepsilon, \quad (3.3)$$

$$\omega_{SG} = \omega_{SiGe} - 16x - 575\varepsilon, \quad (3.4)$$

where $\omega_{Si(SiGe)}$ is the frequency of pure, fully relaxed Si(Si₅₀Ge₅₀) at room temperature, 520 and 400.5 cm⁻¹, respectively[138]. These equations can then be

rearranged so that x and ε can be determined from the peak positions in the Raman spectrum,

$$x = \frac{(\omega_{SG} - \omega_{SiGe}) - 0.6928(\omega_{SS} - \omega_{Si})}{64.84}. \quad (3.5)$$

When SiGe alloy films are grown on Si substrates, a strain in the alloy film results from the differences in interatomic bond length[141, 142]. As the film thickness increases, the stress also increases until the energy is released as dislocations. Depending on the growth temperature, the amount of relaxation at any thickness will vary. Therefore, a film can be grown at various strain states, which is quantified by the degree of relaxation of the film,

$$r = \frac{\Delta_{exp} - \Delta_s}{\Delta_r - \Delta_s} \times 100\%, \quad (3.6)$$

where $\Delta_r = 70.5x$, $\Delta_s = 36x$ are the peak shifts in the fully relaxed and strained state respectively, and $\Delta_{exp} = \omega_{SS} - 520 \text{ cm}^{-1}$ [138]. Knowing the relaxation state of a sample is important for quantifying the quality of the film since relaxation occurs through the formation of dislocations.

3.2.2 Linewidth

At the same time, the linewidth of the peak is dependent on temperature[92, 134, 138, 143]. The origin of this linewidth arises from the Heisenberg uncertainty principle, which states that for a given uncertainty in measured energy of a particle a minimum uncertainty in the lifetime of a state is achievable[144]. The experimental Raman peak has a finite width in energy, which is related to the uncertainty in the energy, $\Delta\epsilon$, so that the linewidth is directly related to the phonon lifetime as,

$$\Gamma \approx \Delta\epsilon = \frac{\hbar}{\tau}, \quad (3.7)$$

where \hbar is Planck's constant, $5.3 \text{ cm}^{-1} \text{ ps}$.

For bulk, defect free crystals, phonon-phonon scattering is the dominant scattering mechanism responsible for the temperature dependence of the linewidth. As the number of phonons available for scattering increases with temperature, following the Bose-Einstein distribution, so to does the probability of a scattering event. This increased probability reduces the phonon lifetime, yielding an increased linewidth. In the case of imperfect crystals, such as amorphous materials, disordered alloys and doped semi-conductors, the observed linewidth can be dominated by static imperfections that are not in general temperature dependent according to Eqs. 2.4-2.6. The temperature dependence of the linewidth therefore has two components; one temperature dependent and one temperature independent.

The linewidth of the Raman spectrum can be modeled from two perspectives; scattering or decay. The phonon scattering view point treats phonon scattering as thermal particles which scatter with each other and the host material. The phonon decay interpretation, on the other hand, treats Raman phonons as excited particles that decay to a lower state after scattering. The prior perspective employs Eqs. 2.3-2.6 and Matthiessen's rule to model the linewidth. The latter assumes that the decay mechanism is related to the population of the decayed state.

Klemens originally derived a model for the temperature dependence of the Raman linewidth using perturbation theory[145]. He considered the Raman linewidth to be related to the lifetime of the Raman optical phonons before decaying into acoustic phonons. This lifetime is related to the population of the final phonon states and thus to a summation of Bose-Einstein distributions. For decay paths from one optical phonon to two acoustic phonons (3-phonon process), the linewidth equals,

$$\Gamma^3(T) = \Gamma_0^3 \left(1 + \sum_{i=1}^2 \frac{1}{\exp\left(\frac{\hbar\omega_{f,i}}{k_B T}\right) - 1} \right) + \Gamma_0^I, \quad (3.8)$$

where $\omega_{f,i}$ is frequency of i th final phonon state, Γ_0^I is the temperature independent linewidth caused by static imperfections in the lattice, and Γ_0^3 is the 0 K phonon

linewidth in a perfect crystal[134, 143, 145]. The decay path of optical phonons must obey the same conservation of momentum and energy conditions discussed in Section 3.1. Because the Raman active mode originates from the zone center, total momentum of the final states must equal zero. Therefore, the final states are often assumed to have half the frequency of the Raman mode, i.e. $\omega_{f,i} = \omega_0/2$, with wavevectors q and $-q$. In this case, Eq. 3.8 becomes,

$$\Gamma^3(T) = \Gamma_0^3 \left(1 + \frac{2}{\exp\left(\frac{\hbar\omega_0}{2k_B T}\right) - 1} \right) + \Gamma_0^I, \quad (3.9)$$

where ω_0 is the Raman phonon frequency[134, 143, 145]. In some cases, higher order phonon scattering may significantly contribute to the linewidth, which can be accounted for by a 4-phonon term,

$$\Gamma^4(T) = \Gamma^3(T) + \Gamma_0^4 \left(1 + \frac{3}{\exp\left(\frac{\hbar\omega_0}{3k_B T}\right) - 1} + \frac{3}{\left(\exp\left(\frac{\hbar\omega_0}{3k_B T}\right) - 1\right)^2} \right), \quad (3.10)$$

where $\omega_{f,i} = \omega_0/3$, Γ_0^4 is the 4-phonon scattering component of the line width at 0 K[146]. Using these equations, the influence of each scattering type on the observed linewidth can be investigated through temperature dependent Raman measurements.

3.3 Fitting

In order to extract information, e.g. peak position and linewidth, from the Raman signal, a model function must be fit to the collected spectrum. Depending on the material properties, the peaks may have a wide variety of shapes caused by different physical principles and so an appropriate model function must be chosen.

For a perfect crystal, the real Raman signal will be a Lorentzian line shape[144]. However, due to the finite size of the probing laser spot and the finite resolution of the spectrometer, the measured signal will be convoluted with an additional width

caused by the instrument. Because of the Gaussian distribution of intensity in the laser spot, the measured line is often modeled by convoluting the Lorentzian with a Gaussian function resulting in the Voigt function[147],

$$I_V(\omega) = I_0 \int_{-\infty}^{\infty} G(\omega')L(\omega - \omega')d\omega', \quad (3.11)$$

where G is the Gaussian function, L is the Lorentzian function, I_0 is the peak intensity, ω is the frequency in cm^{-1} and ω' is an integration variable. Using this line shape, there will be two linewidths: one associated with the instrument broadening and one from the finite lifetime of the measured phonon. Additionally, there will be a broadening term from the discreteness of the data points mapping out the spectrum which is often absorbed into the Gaussian width of the Voigt function, but under certain conditions must be accounted for as will be discussed in Chapter 4.

In an imperfect crystal, the line shape may deviate from a perfect Lorentzian. For example, in amorphous or inhomogeneous materials, the phonon frequencies may have a distribution of frequencies due to the distribution of local atomic arrangements throughout the sample[98]. If the distribution of vibrational frequencies is Gaussian, then the signal will have a Voigt profile regardless of the instrument broadening. If the inhomogeneity results in a distribution of frequencies that is something other than a Gaussian, then the Lorentzian profile must be convoluted with that distribution.

In some cases, the spectrum may have an asymmetric shape. The two most common causes of this shape are phonon-electron interactions (Fano resonance) or a relaxing of selection rules caused by nanoscaling (phonon confinement effect). Fano resonance occurs when the discrete frequency of the phonon interacts with a continuum of electronic states[148–150]. The Fano function was derived from first principles to describe this phenomenon,

$$I_F(\omega) = I_0 \frac{(1 + 2(\omega - \omega_0)/Q\Gamma)^2}{1 + (2(\omega - \omega_0)/\Gamma)^2}, \quad (3.12)$$

where I_0 is the peak intensity, ω_0 is the peak frequency, ω is the frequency in cm^{-1} , Γ is the Lorentzian linewidth and Q is the Fano asymmetry parameter. It is often termed the asymmetric Lorentzian because in the limit of no electron-phonon interaction, $Q = \pm\infty$, the Fano function becomes a Lorentzian function.

When a material is nanoscaled it may also result in an asymmetry in the Raman peaks due to phonon confinement[100–102]. This is due to the vibrational modes no longer having plane-wave nature and so they may be described by a superposition of plane-waves resulting in an uncertainty, or finite distribution, in the wavevectors. This relaxes the selection rules of the Raman modes so that modes away from, but near, the zone center may participate in Raman scattering. Most often the optical mode at the zone center is the highest frequency mode and so representation of modes away from the zone center results in a low-frequency asymmetry on the Raman peak. Richter[100], and Campbell and Fauchet[101, 102] developed a phonon confinement model (PCM) to describe the asymmetry observed in the Raman spectra of nanoscaled systems,

$$I_{PCM}(\omega) = I_0 \int_0^1 \frac{|C(q)|^2 d^3q}{(\omega - \omega(q))^2 + (\Gamma/2)^2}, \quad (3.13)$$

where the integration is over the normalized Brillouin zone. Effectively, Eq. 3.13 is an infinite summation of a series of Lorentzians weighted by a Fourier series coefficient, $C(q)$, that depends on the geometry and dispersion, $\omega(q)$, of the nanoscaled system. The difficulty in using this model is that $C(q)$ is somewhat arbitrary since the weighting of wavevector contributions is unknown[102]. Additionally, the dispersion must be used in the model, and is often assumed to be the bulk dispersion of the material being investigated. However, as we discussed in Section 2.2, nanoscaling alters the dispersion. Therefore, there are significant uncertainties when using this equation, especially, in disordered samples where a dispersion cannot be defined.

The Raman spectra used in the following studies will be collected from single crystalline, compositionally disordered SiGe alloy films and the single crystalline

Si(100) substrate on which they are grown. The peak from the Si substrate can be very accurately fit using a Voigt function since the substrate is a pure crystal, however choice of model function for the SiGe is more difficult. The SiGe peak has a slight asymmetry likely due to disordered induced localization as well as phonon confinement caused by nanoscaling, as will be discussed in more detail later. Therefore, the PCM would be the natural choice for fitting to the SiGe peak. However, the PCM requires the dispersion as an input, and since the SiGe films are compositionally disordered, the dispersion of the optical modes cannot be well defined. Therefore, the asymmetry is chosen to be empirically fit using the Fano function. While this function is not designed to physically describe the asymmetry of our SiGe films, it provides a quantitative measure of important spectral parameters which can be discussed from a physical perspective.

3.4 Raman Experiments

Raman experiments were performed using a custom commercially built Renishaw InVia Raman microscope. The system is outfitted with 3 lasers and 4 wavelengths, 4 microscope objectives, polarization optics, 3 diffraction gratings, low and high temperature stages, a pump beam path and 3 probe beam paths. Additionally, the system can be coupled to an atomic force microscope (AFM) and scanning tunneling microscope (STM). With these capabilities, nearly every known form of continuous wave Raman spectroscopy can be performed, including resonant Raman, tip enhanced Raman and polarized Raman. This work primarily deals with temperature dependent, polarized, spontaneous Raman spectroscopy and this section outlines the operation of the system for these purposes.

3.4.1 Renishaw InVia Spectrometer

Figure 3.5 is an internal diagram of the InVia system. The light source for Raman experiments is one of 4 wavelengths (405, 488, 514, 785 nm) emitted from one of three lasers (405 nm diode, 488/514 nm Ar ion, 785 nm diode). Each laser has a different beam path between the laser and the objective. After the objective, the beam paths are the same for each laser, but the lens and grating positions are automated and are adjusted for the particular wavelength being used.

Probe light from the laser is injected into the spectrometer using two mirrors, one manually adjusted (M1), and one motorized and computer controlled (M2). Between the two mirrors are neutral density (ND) filters used to adjust the laser power and a shutter to block the beam. The two mirrors are needed to ensure the laser beam passes through the beam expander axisymmetrically. The beam expander corrects for any divergence of the beam out of the laser, i.e. collimates the beam, and expands the cross-sectional diameter of the beam to equal the back aperture of the objective. A pin hole can drop into place between the two lenses of the beam expander to both clean up the shape of the beam and to assist in alignment of the laser through the center of the beam expander. A pin hole can drop into place between the two lenses of the beam expander to both clean up the shape of the beam and to assist in alignment of the laser through the center of the beam expander.

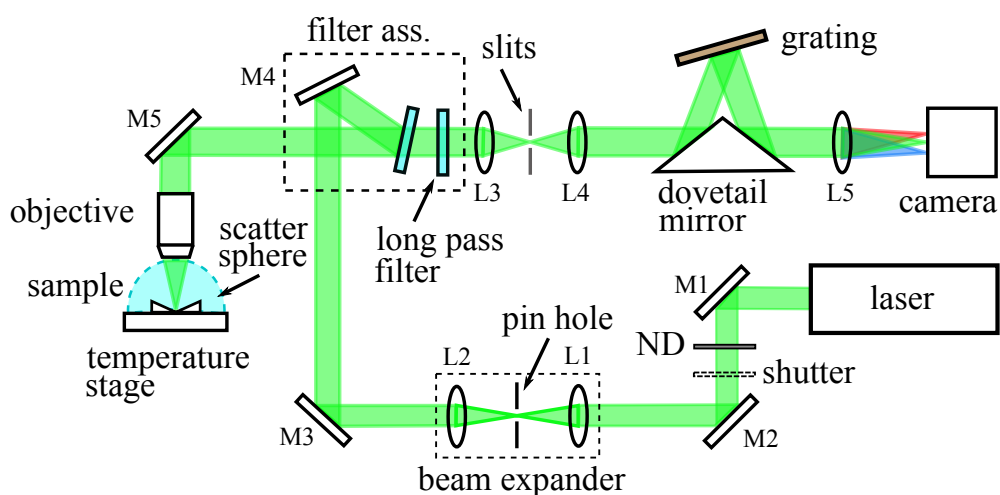


FIGURE 3.5: Internal diagram of Renishaw InVia Raman microscope.

After the beam expander, the beam is directed by a motorized mirror (M3) into a filter assembly, composed of a manual mirror (M4) and two long pass filters. After reflecting off M4, the first long pass filter reflects the laser light onto a fixed mirror (M5) and into the back of the objective which focuses the beam to a roughly $1 \mu\text{m}$ spot on the sample. The two adjustable mirrors, M3 and M4, after the beam expander are needed to ensure the laser beam is aligned through the objective axisymmetrically.

The incident light impinges on the sample, resulting in reflected light, Rayleigh scattered light and Raman scattered light. Since Raman and Rayleigh scattered light scatters in a random direction, a sphere of scattered light is generated centered at the laser focal point on the sample surface. The fraction of light collected from the sphere depends on the numerical aperture (NA) of the objective. The fraction of collected light is equal to the solid angle collected by the objective divided by the solid angle of a sphere. The solid angle of light collected by the objective is directly related to the numerical aperture of the objective, so that the fraction of light collected is,

$$\frac{I_{\text{collected}}}{I_{\text{generated}}} = \frac{2\pi f^2(1 - \cos(\theta))}{4\pi f^2} = \frac{1 - \cos(\sin^{-1}(\text{NA}))}{2}, \quad (3.14)$$

where f is the objective focal length and $\theta = \sin^{-1}(\text{NA})$ is the half angle of the objective acceptance cone, see Fig 3.6(a). Additionally, the laser spot diameter, $2w_0$, and depth of field, DOF, depend on NA[153], which influence the lateral and depth resolution of the microscope as well as laser heating,

$$2w_0 = \frac{4\lambda_L \cos(\sin^{-1}(\text{NA}))}{\pi \text{NA}} \quad (3.15)$$

$$\text{DOF} = \frac{8\lambda_L}{\pi} \left(\frac{\cos(\sin^{-1}(\text{NA}))}{\text{NA}} \right)^2, \quad (3.16)$$

where λ_L is the laser wavelength.

The collected light then passes through the objective and is directed back to the long pass filters. Long pass filters reflect all light with a wavelength at or shorter

than a chosen wavelength and transmits any light with a longer wavelength. The cutoff wavelength of the filter is selected to be slightly longer than the chosen laser wavelength to prevent the strong Rayleigh signal from overwhelming the weak Raman signal. As a result, the sample reflected laser light, Rayleigh scattered light and anti-Stokes light is reflected back down the injection path, while the Stokes scattered light passes through the filters.

The Stokes light then passes through a lens (L3) which focuses the light onto the entrance slit. The entrance slit is composed of two motorized razor blades that move independently so that the center and width of the entrance slit can be adjusted. The entrance slit is designed to reject any light that comes from locations other than the focal plane of the objective. The slit along with the camera are used to adjust the confocality, i.e. spectrometer depth resolution, as will be discussed later in this section.

After passing through the slit, the light is recollimated and expanded to the size of the diffraction grating area by a second lens (L4). The collimated Raman light then reflects off the dove tail mirror onto a diffraction grating which disperses each wavelength of light at a different angle, while keeping each wavelength collimated. Diffraction gratings are designed to reflect light in such a way so that each wavelength constructively interferes in certain well defined directions and destructively in all others. Due to the differences in wavelength, the angle at which each wavelength constructively interferes will be different, leading to a separation of wavelengths. There are three gratings purchased for this system which can be defined by the blaze angle and groove density (1200 g/mm, 3000 g/mm and 1800 g/mm).

A diffraction grating is made up of a highly reflective material where a series of closely packed grooves have been etched into the surface. The groove density for a specific blaze angle is used to define the separation of each wavelength in angle, also known as the grating dispersion. The higher the groove density, the greater the dispersion. The blaze angle defines which wavelength will most efficiently

constructively interfere for a defined diffraction order. Therefore, gratings that have been blazed for light in the IR may not be applicable for separating wavelengths in the UV. The 1800 and 3000 g/mm gratings were blazed for UV-visible light while the 1200 g/mm grating was blazed for near IR light.

After light is separated by the grating, dispersed light is finally collected by a lens (L5) and focused onto a thermoelectrically cooled charge couple device (CCD) camera. The CCD chip in a CCD camera used for Raman spectroscopy or other low light applications is often made of an array (1040×256) of metal-oxide-semiconductor capacitors, which each act as a pixel of the camera. When a Raman photon impinges on one of the pixels, it excites an electron out of the valence band which is then stored in the capacitor. As long as the shutter is open and the laser is on, Raman light is collected by the CCD camera so that the charge built up on each capacitor is proportional to the number of photons absorbed. Since the light is first reflected off a diffraction grating and passed through a focusing lens, each pixel on the vertical axis of the CCD chip represents a narrow range of wavelengths. The charge stored in each pixel then equals the number of Raman photons within a small range of wavelengths and the whole array is a discretized representation of the Raman spectrum. The horizontal axis of the CCD chip acts as a virtual vertical entrance slit, complimenting the physical horizontal entrance slit previously described. The camera is thermoelectrically cooled to -78 °C because thermal energy can excite electrons out of the valence band of each pixel leading to noise in the spectrum. Often, cameras used in Raman applications are cooled using liquid nitrogen to further minimize noise.

3.4.2 Raman Penetration Depth

A Raman signal is generated throughout the entire volume in which light penetrates into a material. For thin films, the depth of this volume may be larger than the film thickness leading to a signal being generated from the substrate in

addition to the film. To remedy this problem, a laser with a shorter wavelength may be used since shorter wavelengths often have smaller penetration depths than longer wavelengths. Here, the influence of wavelength on Raman penetration depth is presented with emphasis on wavelengths equipped by the Raman system at UVA and SiGe alloy film thicknesses studied in this work.

When light impinges on a material it is absorbed so that the light intensity exponentially decays into the material following the Beer-Lambert Law,

$$I_{BL} = \exp(-\alpha(\lambda)z) \quad (3.17)$$

where $1/\alpha(\lambda)$ is the wavelength dependent optical penetration depth of the material, δ_p . Since Raman light is generated where light is absorbed in the material, the Raman light that is collected by the spectrometer must be Raman light that escapes the film and re-enters the objective. Ignoring optical geometries and assuming that all Raman light generated takes the same path as the incident light but reverse, the Raman light collected will be the multiplication of two exponentials, Eq. 3.17,

$$I_R = \exp(-2\alpha(\lambda)z), \quad (3.18)$$

so that the effective Raman penetration depth is half of the incident light penetration depth[151, 152].

The penetration depth can be calculated using either the complex dielectric function, $\tilde{\epsilon} = \epsilon_1 + i\epsilon_2$ or the complex index of refraction, $\tilde{n} = n + i\kappa$, shown for Si and Si₈₀Ge₂₀ in Table 3.1. The index of refraction and dielectric function are related by the following functions[153],

$$n = \sqrt{\frac{\sqrt{\epsilon_1^2 + \epsilon_2^2} + \epsilon_1}{2}} \quad (3.19)$$

TABLE 3.1: Penetration depth and complex index of refraction for Si and Si₈₀Ge₂₀ at various wavelengths[6, 7].

laser wavelength	Si ₈₀ Ge ₂₀			Silicon		
	n	κ	δ_p	n	κ	δ_p
405 nm	6.28	0.55	59 nm	6.03	0.34	95 nm
488 nm	4.84	0.13	297 nm	4.63	0.13	412 nm
514 nm	4.59	0.11	376 nm	4.41	0.09	457 nm

TABLE 3.2: Percent of Raman light generated by a cumulative depth at various wavelengths in Si₈₀Ge₂₀ calculated using Eq. 3.18.

laser wavelength	50%	63%(1/e)	86%(1/e ²)	93%(1/2e ²)
405 nm	20 nm	29 nm	58 nm	79 nm
488 nm	103 nm	148 nm	295 nm	398 nm
514 nm	129 nm	186 nm	370 nm	493 nm

$$\kappa = \sqrt{\frac{\sqrt{\epsilon_1^2 + \epsilon_2^2} - \epsilon_1}{2}}. \quad (3.20)$$

Using the refractive index, the laser optical penetration depth is calculated using,

$$\delta_p = \frac{\lambda_L}{4\pi\kappa}, \quad (3.21)$$

where λ is the laser wavelength.

To determine where the majority of Raman light is generated for each wavelength, we then must calculate the sum of the signal from each planar depth to calculate the percent contribution for each thickness. The results for Si₈₀Ge₂₀ are shown in Table 3.2. As we can see, even though the penetration depth of the 405 nm laser is 59 nm, 50% of the Raman light generated is from the top 20 nm of the sample as compared to 103 nm for the 488 nm laser. One of the SiGe films being investigated in this work is 40 nm thick, meaning 75% of the Raman signal will be generated from the film and only 25% from the substrate when using the 405 nm laser, and vice versa when using the 488 nm laser. We may then selectively probe layers by varying the wavelength of the Raman light source.

3.4.3 Confocality

Due to the finite penetration depth and spot size of the laser, a Raman signal is generated throughout a volume of the sample. Collecting a signal from a large volume can cause problems when attempting to measure properties of thinly layered materials or surfaces. When the collection volume is larger than the region of interest, a Raman signal will be collected from multiple regions or materials which may interfere with the spectrum of interest, as will be discussed more thoroughly in Chapter 4. Additionally, collecting light from a large volume convolutes an additional broadening with the natural Raman line width. By operating the spectrometer in high confocal mode, scattered light originating away from the region of interest can be minimized.

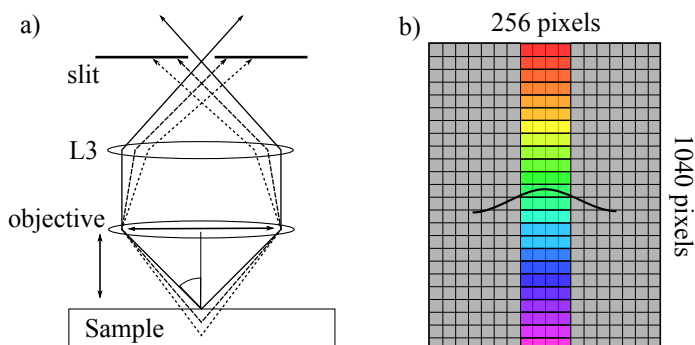


FIGURE 3.6: (a) Diagram of confocal Raman setup with objective lens (b) and CCD camera chip. The entrance slit of the spectrometer and CCD chip filters out Raman scattered light generated from areas away from the objective focal point.

Briefly mentioned earlier in this section, the spectrometer entrance slit and CCD chip act as filters to reject Raman scattered light not originating from a small volume near the focal point of the objective. Figure 3.6 (a) is a diagram of light collected by the objective and filtered by the entrance slit. Light is generated at several depths in the sample. When the objective is focused on the sample surface, i.e. the distance between the objective and sample surface is equal to the objective focal length, light from the focal point will be imaged at the focal plane of the entrance slit. All light from the focal point of the objective will therefore pass through the entrance slit.

Light originating from deeper in the sample will be imaged in front of the entrance slit, so that only some of the light passes through the slit. The deeper in the sample the light is generated, the less light passes through the slit. The contribution of light from away from the focal point can be adjusted through the entrance slit width.

The entrance slit is a horizontal slit so it only rejects light in the vertical direction at the focal plane of the slit and CCD chip, or spectral direction on the CCD chip. In order to reject light in the horizontal direction, a second vertical slit must also be used to create a rejection square, or pin hole. Two slits cannot be placed at the same focal plane because of the finite size of the slit mechanisms. Therefore, the second slit must be placed at a second focal plane. The only other focal plane in the spectrometer is at the CCD camera, where it is impossible to add a physical slit. Instead, the chip itself can be used as a virtual vertical slit, by only collecting the signal from a small range of pixel columns instead of the entire 256 columns, as shown in Fig. 3.6 (b).

High confocal mode reduces the entrance slit width from the normal $50\ \mu\text{m}$ to $25\ \mu\text{m}$ and reduces the width of the CCD virtual slit from 8 pixels to 2. The minimum spatial resolution achievable through confocal techniques is greater than or equal to $1\ \mu\text{m}$. To further improve spatial resolution, the laser wavelength can be selected to adjust the Raman penetration depth which will be the subject of Chapter 4.

In addition to influencing spatial resolution, adjusting the entrance slit changes the instrument broadening of the spectral peak width. When all lenses are at the correct focal points, as is the case for our spectrometer, an image from one focal plane will be imaged at another focal plane. Therefore, the image at the entrance slit, a superposition of defocused images of Raman light originating below the objective focal point and the focused image at the focal point, will be imaged onto the CCD chip. The shape of the defocused Raman image at the focal plane of the entrance slit will be a superposition of 2-dimensional Gaussians where the Gaussian width increases proportional to the originating depth of the signal.

These broad Gaussians convolute with the natural linewidth of the Raman signal

to artificially broaden it. If the Gaussian broadening is much larger than the natural linewidth, then the natural linewidth can be difficult to deconvolute. By narrowing the entrance slit, the components of the Gaussian in the spectral direction wider than the entrance slit will be rejected leading to a narrowing of the spectral peaks. However, this also reduces the signal intensity resulting in a lower signal to noise. So, a balance between signal and Gaussian broadening must be achieved.

In this work studying SiGe alloys using a 405 nm laser, the ideal confocal settings are a 25 μm slit width and 8 pixel CDD chip read out. Since the Raman penetration depth using the 405 nm laser, ~ 60 nm, is much smaller than the confocal spatial resolution, ≥ 1 μm , high confocal mode will not improve the spatial resolution. However, narrowing the entrance slit will reduce the instrument broadening of the Raman peak. Therefore, the entrance slit was reduced to improve extraction of the SiGe linewidth, while the virtual CCD slit was adjusted to maximize the signal throughput.

Chapter 4

Limits of Phonon Linewidth Measurements

4.1 Motivation

Most often, Raman optical phonon linewidth studies are performed on samples thick enough that a Raman signal from the substrate is not generated or the substrate is selected so that its Raman signal is not close in frequency to the signal of interest. For some thin film samples, however, it is not possible to select a substrate that does not have an interfering Raman signal. For example, SiGe alloy thin films grown on Si, which will be the focus of the following studies, suffer from both of the described conditions. The film is thin enough that a substrate signal is generated and the substrate signal is close in frequency to the film signal, making it difficult to deconvolve the two signals.

The two spectroscopic properties of interest when attempting to separate overlapping signals are spectral and spatial resolution. In Raman spectroscopy, spatial resolution is the ability to preferentially collect signal from the area of interest (thin film) and reject signals from other parts of the sample (substrate). Spatial resolution is important because all lasers penetrate into the probed sample

to some finite depth thus generating a Raman signal through the entirety of that depth as discussed in Section 3.4. If the film is thinner than this penetration depth, then a Raman signal from the substrate will be generated in addition to the Raman signal from the film. If these signals are close in frequency, it may be difficult to accurately measure phonon lifetimes due to signal convolution. Spectral resolution on the other hand is the ability to discern two Raman peaks that are close in frequency. In such a case, a spectrometer with low spectral resolution can cause the peaks to broaden and blur together making it impossible to accurately fit a model function and extract pertinent peak parameters.

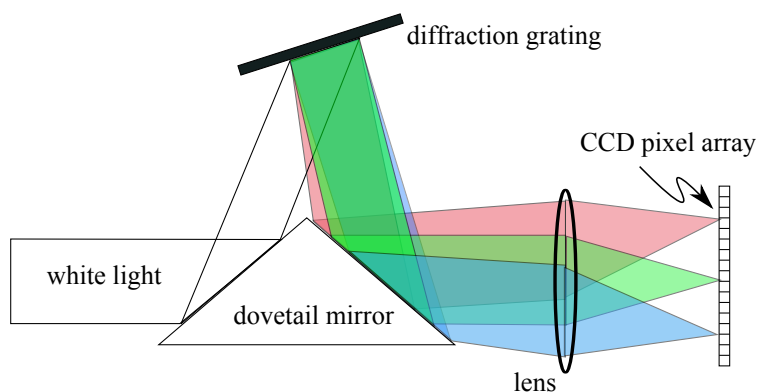


FIGURE 4.1: As the angle at which light is dispersed by the grating increases, the spectral resolution of the spectrometer increases because there are fewer wavelengths per pixel.

The two most important experimental parameters in determining spatial and spectral resolution are the laser wavelength and grating dispersion angle. The grating dispersion angle determines how far the wavelengths of light are separated on the CCD camera pixel array. The greater the degree of separation, the higher the spectral resolution since there are fewer wavelengths falling on each pixel of the camera, see Fig. 4.1. This in turn means that there are more pixels, or data points, mapping out the Raman peak improving the fitting ability. While the grating primarily affects the spectral resolution of the Raman system, the laser affects both the spectral and spatial resolutions. As a rule of thumb, the shorter the laser

wavelength, the smaller the penetration depth and smaller the laser spot on the sample, which improves the resolution on both the surface and depth of the sample. This means that for short wavelengths more of the signal will be generated in the film than the substrate when compared to longer wavelengths. However, since the Raman spectrum is based on energy shifts (for Si the shift is 0.06 eV or 520 cm^{-1}), a lower wavelength laser will yield a lower energy or spectral resolution, since the grating dispersion is roughly a constant wavelength per pixel. This means that when using a lower wavelength laser to improve spatial resolution, the spectral resolution will decrease unless a higher resolution grating is used to compensate. Alternatively, the grating can be operated at different diffraction orders to improve resolution.

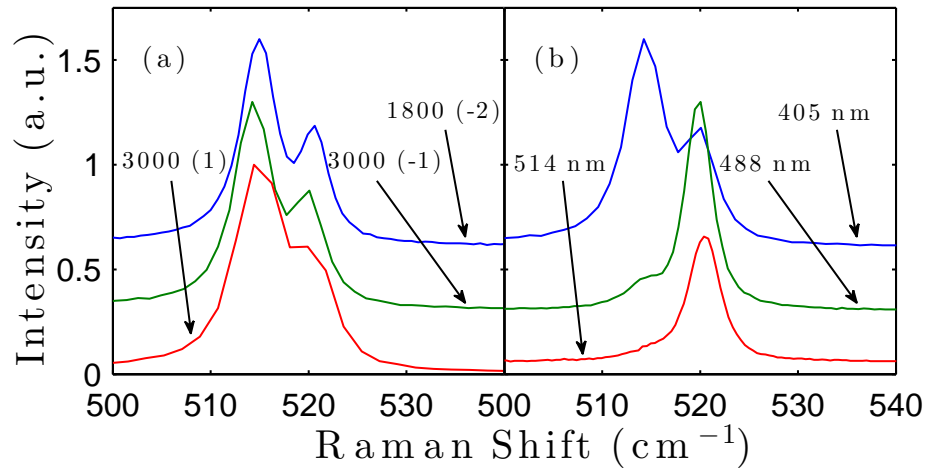


FIGURE 4.2: (a) The Raman spectra of a 39 nm $\text{Si}_{80}\text{Ge}_{20}$ thin film on Si taken using the 405 nm laser with three grating combinations are shown. We can see that as the resolution of the grating increases the peaks narrow and become more distinct. (b) The Raman spectra of 39 nm $\text{Si}_{80}\text{Ge}_{20}$ thin film on Si taken using the 405, 488 and 514 nm lasers with the 3000 g/mm (-1) grating are shown. As the wavelength decreases, the spatial resolution increases by more than an order of magnitude but the spectral resolution is reduced by a factor of 3.

A diffraction grating is based on the principle of wave interference. Due to the difference in wavelength, each wavelength constructively interferes at different discrete angles allowing for wavelength separation. The first angle of constructive interference is the zeroth order where the grating acts like a mirror. The next, and most efficient, and thus brightest, is the 1st order. The next, mirrored in angle

TABLE 4.1: The spectral resolutions, in $\text{cm}^{-1}/\text{pix}$, of three lasers with three different grating types, where the number in parenthesis is the order the grating is operated in. The relative Raman intensities of the 40 nm thin film $\text{Si}_{75}\text{Ge}_{25}$ (Sample 5) alloy peak and Si substrate peak is included as an indication of spatial resolution.

	I(SiGe)/I(Si)	1800 g/mm	3000 g/mm (+1)	3000 g/mm (-1)	1800 g/mm (-2)
405 nm	2.21		1.84	1.16	0.71
488 nm	0.10	2.24	1.12	0.56	
514 nm	0.07	1.99	0.95	0.40	

across the zeroth order, is the -1 order and following the same pattern, the 2nd and -2, 3rd and -3 and so on. Most often, diffraction gratings are operated using the 1st order diffraction because they are the most efficient at that order, however, they also have the lowest dispersion. Therefore, it is possible to improve the spectral resolution of the spectrometer by operating the grating at a higher order albeit at the cost of signal intensity.

The Raman microscope at UVA is uniquely equipped to explore and take advantage of such principles, since it is equipped with 4 unique wavelengths (405, 488, 514 and 785 nm)¹ and 3 gratings (1200, 3000 and 1800 g/mm). In order to demonstrate these concepts, Raman spectra were acquired on a 39 nm $\text{Si}_{80}\text{Ge}_{20}$ alloy thin film grown on Si at several wavelengths using different diffraction orders of the grating. The results are plotted in Figs. 4.2(a) and (b) and tabulated in Table 4.1.

It is clear from the relative intensities of the film peak ($\sim 515 \text{ cm}^{-1}$) and substrate peak ($\sim 520 \text{ cm}^{-1}$) plotted in Fig. 4.2 and listed in the first column of Table 4.1, that lower wavelengths significantly improve spatial resolution so that the Raman signal from the film is preferentially selected. However, the spectral resolution of the film is reduced by a factor of two when using the 3000 g/mm(+1) grating and by a factor of three when using the 3000 g/mm(-1) grating. For this reason it was necessary to use higher order diffraction when using the 405 nm laser. This could not be accomplished using the 3000 g/mm grating because of the inefficiency at such high diffraction order. However, the 1800 g/mm provided nearly a factor of two improvement and much less

¹The penetration depth of the 785 nm laser is far too large to be used with 40 nm SiGe film and so will not be used in this study.

signal reduction when using the -2 order.

Qualitative differences based upon laser wavelength and grating are self evident upon inspection of Fig. 4.2. The following examines the quantitative impacts of these differences in the measurement of Raman linewidths. In order to do this, we need to first understand how spectral resolution affects the Raman signal of a single peak. We can then investigate how fitting two overlapping spectra influence line width extraction. Finally, we can investigate the two simultaneously. Ultimately, the purpose of this study is to help the Raman spectroscopist tailor their experiment through selection of laser wavelength, resolution and noise to minimize uncertainties in linewidth measurements of a nanoscaled materials.

4.2 Experiment

Raman spectra were acquired on a series of SiGe alloy thin films on Si substrates with various thicknesses. The spectra were collected using a series of laser wavelengths and gratings to study the impact of spectral and spatial resolution on linewidth uncertainties. Using this data and models of the Raman spectra based on this data, we assess the impact of the experimental conditions on measuring these parameters. This section outlines the collection of these spectra.

Spatial resolution is quantified in our Raman signal by the relative peak intensity (RPI) of the film to substrate peak. As previously mentioned, the RPI is not affected by the grating selection but only the laser wavelength. However, we can also influence the RPI of our signal through the thickness of the sample. Due to the finite Raman penetration depth, as the sample thins, more signal is generated by the substrate, which causes a decrease in RPI. In order to create more data points along the RPI axis, a range a wavelengths and gratings as well as a range of SiGe film thicknesses (40, 90 and 210 nm) were investigated².

²The details of sample growths and characterization are discussed in Chapter 6

TABLE 4.2: Combinations of laser wavelength, grating and sample thickness used for linewidth uncertainty measurements of Si and Si₇₅Ge₂₅ with thicknesses 20, 90 and 210 nm (Samples 5-7). X symbolizes laser wavelength and grating combinations that will not be collected. ✓ indicates laser and grating combinations for which data was collected and the number in parenthesis is the RPI.

Silicon	1800 g/mm	3000 g/mm	3000 g/mm (-1)	1800 g/mm (-2)
405 nm	X	✓	✓	✓
488 nm	✓	✓	✓	X
514 nm	✓	✓	✓	X
$d = 40$ nm	1800 g/mm	3000 g/mm	3000 g/mm (-1)	1800 g/mm (-2)
405 nm	X	✓(6.28)	✓(5.50)	✓(5.29)
488 nm	✓(0.12)	✓(0.10)	✓(0.10)	X
514 nm	✓(0.08)	✓(0.06)	✓(0.06)	X
$d = 90$ nm	1800 g/mm	3000 g/mm	3000 g/mm (-1)	1800 g/mm (-2)
405 nm	X	✓(∞)	✓(∞)	✓(∞)
488 nm	✓(0.37)	✓(0.30)	✓(0.29)	X
514 nm	✓(0.19)	✓(0.17)	✓(0.16)	X
$d = 210$ nm	1800 g/mm	3000 g/mm	3000 g/mm (-1)	1800 g/mm (-2)
405 nm	X	✓(∞)	✓(∞)	✓(∞)
488 nm	✓(1.09)	✓(0.91)	✓(0.87)	X
514 nm	✓(0.58)	✓(0.48)	✓(0.45)	X

The laser wavelength, grating and sample combinations that were used are outlined in Table 4.2 with the RPI included in parenthesis. Note that the peak intensities change with the grating for a specific sample and laser wavelength. This is because as the resolution decreases, more wavelengths are binned in each pixel causing the peaks to blur together and artificially change the real RPI. For the 405 nm laser and 90 and 210 nm thick samples the intensity is ∞ since no substrate peak is observed due to the Raman penetration depth being smaller than the sample thickness.

When collecting Raman data, it is imperative that the experiment itself does not influence the measured results. Since heating influences the Raman linewidth, we must be careful not to heat the sample with the probing laser. Laser heating of Si and SiGe will be thoroughly discussed in the following chapter. The laser power used was determined by reducing the laser power with ND filters until shifts in peak position and linewidth were no longer observed with a further decrease in power.

When performing a Raman experiment, every material/sample will yield a different signal strength for a particular set of experimental settings. This is because every material has a different Raman cross section or efficiency. The Raman cross section is a measure of the probability that a single incident photon of a particular wavelength will be converted to a Raman photon. Therefore, Si and every SiGe alloy will have a different Raman cross section and thus a different spectral intensity. If we assume that the noise of the spectrometer is a constant for each grating, then each laser wavelength, grating and sample will have a different amount of noise for the same collection time and laser power. Increasing the laser power will increase the signal relative to the noise, however this can also lead to sample heating, which artificially changes the measured linewidth.

Since the uncertainty of the fit is directly related to the noise in the signal, the collection/integration time of each laser wavelength, grating and sample combination was selected to have as close to the same noise as possible. The noise to signal ratio (N/S) was calculated by first subtracting the baseline and then normalizing the spectrum to a peak intensity of one. Due to the very complex spectral structure of both Si and SiGe below 520 cm^{-1} , the baseline was calculated between the region 600 and 750 cm^{-1} . Since this region had very small slopes in all spectra, the baseline was not fit to a linear function, as is normally the case. Instead, the average value of the baseline region was subtracted as a constant from the spectrum. After normalizing, the standard deviation of the pixel intensities in the baseline region was used as the noise level. A N/S value of 0.0025 was chosen because it is a moderate N/S ratio for a Raman spectrum that is achievable under non-ideal conditions, such as when using a grating in a higher order diffraction while taking data through the window of a temperature stage at high temperatures.

The specific integration time of each experimental setting and sample combination was determined by setting the laser power to the non-heating value and calculating N/S for integration times ranging from 1 to 200 seconds. The results of the N/S

measurements versus integration time are plotted in Fig. 4.3 for Si spectra taken using the 488 nm laser. As expected, the N/S decreases with increasing integration time. However, due to the exponential decay, after a certain point increasing the integration time minimally improves the N/S ratio. This means that after a certain integration time it makes more sense to take another spectrum rather than double the time. This will be helpful in guiding future experiments when attempting to minimize uncertainties. Note however, that this critical integration time will be different for each sample, laser wavelength, grating and objective condition. Therefore, this N/S test must be performed for each experiment. Also note that operating the diffraction grating in a higher order leads to a significant increase in noise. Therefore, improved resolution can come at the cost of higher noise making the choice of experimental conditions difficult.

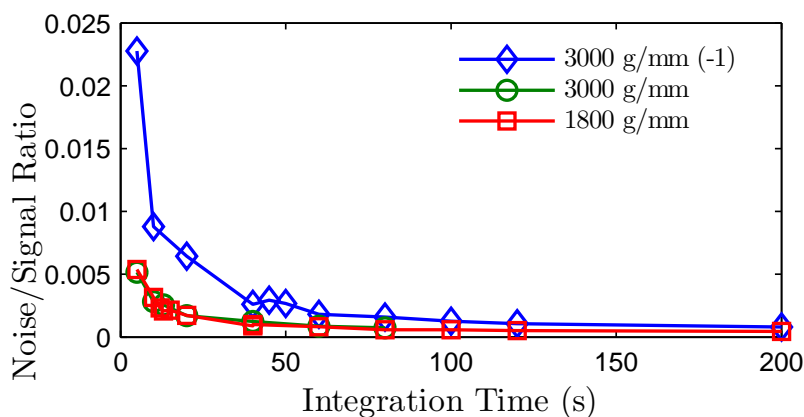


FIGURE 4.3: Change of N/S ratio with changing integration time using Si, 488 nm laser, 50x objective and various grating conditions.

Since each sample has a different cross section, thermal conductivity and thickness, the maximum laser power that did not lead to observable sample heating as measured by the peak position was individually selected for each sample in Table 4.2, followed by a N/S test to determine the integration time needed. A spectrum was then collected 25 times at the same location on the sample. The spectra were fit in the range of 490 to 530 cm^{-1} to a two peak function consisting of an asymmetric Lorentzian for the

alloy peak and a Voigt for the Si substrate peak. The function parameters were bound to make sure correct local minima were achieved. In the case of Si the alloy peak intensity was bound to 0.001 to effectively remove it from the function. Similarly, the substrate peak intensity was bound to 0.001 when no substrate peak was observed.

The Si data collected from this experimental section will be used as inputs for our model simulating a Raman experiment. This model will then be used to simulate the uncertainties in measuring linewidths of two peak Raman spectra of thin film SiGe alloys on Si substrates. The uncertainty results of the two peak simulations will then be compared to experimental SiGe thin film measurements as verification of our simulation results. We will then use the simulation results to comment on the best experimental conditions to minimize uncertainties.

4.3 Modeling the Experiment

In order to simulate the effects of spectral and spatial resolution on linewidth measurement uncertainties, the signal must first be accurately modeled. Spatial resolution is straight forward since it simply increases the RPI. Spectral resolution, on the other hand, is not so straight forward as it changes the binning of light on the CCD array in a fairly complicated way. Finally, and most importantly, we must accurately model the simulated noise.

4.3.1 Experimental Theory

The linewidth of a measured Raman signal is the convolution of two broadening components: the natural linewidth and instrument broadening. The natural linewidth is the physical spectral width of the Raman peak before it is passed through the spectrometer and is related to the scattering rate of the phonons in a high purity crystal, as discussed in Chapter 3. Instrument broadening, convolutes an additional broadening caused by the finite size of the Gaussian laser spot on the sample and the

finite spectral resolution of the CCD array. Both the Gaussian broadening and the spectral resolution affect linewidth uncertainties. As Gaussian broadening increases, the relative contribution of the natural linewidth to the measured signal FWHM diminishes leading to uncertainties in the deconvolution. Spectral resolution on the other hand controls the number of data points mapping out the peak curve. The fewer data points, the more pixelated the peak and the less confidently a model function can be fit to the signal to extract the natural linewidth.

As long as the sample is not heated by the laser, the natural linewidth does not change with laser wavelength³ and is not affected by the grating. Instrument broadening and spectral resolution on the other hand, changes with both the laser wavelength and grating. When the laser is focused on the surface of the sample, the laser spot has a finite Gaussian width determined by the diffraction limit of that objective and wavelength. When the grating of the spectrometer is operating in the zeroth order, the spectrometer acts as a very expensive microscope. The image of the laser spot on the sample is magnified by ~ 10 times on to the CCD chip. Since the laser spot is a Gaussian spot in both the x and y directions, a magnified Gaussian spot will be imaged on the CCD camera in both the spectral (y-direction) and spatial direction (x-direction).

If we move the grating so that it is operating in the first order and if our Raman signal has 3 discrete wavelengths, then the image on the camera will have 4 Gaussian spots; one for the laser and 3 for each Raman wavelength located at different location of the CCD pixel array along the y-direction corresponding to their wavelength. In a real Raman spectrum, the Raman signal is composed of a continuous range of wavelengths, the range of which is quantified by the natural linewidth. Therefore, each infinitesimally narrow range of wavelengths of the natural linewidth will be broadened by the Gaussian image of the spot on the camera. This is identical to the mathematical convolution of a Gaussian function with whatever function describes the

³This assumes that resonance effects do not change the shape of the Raman line.

natural line shape of the sample. In silicon, the natural line shape can accurately be described by a Lorentzian function and so the silicon Raman spectrum is ubiquitously modeled using a Voigt function, Eq. 3.11.

This broadening can be modeled for various resolutions if we know the Gaussian width of the laser spot image on the CCD array and if we know the resolution of the laser, grating and camera combination. In theory we just need to multiply the laser spot image Gaussian width in pixels by the resolution of our experiment in units of wave number per pixel (cm^{-1}/px) to get the instrument broadening caused by the laser spot size. Note that the resolution changes across the CCD array due to the spherical optics projecting on a flat surface. Therefore, the resolution value must be selected from the center pixel closest to the Raman peaks of interest.

The second instrument broadening component, binning, artificially broadens the peak by integrating the signal in discrete chunks. In most cases the Gaussian component of the Voigt function absorbs this extra broadening. However, it can be deleterious for very narrow linewidths or when peaks are very close together. This effect is easily modeled by binning the continuous model function into bins with the same size as the resolution.

4.3.2 One Peak (Si)

Silicon (100) was used as a control to apply these concepts and adjust the simulation parameters before applying them to a more complex two peak system. To do this, the effect of resolution on the experimental and simulated Raman linewidths were compared to confirm correct modeling. The simulated noise was then compared to noise observed in experimental Raman spectra of Si. Ultimately, it was found that resolution had a slightly stronger effect on linewidth uncertainties than noise. Therefore, minimizing uncertainty should begin with selecting the highest resolution experimental condition, unless it results in a disproportionate increase in noise.

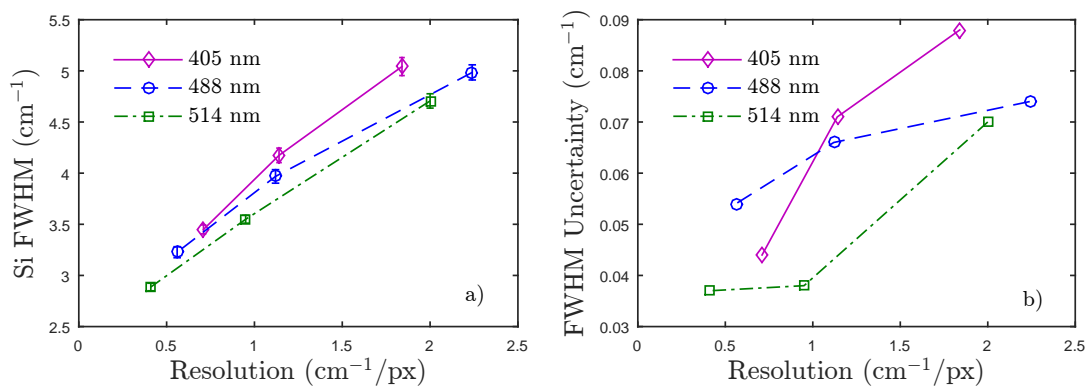


FIGURE 4.4: (a) Total FWHM of silicon as a function of spectrometer resolution when using the 405, 488 and 514 nm lasers. (b) Corresponding uncertainties in the FWHM of Si showing how worsened resolution leads to larger uncertainties.

Figure 4.4 a) plots the FWHM⁴ of Si as a function of resolution for each wavelength studied (405, 488 and 514 nm). As the resolution worsens (increases), the FWHM increases linearly for each wavelength. This is due to the natural linewidth of the Raman spectrum being convoluted with the instrument broadening Gaussian which is then binned into discrete pixels. As the resolution worsens the pixels bin a larger range of wavelengths, thus artificially broadening the peaks. Additionally, the Gaussian FWHM of the instrument broadening is a fixed value in space for each wavelength. So as each pixel represents more wavelengths, the Gaussian component becomes larger relative to the natural linewidth of the Raman peak. Figure 4.4 b) shows that this worsening resolution also leads to a general increase in uncertainty of the measured FWHM due to the reduced number of pixels mapping out the peak and the increased Gaussian component of the linewidth.

The Gaussian and Lorentzian FWHMs can be separated using the Voigt function to show how each changes with resolution. Figure. 4.5 shows that as the resolution worsens, the Gaussian linewidth broadens while the Lorentzian linewidth remains constant as expected. It was previously hypothesized that the Gaussian width would

⁴Three linewidths will be mentioned during this study, FWHM, Gaussian FWHM and Lorentzian FWHM. The FWHM represents the total measured linewidth of a spectrum, the Gaussian FWHM is the instrument broadening FWHM and the Lorentzian FWHM represents the natural linewidth.

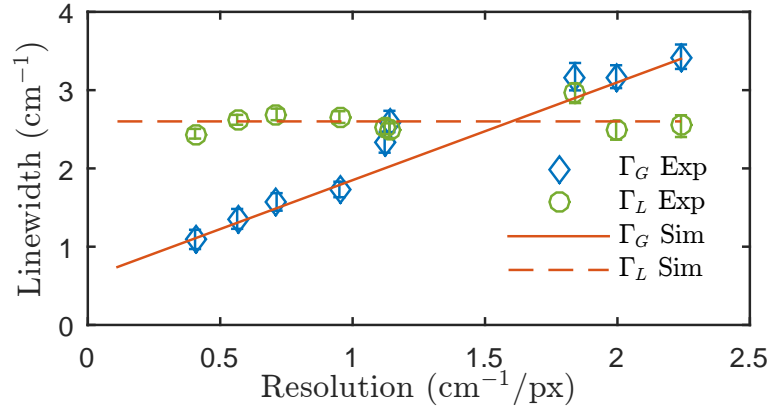


FIGURE 4.5: Gaussian and Lorentzian linewidth of simulated and experimental silicon Raman spectra versus resolution.

be equal to the resolution multiplied by the laser spot size on the CCD array, meaning the y-intercept would be equal to zero. However, the extrapolated intercept is non-zero implying that there is another source of Gaussian broadening that has not been considered even though pixel binning has been taken into account. The source of this broadening has not been determined but is likely caused by the finite spectral width of the laser line which was accounted for by adding a constant to the Gaussian linewidth⁵ as,

$$\Gamma_G = R\Gamma_S + \Gamma_0, \quad (4.1)$$

where R is the resolution in cm^{-1}/px , Γ_S is the laser spot size (Gaussian FWHM) in pixels and Γ_0 is a factor to account for the non-zero intercept. Equation 4.1 is plotted for $\Gamma_S = 2.8 \text{ px}$ and $\Gamma_0 = 0.59 \text{ cm}^{-1}$ along with experimental data to show the fit.

The last item that needed to be calibrated is the noise level. While the experimental noise of the spectra was quantified by taking the standard deviation of the signal between 600 and 750 cm^{-1} , additional noise is observed near the peak of the spectrum due to the probabilistic nature of the Raman process. To account for this, a noise proportional to the intensity of the signal was added to the spectrum

⁵This method is not strictly accurate since the laser line width would be convoluted with the Raman spectrum similar to how the Gaussian laser spot width is convoluted with the natural line of the Raman spectrum, but approximates the effect reasonably.

along with a baseline noise so that the simulated intensity was,

$$I_{Sim} = I_0 + N_{peak} * I_0 * randn + N_{base} * randn, \quad (4.2)$$

where I_0 is the simulated spectrum before noise, $randn$ is a function for calculating a random number with a normal distribution with standard deviation of one, N_{base} is the baseline noise level and N_{peak} is the peak noise level. The baseline noise level was carefully controlled during experimental data collection so was set to the same value for the simulation, 0.0025. However, N_{peak} is difficult to control and so was calculated after the fact and is approximately 0.02. This value was calculated by subtracting the fit curve from the experimental data to get the error at each pixel. The same was done for the simulated data while adjusting N_{peak} until the error data had a similar shape and magnitude for both the simulated and experimental data, see Fig. 4.6.

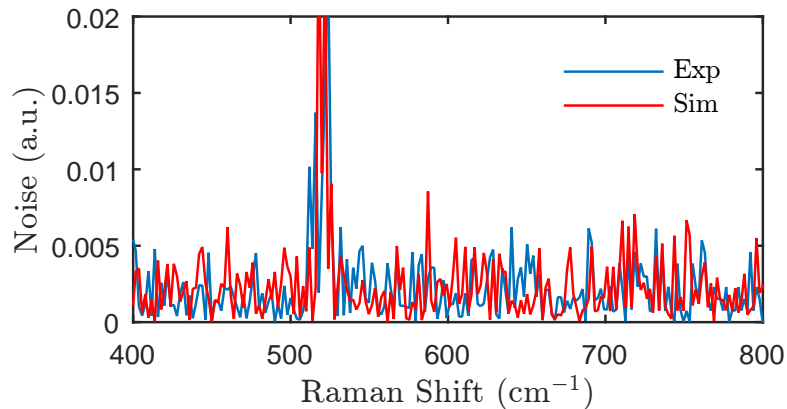


FIGURE 4.6: Simulated and experimental noise of the Si Raman spectrum.

The ultimate goal is to model the noise so that the simulation and experimental uncertainties match allowing us to predict the effects of resolution and RPI. Therefore, as a final test, the uncertainties of the experimental and simulation parameters were compared. Table 4.3 presents a few of the simulation and experimental fit parameters along with uncertainties for the case of 514 nm laser and 1800 g/mm grating. The simulation uncertainty results closely match the experimental results. However, our

TABLE 4.3: Uncertainties of fit experimental and simulated Si fit parameters for the 514 nm 1800 g/mm case.

Silicon	Γ_L	Γ_G	ν_0
Experiment	2.75 ± 0.119	2.98 ± 0.130	520.44 ± 0.0256
Simulation	2.58 ± 0.124	3.10 ± 0.094	520.42 ± 0.027

simulations slightly over predict the Lorentzian linewidth uncertainty while under predicting the Gaussian linewidth uncertainties. This is likely because our simulation also under predicts the Lorentzian component while over-predicting the Gaussian component.

Using these simulation input parameters, the effects of noise and resolution were simulated on the single peak Si linewidth uncertainty. In these simulations, 50 spectra were generated and fit at each resolution and noise level. The resolution ranged from 0 to 2.5 cm^{-1}/px and the noise ranged from 0 to 2 times the simulated noise, N_{base} and N_{peak} . Note, a noise fraction of one is equal to the experimental values. Uncertainty was calculated through a vector summation of the standard deviation of measured linewidth and fit uncertainty calculated from the fit Jacobian. The results are presented in a contour plot in Fig. 4.7.

As expected, as the noise and resolution worsen, the standard deviation of the linewidth increases. Additionally, the contours have a roughly circular shape indicating the resolution and noise fraction are roughly equally important for one peak linewidth measurements. Meaning doubling the noise has a similar effect as doubling the resolution. To investigate this more closely cross sections of the contour plot are plotted, i.e., FWHM uncertainty versus noise fraction (Fig. 4.7 (a)) and uncertainty versus resolution (Fig. 4.7 (b)). For the realistic experimental conditions of our system, i.e., $0.2 < \text{noise fraction} < 1.5$ and $0.4 < \text{resolution} < 1.5 \text{ cm}^{-1}/\text{px}$, the uncertainty is always a stronger function of resolution than noise. Therefore, when optimizing uncertainties one must choose to improve resolution before noise assuming the improving resolution does not lead to a disproportionate increase in noise. However, even in the disproportionate case, noise can be reduced

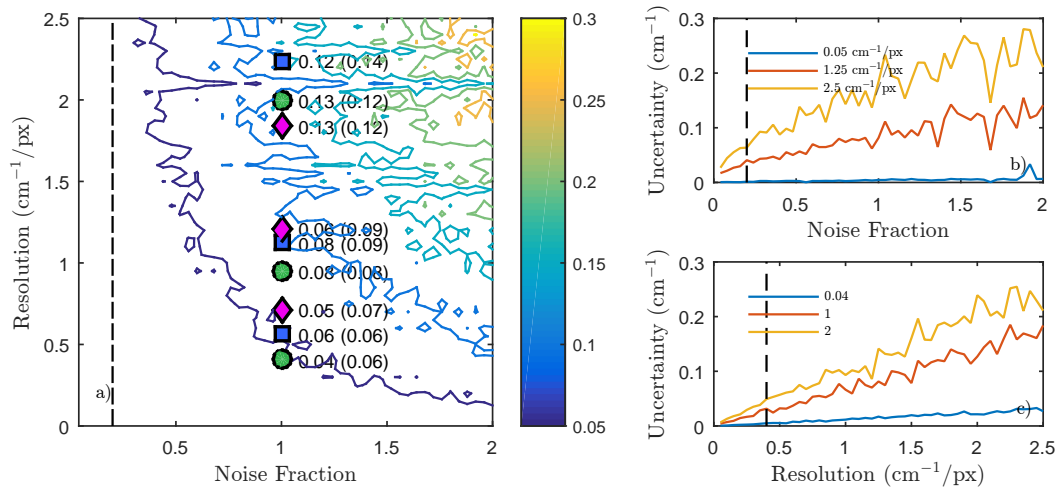


FIGURE 4.7: (a) Contour plot of the standard deviation of the Si Lorentzian linewidth vs resolution and noise level. Markers indicate position on the surface of experiment, 405 nm (diamonds), 488 nm (squares) and 514 nm (circles). The uncertainties of the experiment (simulation) are presented next to the markers. (b) Cross section of the contour plot in the noise fraction direction at various values of resolution. (c) Cross section of the contour plot in the resolution direction at various values of noise fraction. Dashed lines show the minimums of the noise and resolution for the Raman system at UVA.

(to a limit) by increasing the integration time of each collected spectrum, as shown in Fig. 4.3.

In conditions specific to the UVA system, markers in Fig. 4.7 (a), uncertainties vary by a factor of three with the ranges of resolution available. This underscores the importance of using high resolution conditions when measuring Raman linewidths. When attempting to measure the subtle changes to the linewidths, on the order of 0.1 cm^{-1} , caused by nanoscaled or small amounts of disorder it is imperative that the uncertainties be smaller than the changes. If resolution was not considered and the system at UVA was operated in its nominal state, the uncertainty would equal the changes being attempted to resolve in Chapter 6. However, by forcing the system into higher resolution condition it was possible to push the limits of measurements.

As a final general comment, these results are specific to a natural linewidth of 2.6 cm^{-1} . The magnitude of the uncertainty will increase and decrease with the natural

linewidth (not shown). However, the percent uncertainty decreases with increasing linewidth. This is because as the natural linewidth increases, it becomes greater proportionally to the instrument broadening, while a broader peak has more pixels mapping out the curve. It is therefore more important for minimizing uncertainties to minimize resolution for narrow linewidths (seen in highly crystalline materials) than for broader linewidths (seen in highly disordered systems).

4.4 Results

Using the simulation parameters developed for the one peak Si case, the effect of fitting two peaks simultaneously on the uncertainties of linewidths is investigated. Specifically, these investigations will focus on the effect of blurring the peaks together due to changes in resolution and the relative intensity of the peaks. The result of the simulation will then be compared to experimental results from Section 4.2. The results show that a single peak has a far better uncertainty than the case of two overlapping peaks. Therefore, selecting the laser wavelength to remove a second peak is of supreme importance. However, if this is not possible then ensuring that the intensity of the peak of interest (SiGe film peak) is on the same order or greater as the second peak (substrate) is key to ensuring low uncertainties.

4.4.1 Two Peak (SiGe)

For this simulation a range of RPIs consistent with experimental observations of the SiGe film samples is investigated along with the same resolution range studied previously. The parameters noise and instrument broadening are modeled the same way as in the previous one peak study. The peak of the SiGe alloys has an asymmetry that will no doubt effect the results of this study. However, for simplicity and to reduce the parameter space we model the SiGe peak as a symmetric peak. I believe that adjustments for a change in asymmetry will lead to similar trends as when asymmetry

is not included. Therefore, the signal from the two peak system is modeled as the sum of two Voigt functions, with natural widths of 4 cm^{-1} and 2.6 cm^{-1} for the film and substrate peaks, respectively. The difference in the widths is due to the alloy disorder broadening in the SiGe film. Because of the increased linewidth in the alloy film, the uncertainty in the measurement should decrease if the substrate signal is not observed, as previously discussed.

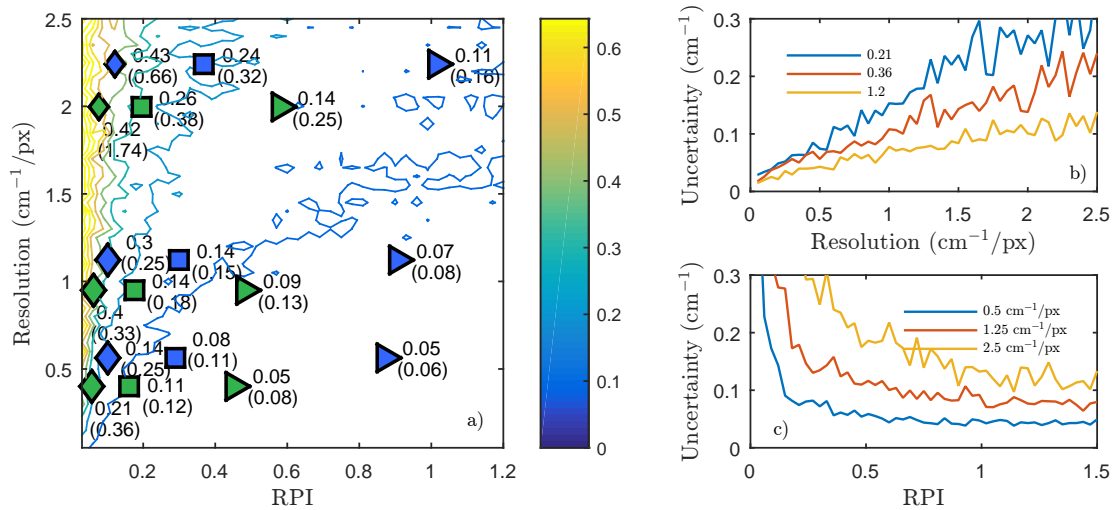


FIGURE 4.8: (a) Contour plot of the standard deviation of the SiGe Lorentzian linewidth vs resolution and RPI. Markers indicate position on the surface of experiment, 40 nm film (diamonds), 90 nm film (squares) and 210 nm (triangles). The color indicates the laser wavelength used, 514 nm (green), 488 nm (blue). The uncertainties of the experiment (simulation) are presented next to the markers in units of cm^{-1} . (b) Cross section of the contour plot in the resolution direction at various values of resolution. (c) Cross section of the contour plot in the RPI direction at various values of noise fraction.

Figure 4.8 (a) plots the experimental (markers) and simulated uncertainty results of the two peak uncertainty analysis as a function of both resolution and RPI. First note that the simulated parameters (parenthesis) closely match the experimental results, indicating the model accurately predicts the combined effects of resolution and RPI on linewidth measurements. The results for the 405 nm measurements are not shown on this plot because no substrate signal is generated when using the 405 nm laser and so sit at infinity on the RPI axis of Fig. 4.8 (a).

The experimental uncertainties however equal approximately 0.03 cm^{-1} , which half the lowest value on the contour plot.

The reason the 405 nm laser yields such low uncertainties compared to the 488 and 514 nm, is that unlike the single peak contour plot, Fig. 4.7, one of the experimental parameters dominates uncertainties. Just like in the single peak, the uncertainty is a linear function of resolution for all values of resolution, see Fig. 4.8 (b). However, at low RPI values, less than 0.5, the uncertainties exponentially increase. This is shown more clearly in the cross section of the contour in Fig. 4.8 (c). This means that when attempting to minimize uncertainties of linewidth measurements, the first priority is minimizing the substrate signal through the spatial resolution.

Since the 405 nm laser was able to improve the spatial resolution sufficiently high to prevent a substrate signal from being collected, it was selected for the SiGe linewidth measurements in Chapter 6. However, when the two peak signal cannot be forced to a one peak signal through wavelength selection, this procedure can help select the ideal conditions specific to a particular Raman system. The user will simply need to provide an estimated noise value and laser spot size, which can then be used in the described procedure to generate a surface plot similar to Fig. 4.8 (a). The results can then be used to tailor the experiment to minimize uncertainties through selection/purchase of grating, grating order, and laser wavelength.

Note that the magnitudes of the uncertainties are specific to the experimental conditions of the SiGe alloy thin films being studied. Specifically, the results will change as the linewidths and separation between peaks changes. As the peaks are separated further, they overlap less. This leads to fit parameters that are weakly coupled in the Jacobian of the fits which in turn results in lesser uncertainties (not shown). Therefore, these exact results are specific to this test. However, the trends will be consistent.

4.4.2 Pixelation Error

While RPI plays the larger role in uncertainties, resolution plays a major role in the error of the measurement. If we take enough data with a low RPI and high resolution, it is possible to minimize the uncertainty through confidence intervals. Alternatively, the fit function can be weighted to force the small film signal to be prioritized. However, if the average value is biased then the confidence intervals will not bound the real linewidth value. Low resolution can cause significant errors/biases to the measured linewidth of a two peak signal due to blurring of the peaks. As these peaks blur together, the saddle point where the two peaks overlap becomes pixelated causing the peaks to look broader, see Fig. 4.2. Alternatively, if a low resolution spectrum does not have a pixel mapping the top of the peak, the fit function will artificially increase the fit height above the maximum pixel signal leading to a narrower linewidth. For these reasons, it is important to ensure that maximizing the RPI does not lead to a significant worsening of the resolution.

When modeling the effects of resolution, the simulated Raman signal has two linewidth components: natural and instrument. Often the instrument broadening value is determined by measuring the linewidth of peaks in the neon lamp spectrum. Since the natural linewidth of the peaks is infinitesimal, the width of the peak is then equal to the width of the instrument broadening. However, because the line is so narrow only 2-4 pixels map out the curve. So, fitting functions try to fit the peak by over estimating the peak height causing an artificially narrow fit of the linewidth. At this point, it became clear that accounting for pixelation was required to measure the linewidth of the very narrow peak. However, this is also necessary when trying to measure small changes in the curvature of a spectrum compared to the resolution. In other words, high curvature points in a spectrum (i.e., tops of peak and saddle points between peaks) cannot be measured in relatively low resolution spectra unless the pixelation is accounted for.

The situations described above are illustrated in Fig. 4.9. Figure 4.9 (a) plots

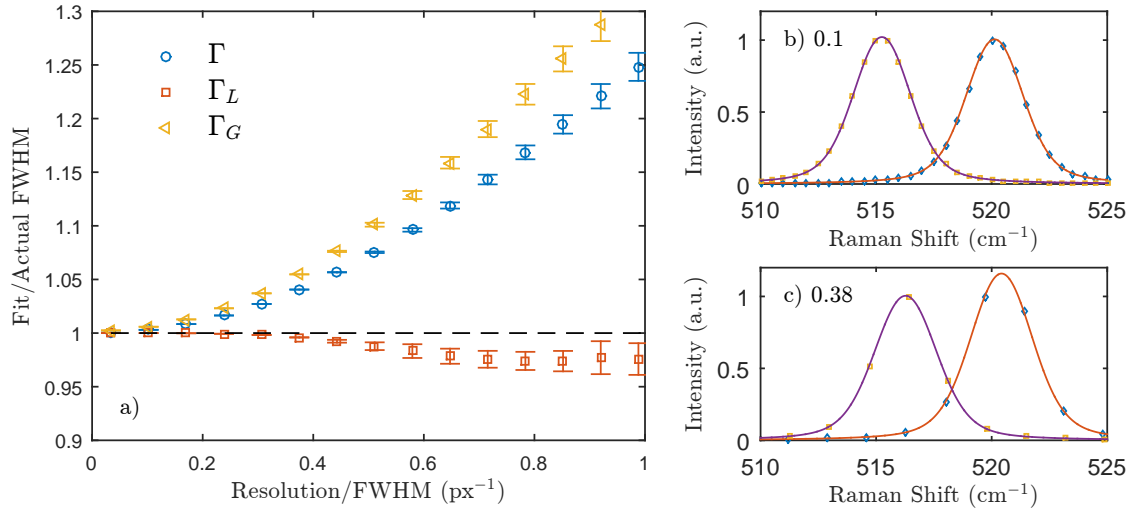


FIGURE 4.9: (a) Normalized fit FWHM versus normalized resolution showing how resolution biases the fit of the Lorentzian linewidth. The fit FWHM and resolution were normalized by the actual FWHM of the simulation input peak. (b) Two spectra (markers) at high resolution with pixels located at different point on the peaks and their corresponding fit (lines) (c) Two spectra (markers) with pixels located at different locations on the peak at low resolution and their corresponding fits (lines).

the normalized fit results as a function of normalized resolution. The Lorentzian, Γ_L , Gaussian, Γ_G , and total, Γ , FWHM calculated by fits are normalized by their real value before pixelation. The resolution is normalized by the width of the total FWHM of the peak. They were normalized this way so that these results can be applied to any Raman linewidth studies. This plot shows that as the resolution worsens, the broadening caused by pixelation is absorbed by the Gaussian FWHM. At low resolutions, the natural (Lorentzian) linewidth closely matches its actual value. However, when the pixel broadening reaches about 0.4, the fit of the natural linewidth is biased away from its real value while at the same time the uncertainty of the measurement increases. The reason for this is that strong pixelation is not Gaussian broadening. So, the Gaussian component of the linewidth cannot fully capture its effect.

The other reason for the error in the Lorentzian is that the fit function fits the Raman spectra differently depending on where the pixels lie on the curve. Figure 4.9

(b) shows two spectra at high resolution (0.1 on the x-axis of plot (a)) with pixels located at different points on the peak. The fits to the peaks are nearly identical because there are sufficient pixels mapping out the curve and the pixel broadening effect is weak. Figure 4.9 (c) on the other hand has a poor resolution (0.38 on the x-axis of plot (a)). The fits here are visibly different when a pixel lies at the center of the peak versus when they flank the center. The fit function tries to minimize the error at these the highest two pixels which artificially increases the peak intensity leading to a narrowing of the linewidth. Note that the linewidth of Si when using the the 405 nm laser and the 1800 g/mm (-2) grating is 3.25 cm^{-1} at a resolution of 0.7 (0.22 on the x-axis of (a)). Therefore, the Si linewidth is on the edge of being effected by the pixelation, but no biases on the natural linewidth should be observed. However, under poor resolution conditions, it is possible for biases to effect linewidth measurements.

This was observed in this study before higher order gratings were employed. Since the resolution of a particular grating is wavelength dependent, switching from the 514 nm laser to the 405 nm to maximize the RPI lead to a 3 fold increase in the resolution, see Table 4.1. However, it is possible to partially account for the pixelation, by modifying the fit function. By forcing the Voigt function to pixelate before the fit, the Gaussian component of the function does not have to absorb the pixel broadening. This is especially helpful when trying to separate two overlapping peaks.

The most difficult part of separating two peaks is accurately fitting the saddle point between the peaks. Figure 4.9 (a) showed that a resolution ≤ 0.4 times the FWHM of a feature is needed accurately fit that feature. The saddle point in our SiGe spectra is very small compared to the resolution of our system. Therefore fitting the two peaks will hinge on having high resolution or accounting for the pixel broadening in the saddle point. Any Raman function, e.g., Lorentzian, Voigt, Fano, can be modified to account for pixelation. This is done by calculating the fit function for ~ 100 times the density of spectral points and then summing those

point in ranges centered on pixel wavelengths. The increased numerical integration is computationally expensive leading to long fit times, but it significantly improves fitting.

4.5 Conclusions

When attempting to perform linewidth measurements of nanoscaled materials, deconvolving the signal of interest from background signals is paramount for minimizing uncertainties. In submicron SiGe thin films grown on Si substrates, this means separating the overlapping SiGe and Si peaks. Accomplishing this hinges on properly setting up the experiment by optimizing spectral and spatial resolution to adjust the relative intensities of the peaks and the pixelation of the signal. Uncertainties are most effectively minimized if the substrate signal can be completely excluded through selection of laser wavelength, unless this results in a disproportionate worsening of the spectral resolution. Therefore, maximizing spatial resolution is the first priority for minimizing uncertainties. For this reason, the 405 nm laser with the 1800 g/mm (-2) grating was selected for linewidth measurements in Chapter 6. The small penetration depth of the 405 nm laser, 60 nm, prevents a substrate signal from being generated, while using the 1800 g/mm grating in the -2 order improves resolution to 0.7 cm^{-1} . When it is not possible to completely remove the substrate signal, minimizing spectral resolution has a stronger effect on minimizing uncertainties and biases than noise. Therefore the second priority should be to select the best resolution possible. Noise can then be minimized as the third priority by increasing integration time of the experiment.

Chapter 5

Laser Heating of SiGe Alloys

5.1 Motivation

Nanoscaling materials causes Raman peaks to asymmetrically broaden. This asymmetry is most commonly accepted to be caused by physical confinement of the modes[100–102, 106, 107, 112, 154]. Phonon confinement relaxes selection rules, which in turn leads to a peak asymmetry. Several studies have used the asymmetry of the Raman peak from nanowires[111, 155], nanograins[107, 108, 156], nanoparticles[104, 157] and superlattices[158] as a metric for the limiting dimension of the material. However, the exact physical mechanism for this asymmetry is not explained in the literature beyond the phenomenological PCM model. Several studies have questioned the phonon confinement model, suggesting that the asymmetry could instead originate from laser heating[159–164], or Fano resonance[165–168].

One study showed that if the laser power was reduced to an absolute minimum, the asymmetry in Si nanowires, Raman peak, vanished[166]. They then went on to hypothesize that the asymmetry in Si nano-wires was actually due to Fano resonance. This idea was supported by a recent study that had studied boron doped Si Raman spectra as a function of laser power and observed a similar peak shift and asymmetric

broadening[167]. This was further supported by a study which investigated the effects of laser power density and Si nanostructure size, and found a similar peak down shift and asymmetric broadening[168].

Doping silicon causes the continuum of electron energy levels to resonantly interact with the phonon line to create an asymmetry via the Fano interaction[149]. The type of dopant can be determined in the Raman spectra by the side the asymmetry of the peak appears. The asymmetry will be on the low energy side for n-type dopants and on the high energy side for p-type. The absolute magnitude of the Fano interaction depends on the population of free carriers and so increases with photo-excitation. This led to the hypothesis that the observed laser power and asymmetry trends were due to Fano interactions.

Other studies challenged the assertion that the asymmetry is due to Fano resonance and contend that it is instead caused by inhomogeneous laser heating[159–164]. These studies hypothesize that due to the finite spot size of the laser and finite penetration depth, the probe laser creates large temperature gradients. Raman signals are then generated from a range of temperatures leading to the observed peak asymmetry. For example Adu *et al.* showed that using the PCM modified for temperature distributions, they could recreate the asymmetry caused by laser heating[160, 161]. They further tested this hypothesis by changing whether the nanowires were in thermal contact with a substrate or not. The asymmetry of the Raman peak for nanowires in thermal contact with the substrate reduced when compared to suspended wires suggesting laser heating.

Silicon nanocrystals were also investigated[163, 164], but instead of a change in asymmetry, the main Raman peak split into two peaks that further separated as the laser power density increased. This was attributed to heating differences in the “bulk” of the nanocrystal and in the oxide surface layer. This was further explained through a two temperature model for surface and “bulk” modes[164].

During laser heating tests from the previous chapter, a similar asymmetry and

even peak splitting with laser power density was observed in the Raman spectra of SiGe alloy thin films. Since the asymmetry will be used as a metric for the confinement of optical modes in the following chapter, it is imperative that the origin of the asymmetry is understood. The purpose of this chapter is to shed light on the cause of the observed asymmetry versus laser power trends. The first section will experimentally investigate this effect and attempt to rule out some of the hypotheses previously presented. A custom steady state FEA code will then be used to model the effects of laser heating on Raman spectra to see if it is possible to create a similar change in peak shape with laser power. In the end, it is found that Fano resonance is not the cause of the asymmetry, and inhomogeneous laser heating is the most likely candidate.

5.2 Experimental Investigations

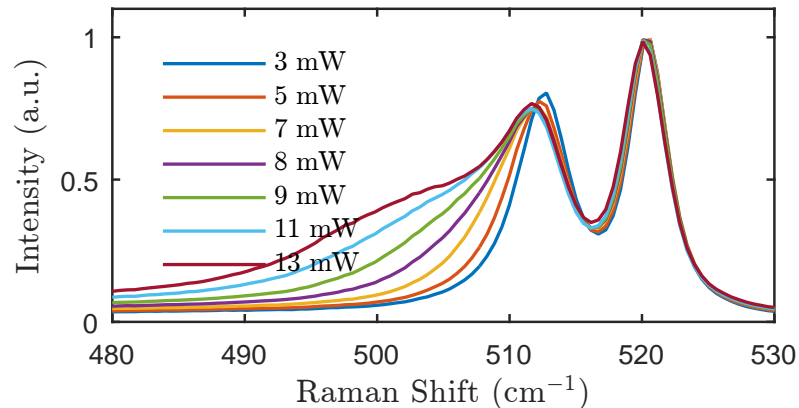


FIGURE 5.1: Raman spectra of Sample 7, 25% Ge 210 nm thick, using 488 nm laser at various laser powers.

Figure 5.1 plots the experimental Raman spectrum of Sample 7 (25% Ge, 210 nm thick SiGe film) at various 488 nm laser powers. The peak around 512 cm^{-1} is from the SiGe film while the peak at 520 cm^{-1} is from Si substrate. As the laser power increases, the peak asymmetrically broadens. At the highest laser powers, the peak even seems to split. Similar observations have been observed previously in Si

nanowires and nanoparticles attributed to either: (1) Fano resonance, (2) surface modes, or (3) inhomogeneous heating. The goal of this experimental section is to determine which of these hypothesis may be the cause of this asymmetry versus power trend.

5.2.1 Fano Resonance

In response to the claim that Fano resonance was the cause of the asymmetry, Piscanec *et al.* reinvestigated this effect on Si nanowire mats[159]. They were able to recreate the change in asymmetry with laser power, but based on two points they rejected the assertion that it was due to Fano resonance. First, if Fano resonance was the cause, it would be caused by photo excited electrons and holes. Since the resonance in Si is more strongly coupled with holes, the asymmetry should be on the high wavenumber side of the Raman peak. Instead, the asymmetry occurs on the low wavenumber side. Secondly, Fano resonance is excitation energy dependent, i.e. laser wavelength dependent.

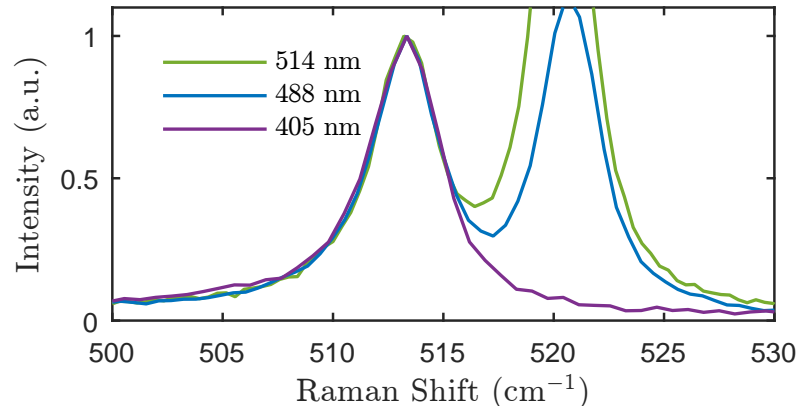


FIGURE 5.2: Raman spectra of Sample 7, 25% Ge 210 nm thick, using 405, 488 and 514 nm laser wavelengths at very low laser power.

When Cerdeira *et al.* investigated the effect of heavy doping on the Raman spectra they found that the degree of Fano resonance followed the probing laser wavelength[149]. Therefore, if the observed asymmetry is due to Fano resonance,

then a higher wavelength light source will increase the Fano effect. However, due to different penetration depths of each laser wavelength and thus power densities this effect must be tested only at very low laser powers where heating is negligible and can be ruled out. Raman spectra at very low powers, $< 80 \mu\text{W}$, taken using 405, 488 and 514 nm lasers are plotted in Fig. 5.2. Note that the absorbed power will depend on the wavelength. However, these powers should be sufficiently low enough to prevent any heating regardless of the absorption fraction. As we can see, there is no strong difference in asymmetry between the three wavelengths at low power, indicating that the asymmetry is not due to Fano type resonance. Additionally, the asymmetry is on the low wavenumber side as seen by Piskanec *et al.*[159] again supporting the claim that the asymmetry is not caused by Fano resonance. Furthermore, Fano resonance could not explain the existence of peak splitting in the spectrum as shown in Fig. 5.1. For these reasons, Fano resonance is disregarded as a possible inducement of observed asymmetry.

5.2.2 Laser Heating

Attention is thus turned to the influence of laser-induced heating. Heating could induce two different changes leading to asymmetry. First, localized-surface-modes may be preferentially heated. Second, the inhomogeneity of the heating could also induce asymmetric broadening. To assess the relative likelihood of each effect, the alloy composition and film thickness were adjusted. Film thickness changes the deposited power density, but also changes the film resistance to mimic the effect of substrate thermal contact and isolation in the Si nanowires previously discussed[160]. Changing the alloy composition allows for a change in the amount of disorder in the sample, thereby influencing the ratio of “bulk” to disordered modes, which can in turn be monitored by the magnitude of peak splitting.

Inhomogeneous Heating

The main point of evidence that Adu *et al.* used to support that inhomogeneous laser heating was the cause of the observed asymmetry changes with laser power, was the reduction in asymmetry when their Si nanowires were in thermal contact with the substrate versus suspended. When the nanowires were in contact with the substrate, the substrate acted as a heat sink abating the laser deposited thermal energy and reducing thermal gradients and in turn peak asymmetry. When the nanowires were suspended the heat was trapped in the wires due to their low thermal conductivity and poor thermal contact with other wires leading to large temperature gradients. Since the Raman spectrum is temperature dependent, each infinitesimal location on and in the wire will yield a Raman spectrum based on its temperature. Each of these sub-spectra will then sum to create an asymmetric peak.

Following the example of Adu *et al.*[160], the effects of laser power on the asymmetry in SiGe thin films with different thermal resistances between the location of laser deposited thermal energy and the heat sink (substrate) were studied. Figure 5.3 plots the spectra for (a) 40 nm and (b) 210 nm Si₇₅Ge₂₅ films at various 488 nm laser powers. The temperature rise can then be approximated using the peak positions from fits to the spectra as metrics for the temperature¹. The measured temperature rise of the film and substrate is plotted for the 40 nm and 210 nm films in Figs. 5.3 (c) and (d), respectively.

As the laser power increases, the measured temperature rise of the film and substrate also increase as expected. However, in the 40 nm film the substrate temperature rises faster than film and vice versa for the 210 nm film. This is because, as the film thickness increases the thermal resistance of the film also increases. Therefore energy deposited near the top of the film will have more resistance before being wicked away by the substrate leading to a higher

¹The peak positions are linearly related to temperature where the proportionality constant was assumed to be equal to that of Si, $-0.022 \text{ cm}^{-1}/\text{K}$ [130].

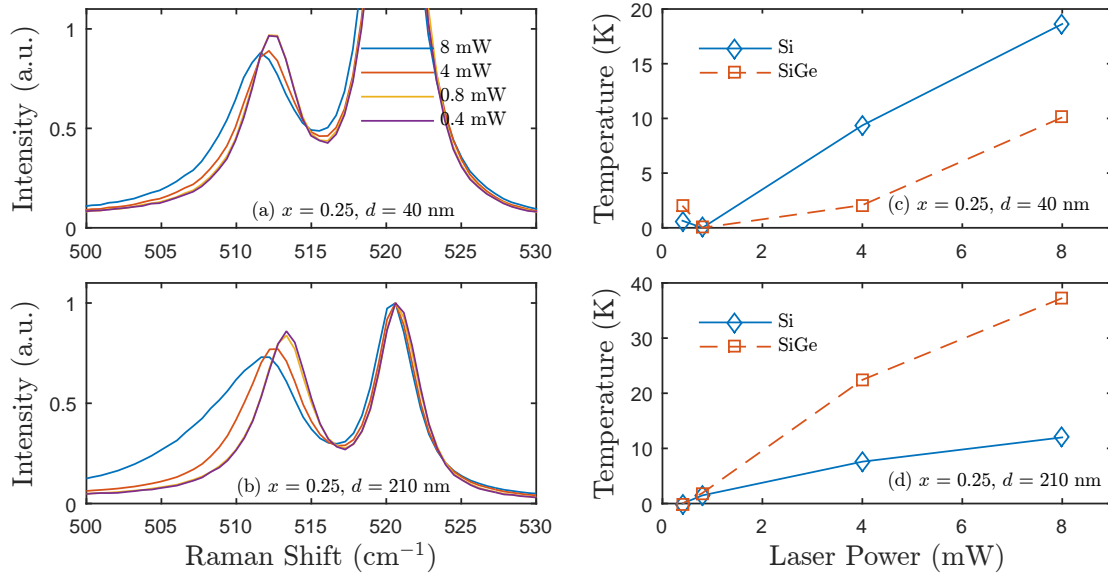


FIGURE 5.3: Raman spectra of (a) 40 nm and (b) 210 nm $\text{Si}_{75}\text{Ge}_{25}$ films at various laser powers. Using the peak position as a temperature metric, the temperature rise of the Si substrate and alloy film are plotted versus laser power for the (c) 40 nm and (d) 210 nm films.

temperature². However, the amount of thermal energy deposited also changes because the penetration depth of the 488 nm laser is larger than the film thickness, ~ 300 nm (see Table 3.1). This causes the Si substrate to heat more in the 40 nm film than 210 nm film. Using the Beer-Lambert Law (Eq. 3.17), I determined that the energy deposited in the 40 nm film is approximately 25% of that deposited in the 210 nm film. I then compared the 8 mW condition from the 40 nm film to the 2 mW condition of the 210 nm film to see if the laser heating is different. Extrapolating the data from for the 210 nm film, we see that the temperature rises and asymmetries of both films are nearly equal for similar power densities. Since the peak position is a metric for the average sample temperature, this result suggests that average temperature is not the cause of asymmetry. However, it is inconclusive with regard to the inhomogeneous heating hypothesis. A more conclusive study could be performed if a higher laser power was achievable or if the penetration depth was smaller.

²The thermal conductivity of Si is $\sim 150 \text{ W m}^{-1} \text{ K}^{-1}$ [169] and $\sim 2 \text{ W m}^{-1} \text{ K}^{-1}$ for SiGe[48].

Laser heating in these films was reinvestigated using a laser with a smaller penetration depth, 405 nm laser, but the 405 nm laser did not affect the peak asymmetry even at the highest laser powers (not shown³). This may be because the 405 nm laser power only provides 2 mW to the sample. However, because the penetration depth is less than a quarter of the 488 nm laser, the power densities are approximately equal. Therefore, we would have expected to see an asymmetry change at the highest laser power. Alternatively, it is possible that because the Raman spectrum of Si₇₅Ge₂₅ is resonant at 405 nm (see Fig. 3.3)[5], the bulk-like modes have a much stronger signal than the surface or disorder modes and so are not observable.

This can be further investigated once the new 405 nm laser is purchased. The new 405 nm laser will be able to deliver 100 mW to the samples. This will allow the for higher power densities to be tested, potentially causing a change in the Raman peak asymmetry. If the asymmetry is affected at high 405 nm laser power, then it would provide evidence that inhomogeneous heating is the cause of the asymmetry. However, if no change is seen then it supports the hypothesis of a dual mode peak.

Dual Mode Peak

Since the above tests are inconclusive, focus is shifted towards testing the hypothesis of the Raman peak being composed of both disorder and bulk-like modes. It is possible that alloy disorder breaks the symmetry of the crystal leading to multiple Raman active modes partially overlapping, which in turn creates the asymmetry in the peak. Disorder causes a break down of the zone center selection rules while also causes Brillouin zone folding leading to more modes at the zone center. Since more modes exist at the zone center more modes are available for Raman scattering. If the spectra from these modes overlap with the bulk Si-like

³Figure 5.7 shows the SiGe peak at high laser powers using both the 405 nm and 488 nm laser. Note that the asymmetry is much smaller in the 405 nm case than the 488 nm case. This level of asymmetry was observed at all 405 nm laser powers.

mode signal, it is possible that the asymmetry originates from these disorder activated modes. An alternative possibility is that the second peak in the spectrum is from surface modes either on the surface of the SiGe film or at the interface between the film and Si substrate as hypothesized Ref. [163].

If disorder modes are the cause of the peak asymmetry, then one would expect that the effect of laser heating on the asymmetry and peak splitting should be higher for samples with more disorder or a higher Ge fraction. Figure 5.4 plots the spectra for four samples with (a) 50%, (b) 25%, (c) 20% and (d) 15% Ge at various laser powers. In Figs. 5.4 c) and d) the laser power increases the main peak asymmetry. However, it isn't obvious that this is a second peak until the Ge content reaches 25% as in Fig. 5.4 (b). At 13 mW we clearly see that a peak is beginning to separate from the main Si-Si peak and that this is not simply an asymmetry. This is also evident at 50% Ge, which suggests that the peak may be composed of two different types of modes. However, it must be noted that the sample thermal conductivity and laser penetration depth of the laser is decreasing with increase Ge fraction, which may also be the reason for the change in asymmetry.

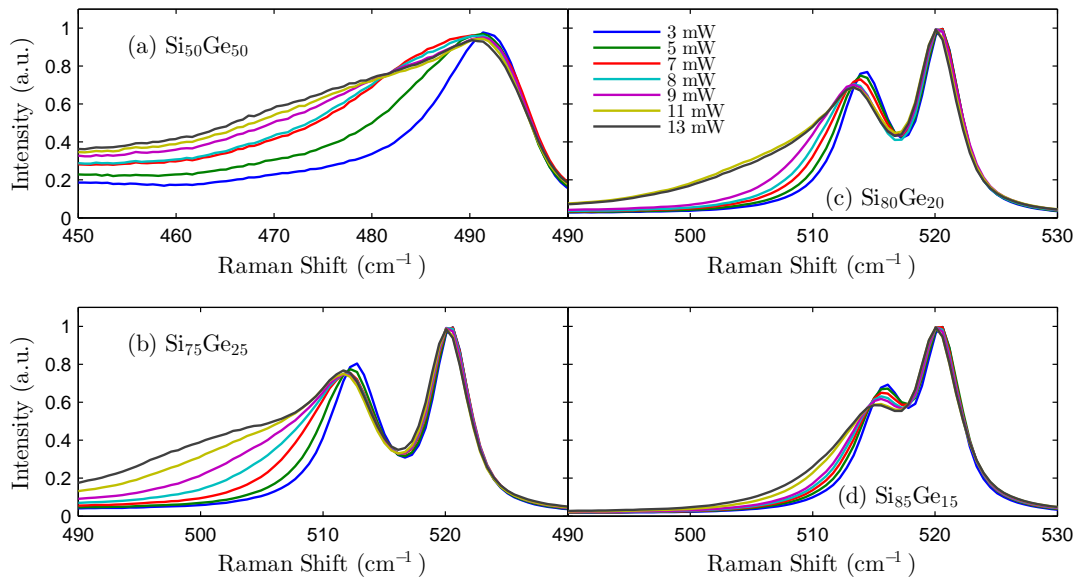


FIGURE 5.4: Raman spectra of the Si-Si peak in SiGe alloys with various Ge content and at various laser power.

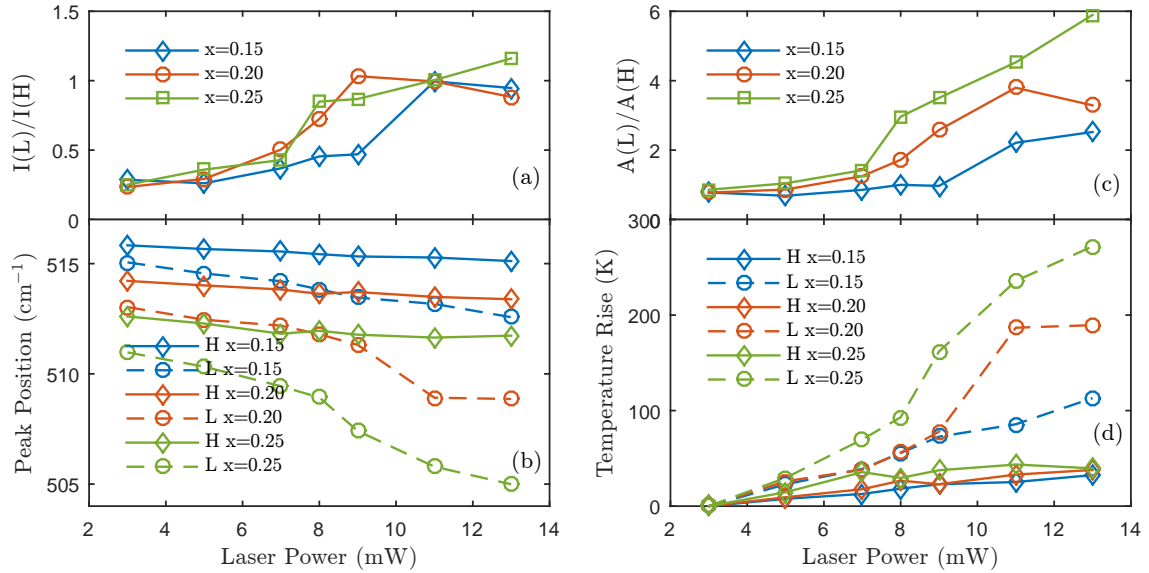


FIGURE 5.5: Fit results of the Si-Si peak.

Recently, a study found that laser heating of Si nanocrystals caused a splitting of the single Si TO peak into a double peak supporting the above findings[163, 164]. Using the Stokes/anti-Stokes intensity ratio and peak position the temperature of each peak was measured. At high laser power, the high wavenumber peak (H-peak) indicated a 300 K temperature rise while the low wavenumber peak (L-peak) indicated a 1200 K temperature rise. They attributed these two peaks to surface modes (L-peak) and bulk-like modes (H-peak). The temperature difference between the modes was hypothesized to be caused by the oxide layer in between the crystallites.

Following a similar procedure as Ref. [163], the shifts and associated temperature of the Si substrate, alloy bulk-like mode (H-peak) and disorder mode (L-peak) were investigated by fitting to three peak function for each of the above samples at various laser powers. The 50% Ge sample was not fit due to the complexity of its spectrum. The results are plotted in Fig. 5.5. Figures 5.5 a) and c) plot the relative intensity and area of the L-peak to H-peak, respectively. The relative intensity and area show how the population of each mode is changing relative to one another, since the area of the Raman peak is related to the Bose-Einstein distribution. As the laser power

increases, the relative intensity of the disorder mode to the bulk-like mode increases, suggesting that the disorder mode is preferentially populated by laser heating. The trend of the ratio versus laser power is roughly constant for each composition. The reason the area ratios are not constant is because the widths of the disorder and bulk peaks are different for each composition.

Figure 5.5 (b) plots the change in peak position (d) and corresponding temperature rise of the two peaks versus laser power for the three compositions. Note that both the L-peak and H-peak positions have the same temperature dependence under uniform heating, i.e., heating in a temperature stage (not shown). These results show that the two peaks shift at very different rates with laser power. The H-peak shift versus laser power is nearly identically for all samples and show maximum temperature rise of 40 K at 13 mW. The L-peak on the other hand shows very different trends for each composition, with maximum temperature rises of 100, 200 and nearly 300 K for 15, 20 and 25 % Ge concentration, respectively. These results are very similar to those found by Faraci in nanocrystals[163], suggesting that two peaks are observed.

If we assume temperature measurements using peak positions would match Stoke/anti-Stokes measurements, as they do in Faraci[163], then the confined modes in our spectra actually feel a different temperature than the bulk modes. In other words, disorder modes are preferentially populated by the localized laser heating. A similar effect is seen when heating polar semiconductors with an electrical current. The optical modes are preferentially populated due to the efficiency of electrons to scatter with them[170, 171].

The dual mode peak hypothesis can also be tested by changing the polarization of the probing laser. The Si-Si Raman mode of the SiGe alloy, located at $\sim 515 \text{ cm}^{-1}$, is only visible for select polarizations of the probe light[120, 172]. This means that the intensity of this mode can be controlled via the relative crystal orientation to the laser polarization, i.e., by rotating the sample. If disorder modes are being created by the alloy disorder and appearing in the Raman spectrum, then they will likely not

have the same symmetry as the bulk-like Si mode. This is seen in disordered modes in other materials systems such as the disorder induced D-peak in carbon allotropes which has a different symmetry and thus polarization dependence than the bulk G-peak[98, 173]. Rotating the sample should then result in a change in the magnitude of the asymmetry. However, if asymmetry is part of the Si-Si mode then the asymmetry should remain constant with rotation angle. Therefore, the asymmetry is monitored as a function of sample rotation angle to determine if its origin stems from the disorder. However, it must be noted that we do not know the symmetry of the disordered modes so this is only conclusive if a change in the asymmetry is observed since it shows that there are indeed two different types of modes. A negative result yields little information since the disordered modes may have the same symmetry as the bulk-like modes.

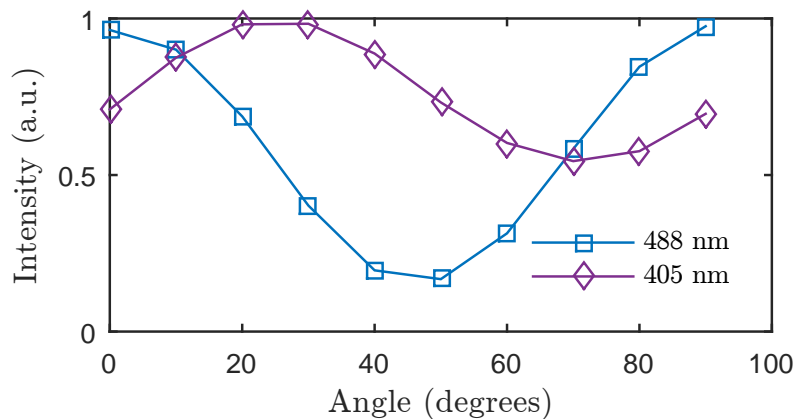


FIGURE 5.6: Peak intensity of the Si (100) Raman spectrum as a function of polarization relative to the (100) crystal direction.

Figure 5.6 plots the normalized peak intensity of the Si(100) Raman spectrum as a function of sample rotation angle. As the sample rotates the signal intensity oscillates sinusoidally due to the fraction of the light polarization vector parallel with the (100) crystal direction changing[172]. Note that the intensity does not go fully to zero. This is due to small imperfections in the lattice as well as not having a perfectly polarized laser. The difference in phase of the 488 and 405 nm sine curves is due to

the output polarization of the 405 nm laser being off vertical.

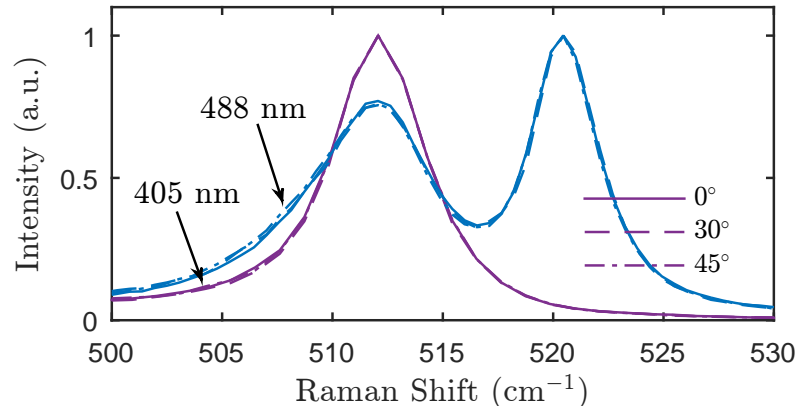


FIGURE 5.7: Raman spectra of a 210 nm $\text{Si}_{75}\text{Ge}_{25}$ thin film at various polarizations relative to the crystal orientation for the 405 nm and 488 nm laser at high laser power, 2 and 8 mW, respectively.

Figure 5.7 plots the SiGe (25% Ge and 210 nm thick) spectrum at three rotation angles for both the 405 nm laser (2 mW) and the 488 nm laser (8 mW). There are no appreciable differences in the shape of the spectra, i.e., asymmetry, with different angle of polarization. This may suggest that the peak is not composed of multiple peaks from the bulk-like and disorder induced modes. However, this is not concrete evidence, since disorder modes may have similar symmetries to the bulk-like modes and may not be separable by changes in polarization.

The experimental investigations showed that Fano resonance is not the cause of the asymmetry seen in our Raman spectra of SiGe alloys and is likely due to laser heating. However, the investigations into how exactly laser heating is creating the peak asymmetry were inconclusive. Some evidence showed that two peaks, one from disorder induced modes and another for bulk-like modes, overlap in the spectrum. The disordered mode is preferentially heated leading to a splitting of the peak in the spectrum. However, other data suggests that the laser inhomogeneously heats the sample creating an asymmetric spectrum composed of sub-spectra from a range of temperatures. Due to the inconclusive results, the effect of laser heating is modeled using an equilibrium finite elemental model as a final test.

5.3 Modeling Laser Heating

In order to test whether this asymmetry with laser power and emergence of the second peak could be solely due to laser heating, 488 nm laser heating of SiGe film with Ge concentrations ranging from $x = 0.15$ to 0.25 were modeled using a steady state FEA model.

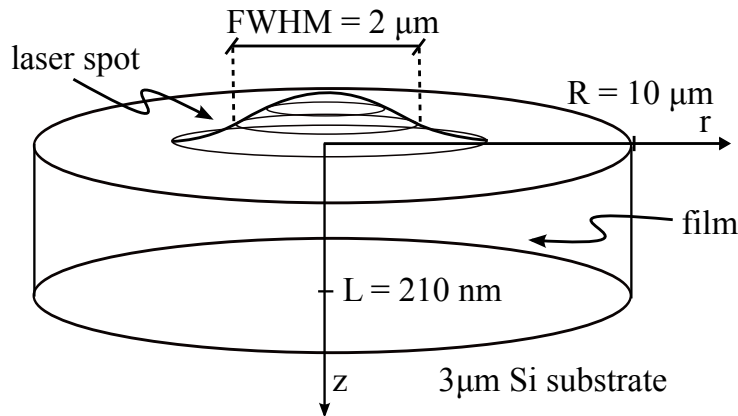


FIGURE 5.8: FEA model system for laser heating thin film (*not* drawn to scale). A cylinder with radius $10 \mu\text{m}$ and thickness 210 nm was irradiated with a $2 \mu\text{m}$ laser beam. Due to the radial symmetry, the system was constructed in 2-dimensions, r and z .

5.3.1 Model System

Since the Gaussian laser spot has radial symmetry, a 2-dimensional code was written in cylindrical coordinates. The system was modeled as a $10 \mu\text{m}$ radius by 210 nm thick cylinder on a $3 \mu\text{m}$ Si substrate as shown in Fig. 5.8. To model the heat flow through the cylinder, the system was discretized into a cylindrical shells as shown in Fig. 5.9. In steady state, the flux out of the shell must then equal the heat generation in the cell due to the laser,

$$Q_{Laser}(r, z) = Q_T(r, z + \frac{\Delta z}{2}) + Q_B(r, z - \frac{\Delta z}{2}) + Q_L(r - \frac{\Delta r}{2}, z) + Q_R(r + \frac{\Delta r}{2}, z), \quad (5.1)$$

where Q_T , Q_B , Q_L and Q_R are the fluxes out of the top, bottom, left and right of the element, respectively, Q_{Laser} is the heat generated by the laser and Δr and Δz are the element's radial and z size. In general, the thermal flux through a finite surface is proportional to the thermal conductivity, k , area of the surface, A_S and temperature gradient across the surface, $\vec{\nabla}T$. However, in our case the elements are chosen so that the surfaces point in a single orthogonal direction so that the gradient becomes one dimensional and since the element are finite in size the derivative becomes a ratio of finite differences,

$$Q = -kA_{(r,z)}(r) \frac{\Delta T}{\Delta(r, z)}, \quad (5.2)$$

where the areas in both the z and r -direction are a function of r ,

$$A_z(r) = \pi\left(\left(r + \frac{\Delta r}{2}\right)^2 - \left(r - \frac{\Delta r}{2}\right)^2\right) = 2\pi r \Delta r, \quad (5.3)$$

$$A_r(r) = 2\pi r \Delta z. \quad (5.4)$$

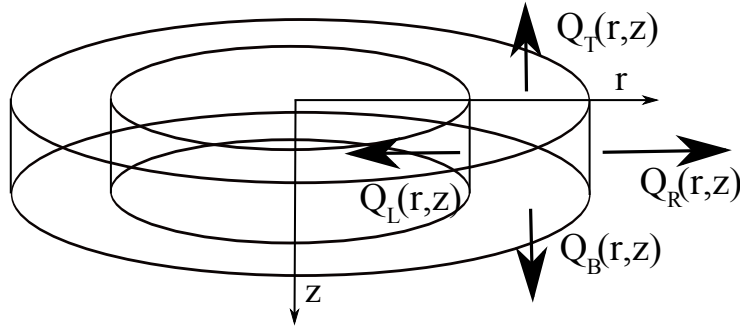


FIGURE 5.9: (solid) Raman spectra of the Si-Si peak in SiGe alloys at various temperatures using the 405 nm laser. (dashed) The fit of the peak using a Fano line shape is also shown at each temperature.

The top and bottom boundary condition were free convective heat transfer with convection coefficient assumed to be $h = 50 \text{ W/m}^2/\text{K}$. The center of the cylinder had an adiabatic condition so only one half of the laser spot needed to be simulated, which reduced the computational expense. The outer boundary of the cylinder was

fixed to room temperature, 300 K. The interface between the film and substrate was modeled assuming a boundary conductance of $200 \text{ MWm}^{-2}\text{K}^{-1}$.

5.3.2 Laser Heating

The laser heating was modeled with a Gaussian spot centered at a radius of zero with FWHM of $2 \mu\text{m}$. Since the laser is Gaussian in both the x and y-directions, a Gaussian in the r-direction was constructed ensuring that the area under the curve was equal to the laser power. Each point of that Gaussian was then multiplied by the peak intensity of another Gaussian whose area under the curve equaled one, $2\ln(2)/\Gamma_{spot}\sqrt{2\pi}$, where Γ_{spot} is the laser spot FWHM. This step ensured that the volume under the 2-dimensional Gaussian equaled the power of the laser. That intensity was then multiplied by $A_z(r)$ to get the laser power incident at each radial surface. Due to the finite penetration depth of the 488 nm laser on Si, this power was then distributed into the sample using the Beer-Lambert law (Eq. 3.17) of 488 nm light in $\text{Si}_{75}\text{Ge}_{25}$ is 260 nm. So, the incident light was then scaled by the light absorbed in each element by finding the difference in the light intensity at the top surface and bottom surface of each element,

$$I_{absorbed} = I_{BL}(z - \frac{\Delta z}{2}) - I_{BL}(z + \frac{\Delta z}{2}). \quad (5.5)$$

The penetration depth was not adjusted for the different compositionse during simulations.

5.3.3 Solution

The temperature map was then calculated by solving the system of equations,

$$\tilde{A}\vec{T} = \vec{b}. \quad (5.6)$$

This meant generating a matrices, \tilde{A} and vector \vec{b} , where \vec{T} is the temperature vector and \vec{b} is a vector that contains the fluxes from heat generation and heat loss at the boundaries and \tilde{A} is a matrix containing the fluxes between elements. The temperature vector was then solved for by multiplying the left side by \tilde{A}^{-1} .

To ensure that the model was correct, the bottom and top boundary conditions were set to adiabatic and a heat source was added to the center boundary. This created the condition of heat flowing radially though a pipe with inner radius equal to zero and outer radius, R , and length, L , for which an analytical solution exists,

$$T(r) = \frac{-Q \ln(\frac{r}{R})}{2\pi Lk} + T(R), \quad (5.7)$$

where Q is the flux from the center of the pipe and $T(R)$ is the temperature on the outside of the cylinder. Under these conditions, the FEA and analytical temperature profiles exactly match indicating that the code was working properly.

5.3.4 Raman Simulation

Lastly, the Raman spectrum from each model element must be generated. A Fano function was used to account for the natural asymmetry of the SiGe line shape, Eq. 3.12. The Fano function was fit to experimental Raman spectra of a 210 nm, $x = 0.25$ SiGe film (Sample 7) at temperatures ranging from 78 to 500 K. The temperature trends of the peak position, peak intensity and linewidth were then fit to 2nd order polynomials for use as temperature dependent inputs for the simulated Raman spectrum. The peak position and Q were also adjusted to account for Ge composition, while Q was held constant with temperature.

The resulting Raman spectrum was then generated by summing the Raman spectrum from each element in the sample. Each element Raman spectrum was generated by adjusting the peak position, width and intensity by the FEA predicted temperature of the cell. Additionally, the intensity was scaled by the absorbed laser

power, Eq. 5.5. However, rather than using the optical penetration depth, half the penetration depth was used due to the absorption of the Raman signal as it exits the sample to be collected.

After running the simulations with exact experimental values for the laser power and thermal conductivity, the laser power was adjusted to match the shape of simulated Raman spectrum to experiment and to match fits of experimental and simulated fits of the resulting Raman spectra. The thermal conductivity used for the simulations was 2, 1.2 and 1 W/m/K for $x = 0.15$, 0.2 and 0.25 films respectively, which is equal to that measured by time domain thermoreflectance from the Hopkins group at UVA. Details of the measurements are described elsewhere[48].

5.3.5 Results

In order to test if the laser power dependence of the Raman peak asymmetry in SiGe films was caused by inhomogeneous heating, the above model was used to simulate Raman spectra at various laser powers and Ge concentrations. Note, that the simulated laser power was adjusted so that the simulated and experimental Raman spectra closely match for one sample (25% Ge 210 nm thick) at one laser power 13 mW. This simulated laser power was, 52 mW, or four times the experimental laser power. The four times multiplier was then applied to the simulated laser powers of all three samples, 25%, 20% and 15% Ge, i.e., the laser powers used in the simulation ranged from 12 to 52 mW, while the experimental laser power ranged from 3 to 13 mW. Note, that the effect of composition was solely modeled as a change in thermal conductivity.

Figure 5.10 plots the simulated (left column) and experimental (right column) Raman spectra at various laser powers and Ge compositions. First note that the simulated spectra closely match the experimental spectra at all Ge compositions. For $x = 0.15$ (a and d) and 0.20 (b and e), the asymmetry increases with laser power, but

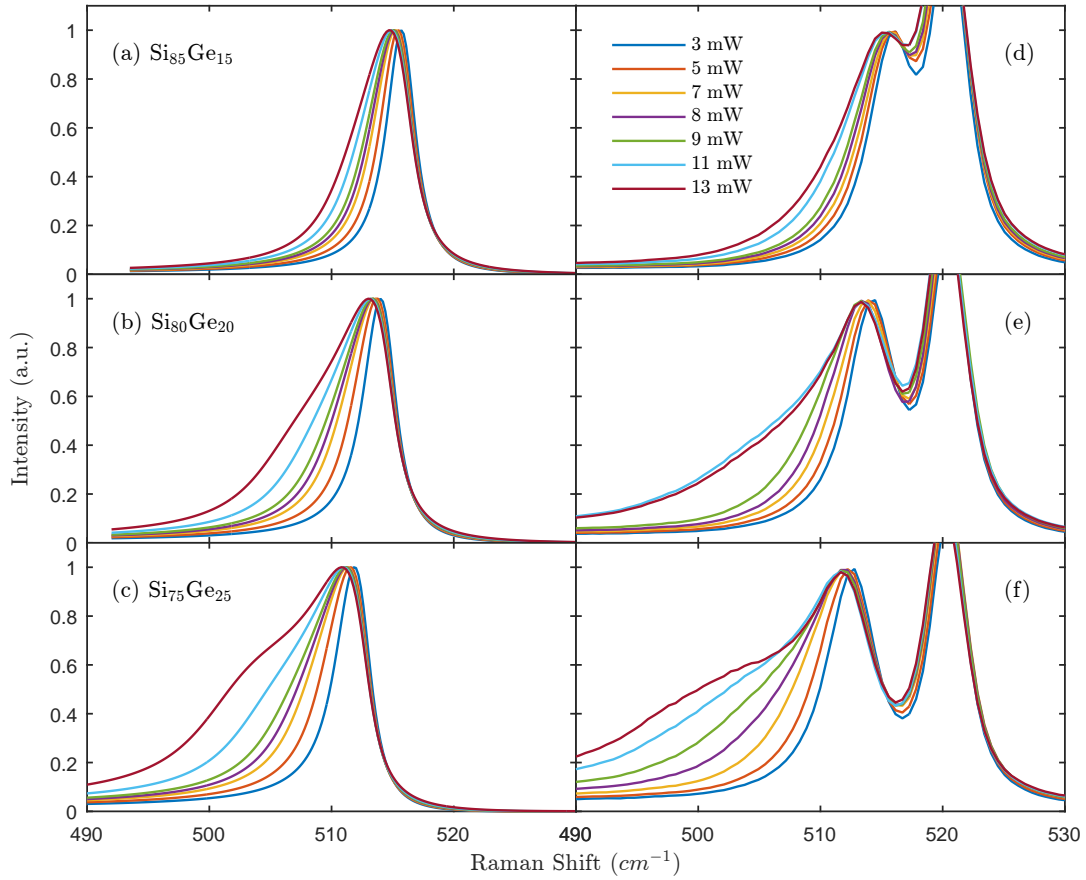


FIGURE 5.10: Left column plots simulated Raman spectra for various Ge contents at various laser powers. The right column plots the experimental analog.

in the $x = 0.25$ spectra (c and f) a hump begins to form at the highest laser powers. This could be perceived as another peak emerging due to surface or confined modes. However, the second peak (L-peak) is also observed in the simulated spectra where no surface or confined modes are modeled. This implies that the asymmetry with laser power is solely due to temperature gradients in the sample.

In order to look at the magnitude of the temperature gradients needed to create a perceived peak splitting, Figure 5.11 plots the temperature map of the simulation for the 25% Ge sample at the highest laser power, 13 mW experimental and 52 mW simulated. Note that the maximum temperature in the simulation is roughly 750 K, meaning laser heating created a 350 K temperature rise. This is an order of magnitude higher than the temperature measured using the peak position from a single peak fit,

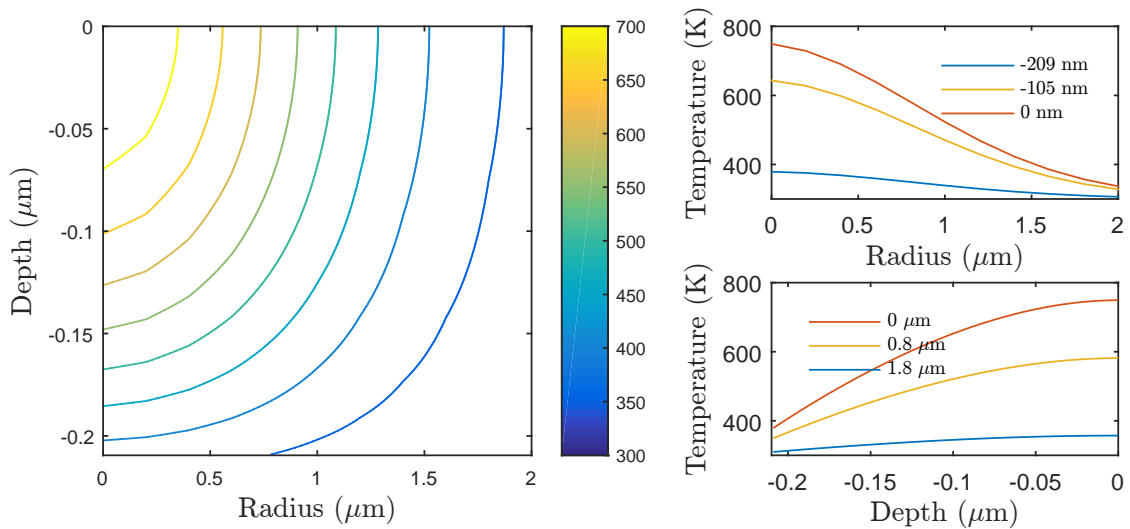


FIGURE 5.11: Temperature profile of 210 nm thick $\text{Si}_{75}\text{Ge}_{25}$ film heated by 52mW 488 nm laser (compare to 13 mW experiment).

see Fig. 5.3. This suggests that using the single peak position to measure temperature of inhomogeneously heated system is not accurate. The Raman microscope probes a volume of the sample which may not have a constant temperature. The spectrum will, therefore, be a convolution of the range of temperatures in the volume weighted by the laser penetration depth. This is likely also true when measuring other properties that may be inhomogeneous in a material, such as strain and composition.

To further compare these simulated results to experiment, the simulated spectra are fit to two peaks, L-peak and H-peak, in the same way as in Fig. 5.5. The results, Fig. 5.12, show that the (b) peak positions and (d) associated temperatures of the L-peak and H-peak for the simulated (solid lines) and experimental (markers) follow the same trends with laser power. This further supports the hypothesis that the change in asymmetry with laser power is due to inhomogeneous heating.

These results also suggests that laser heating has a much stronger effect in low thermal conductivity systems than expected by single peak position fits as shown by the maximum simulated temperature in Fig. 5.5 (c). Since the Raman line shape is

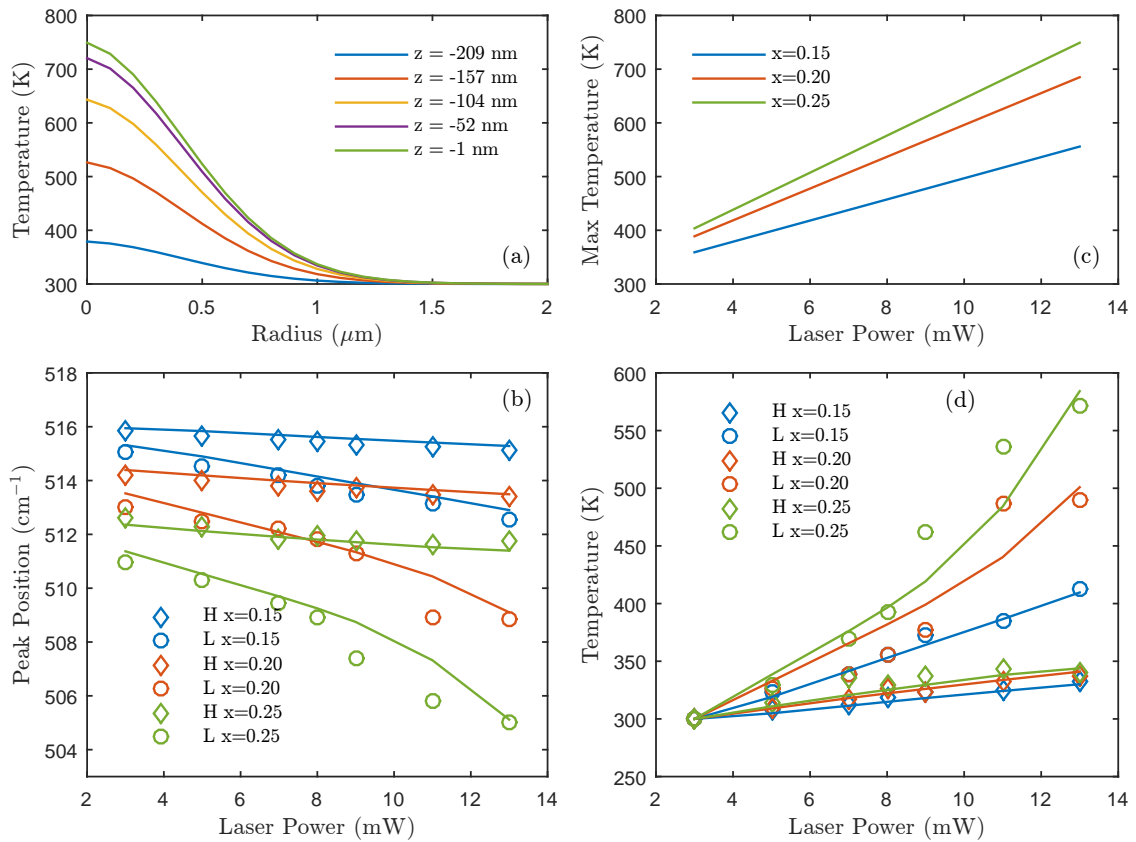


FIGURE 5.12: Results of the simulated (solid lines) and experimental (diamonds and circles) 488 nm laser heating of 210 nm SiGe films. (a) The temperature profile at various depths of the $x = 0.25$ SiGe film irradiated with 13 mW (52 mW simulated). (b) Peak position of two peak Fano fits to the heated experimental and simulated spectra at various laser powers. (c) Maximum temperature when irradiated at various laser powers. (d) Temperature of experimental and simulated films based on peak position fits.

temperature dependent, measurements of the linewidth and asymmetry will therefore be significantly biased by the laser heating. This underscores the importance of selecting the conditions of the Raman experiment to minimize measurement induced biases, in this case minimizing laser heating.

Finally, a comment on the factor of four difference between the simulated and experimental laser power. The reason that the simulation required a higher laser power than experiment is likely because (1) a classical FEA model was used to simulate nanoscale heat transfer and (2) simulated material properties (e.g., penetration depth, reflectivity, thermal conductivity, etc.) were not modeled as

temperature dependent. At 210 nanometers, the wavelength of many of the phonon modes are longer than the thickness of the film leading to size effects that classical models are not equipped to handle. As can be seen from temperature dependent measurements of the Raman spectra, the penetration depth decreases as the film temperature rises (not shown). This will lead to a higher power density being deposited at the surface of the film at high temperatures, which in turn leads to higher temperature gradients in the film and high asymmetry in the peak. Similar compounding effects may also occur if the temperature dependence of other material properties are accounted for.

5.4 Conclusions

By combining the measurements of various powers and wavelengths, we have measured the effect of laser power density on the asymmetry of the Raman peak in SiGe films. Using these measurements, the contributions to the asymmetry of the Raman peak from three separate phenomena were investigated, namely (1) Fano resonance, (2) overlapping disorder and bulk-like peaks and (3) inhomogeneous heating. Fano resonance was rejected as a contributor to the peak asymmetry since it did not show a wavelength dependence at low powers. Furthermore, Fano resonance could not explain the peak splitting at high laser powers. Experimental evidence to support or disprove the hypotheses of a dual mode peak or inhomogeneous heating, on the other hand, were inconclusive.

Varying the film thickness in an attempt to change the thermal resistance of the film and thus the laser heating was inconclusive since the penetration depth of the 488 nm laser is much larger than the film thicknesses used. Using a 405 nm laser with a much smaller penetration depth, did not resolve the issue since the asymmetry was not reproducible with this wavelength, even though the power densities of the 488 and 405 nm lasers were similar. This may be because the 405 nm wavelength is resonant

with the bulk modes, so that the disorder modes are unobservable. Alternatively, it may be because the laser power was not high enough to induce changes in the peak asymmetry. This was tested by changing the disorder of the film through a change in alloy composition, in an effort to change the ratio of disorder and bulk-like modes. The results showed that as the Ge fraction increased the magnitude of the peak asymmetry and even peak splitting increased, which supported the dual mode peak hypothesis. However, because the thermal conductivity changed with composition, inhomogeneous heating could not be ruled out. Therefore, the effects of laser heating on the Raman spectra were modeled using a custom steady state FEA model. The model showed that the asymmetry and peak splitting can be replicated by only accounting for changes in incident laser power and film thermal conductivity. However, a simulated laser power four times the experimental laser power was required to recreate these results, yielding some doubt in the results.

One of the primary goals of this study was to ascertain the cause of the asymmetry in the Raman peak, to ensure that asymmetry can be used as a metric for localization of Raman modes. While the results of this study do not make strong conclusions on the exact cause of the asymmetry, they do show that the asymmetry is related to the disorder in the alloy and thus can be used to quantify localization. If the change in asymmetry is due to inhomogeneous heating, then as long as the laser power is low enough to prevent heating, the peak asymmetry results from a disorder induced breakdown of selection rules similar to phonon confinement. Alternatively, if the hypothesis of a dual mode peak is correct then the asymmetry can still be used as a metric for localization of modes since the asymmetry is caused by the appearance of localized disorder modes in the spectrum. However, in an effort to mitigate any influence of these effects, studies in Chapter 6 are performed using the 405 nm laser, which did not influence the peak asymmetry.

Chapter 6

Phonon Scattering in SiGe Alloys

6.1 Introduction

Thermal conductivity in non-metals is generally modeled by treating the thermal energy carriers (phonons) as a gas of particles using the phonon gas model (PGM)[11]. Using this model, thermal conductivity is a function of the energy each particle carries (specific heat), the speed at which the particle carries that energy (group velocity), and the frequency of collisions with other particles or obstructions (scattering rate). When modeling thermal transport, vibrations are assumed to behave like plane waves and thus have a defined wavevector and spatially extend throughout the system. This assumption is valid for bulk crystalline systems, due to the periodic symmetry of the crystal. However, as the local symmetry is broken through the introduction of impurities[90, 174], vacancies in the crystal, or by nanoscaling[101], the vibrational modes become localized[78].

Since vibrations in non-periodic systems cannot be described by plane waves, Allen and Feldman defined all disordered vibrational modes as vibrons, which are composed of propagons, diffusons and locons[12]. Propagons are low frequency delocalized vibrations with plane wave-like motion, diffusons are mid-frequency partially localized vibrations, and locons are strongly localized high frequency

modes. As modes become localized, their ability to contribute to thermal conductivity is diminished since they are confined to a small spatial region in the material and thus are not able to move energy through the material. In addition, the disorder and nanoscaling localizing the modes, also creates static scattering sites that further reduce thermal transport.

Localized modes are most often investigated theoretically since the models used in experimental studies treat the effects of disorder and nanoscaling[48] as a change in the scattering rates. The models used in experimental studies assume that the material is semi-infinite and that any disorder or nanoscaling is treated as a perturbation to the system accounted for by augmenting the temperature independent scattering rates[50]. However, when the magnitude of the perturbation Hamiltonian becomes comparable to the system Hamiltonian, such as in an alloy, ultra thin film or amorphous material, perturbation theory is not applicable[97, 175]. Additionally, most recent theoretical studies have shown that disorder and nanoscaling reduce thermal conductivity by removing the ability of phonons to transfer thermal energy through the material instead of only affecting the scattering[78, 90]. Therefore, paradigms are needed to account for the influence of disorder and nanoscaling on both the nature (localization) and behavior (scattering) of the vibrations. Here we leverage the Raman response of SiGe towards that end.

Raman spectroscopy is uniquely adept for investigating localization and scattering of vibrations since it can directly probe the scattering rate and localization of Raman active modes independently. The scattering rate of Raman active modes in crystalline materials is directly related to the linewidth, Γ , of the Raman peak through the uncertainty principle[144]. For small perturbations of the crystallinity, such as doping or in a dilute alloy, the peak will symmetrically broaden due to the impurity scattering. However, when the translation symmetry is strongly perturbed by nanoscaling or disorder, the peak will asymmetrically broaden due to

localization of the Raman modes and break down of the Raman selection rules[101]. By fitting the peaks to an appropriate function, the symmetric and asymmetric broadening can be measured simultaneously to quantify scattering rates and localization. While these results can not be directly linked to thermal conductivity, since acoustic modes are the primary thermal transport mechanism, these results provide insight into fundamental vibrational physics.

Numerous studies have used Raman spectroscopy to measure the localization of Raman modes in nanoscaled structures, such as nanowires[111, 159, 160], nanocrystals[107, 112, 154, 154, 176] and superlattices[177], via analysis of the asymmetry of the Raman peaks. At the same time, defects[104, 116] and alloying[115, 116, 120, 121, 136] have been shown to break the local symmetry of the crystal while also creating scattering sites[178], leading to a symmetric and asymmetric broadening of the Raman linewidth. However, none of these studies have systematically investigated how breaking of the translational symmetry of the crystal influences both the localization and scattering rates in concert. Additionally, none of the localization studies investigated the temperature dependence of localizing material properties to gain insight into the interplay between scattering and localization. In response, this study uses Raman spectroscopy to investigate how alloying, dislocations and nanoscaling influences both the nature and behavior of Raman active vibrations in $\text{Si}_{(1-x)}\text{Ge}_x$ thin films.

In this work, temperature dependent Raman measurements of asymmetry and linewidth were collected from SiGe alloys while varying the levels of alloy disorder, dislocation disorder, and nanoscaling. The results of this study show that some types of disorder influence both scattering and localization, while others only affect scattering. Additionally, the scattering rate of each disorder type has a different temperature trend which is correlated to localizing effects. Furthermore, localization is temperature dependent, implying that the normal modes evolve with temperature.

TABLE 6.1: This table summarizes the samples that will be used in this study. The parenthesis next to the growth method (CVD or MBE) indicate the growth temperature while x indicates the fractional Ge concentration of the alloy film. Each number in the table is the sample number which is used to identify each sample for the discussion.

MBE (400 °C) film thickness	Ge Fraction, x			CVD (750 °C) film thickness	Ge Fraction, x		
	0.15	0.2	0.25		0.15	0.2	0.25
40 nm			5	39 nm			1
90 nm			6	88 nm			2
210 nm	9	8	7	202 nm			3
427 nm				427 nm			4

6.2 Experimental

6.2.1 Samples

Phonon physics in bulk, crystalline systems is well understood, while understanding of amorphous phases is ever advancing[12, 15, 16]. However, there is a significant lack of understanding of vibrational physics in the transition region between periodic and disordered states where perturbation theory does not apply. Here, this region is investigated by introducing significant perturbations to the periodic lattice of Si in the form of disordered Ge alloying, dislocations and nanoscaling. The goal of this study is to choose the level of perturbation to be sufficiently high that localization effects are observed but still compete with scattering processes (i.e. diffusion region), to gain insight into how defects influence the scattering and localization of vibrations. Several studies have shown that disordered crystalline alloys contain modes that are not plane wave like due to breakdown of the translational symmetry[4, 17, 122]. However, the level of localization is less than in amorphous systems[12, 15, 16]. Therefore, four series of SiGe alloy samples were grown (see Table 6.1 and Fig. 6.1); a thickness series with varying dislocations (Samples 1-4), a thickness series with a consistent low level of dislocations (Samples 5-7), an alloy series (Samples 7-9) and a dislocation series (Samples 3 and 8).

Samples 1-4, the thermal conductivities of which were studied in Ref. [48], were

thick, undoped Si(001) wafers. The epitaxial alloy films were grown in a custom, ultra-high vacuum, hyperthermal molecular beam epitaxy (MBE) system. The MBE system has a base pressure of 1×10^{-10} Torr and is equipped with variable-distance magnetron sputter guns with Ge and Si as target sources. Prior to insertion into the MBE system, Si(001) substrates were chemically cleaned using a modified IMEC/Shiraki process[179], creating a passive SiO_x layer in the final step. The passive SiO_x layer was desorbed *in situ* at 800°C after an overnight temperature ramp, plus 5 hr. prebake at 600°C . The substrate was then cooled to 720°C for the deposition of a 50 nm Si buffer layer. $\text{Si}_{(1-x)}\text{Ge}_x$ epitaxial films were grown at 400°C with the chamber pressure maintained at 5 mTorr of getter- and LN_2 -purified Ar throughout the deposition. All samples used were 0.5 cm square sections taken from the center of the growth wafer.

6.2.2 XRD Characterization

The thickness of the alloy film, d , was characterized *ex situ* by X-ray reflectivity (XRR). The X-ray diffraction (XRD) instrument used was a Rigaku SmartLab X-ray diffractometer[180] with a 3kW copper sealed tube generator. All the measurements were made at a wavelength of $\lambda = 1.5406\text{\AA}$ obtained using a parallel beam Ge 220×2 -bounce monochromator. Ge composition, x , and the strain relaxation, r , in the films were determined by measuring the 004 and 224 reflections from the sample via conventional “ $\theta - 2\theta$ ” and rocking curve (ω) scans in XRD[181, 182], see Fig. 6.2. Additionally, the average dislocation spacing, σ_{dis} , of the CVD grown films was characterized in the CVD grown films using plan-view TEM[48] and the measured¹ strain[183]. Results are presented in Table 6.2.

As the CVD film thickness increases, both the strain relaxation and dislocation density increases, while the MBE grown film relaxation remains roughly constant and much lower than the CVD grown films. Also, note that the alloy composition in MBE

¹Relaxation was shifted to ensure no negative values by adding a 14% offset.

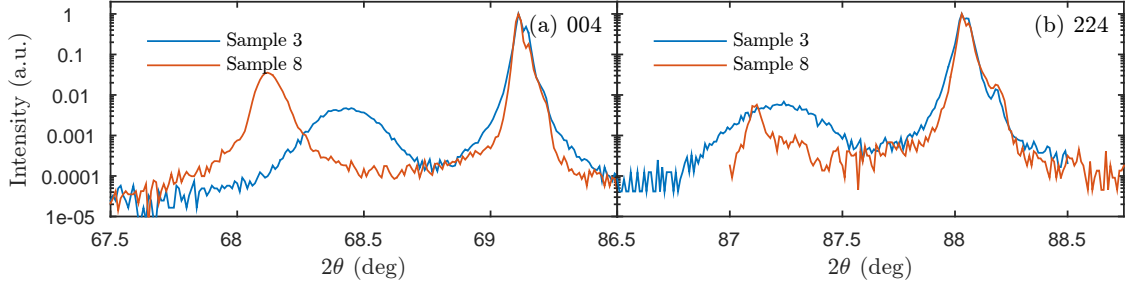


FIGURE 6.2: XRD reflections of Sample 3 ($d = 202$ nm, $x = 0.18$) and Sample 8 ($d = 210$ nm, $x = 0.19$) in the (a) 004 and (b) 224 directions. These results show the strain relaxation from dislocations in the CVD grown films (Sample 3).

TABLE 6.2: This table summarizes material properties, film thickness (d), Ge fraction (x) and percent strain relaxation (r). Samples above the dashed line were grown using CVD and below using MBE. The average spacing of dislocations, σ_{dis} , and Ge atoms, σ_{Ge} , is also shown.

Sample #	x	d (nm)	r (%)	σ_{dis} (nm)	σ_{Ge} (nm)
1	0.17	39	-10	672	0.60
2	0.18	88	23	73	0.59
3	0.18	202	61	36	0.59
4	0.18	427	82	28	0.59
5	0.25	40	-14	900	0.53
6	0.29	90	-2	224	0.50
7	0.24	210	-6	336	0.54
8	0.19	210	-11	896	0.58
9	0.14	210	3	158	0.54

thickness series, Samples 5-7, is not constant. Sample 6 is particularly compositionally mismatched from the other two and so will be excluded from the results presented in the following section. However, due to the angular difference of the Si and Ge targets in the MBE system, the composition of the alloy continuously varies from one side of the growth wafer to the other by nearly 15%. This will be particularly advantageous for adjusting composition in future directions discussed at the end of this chapter.

6.2.3 Raman Measurements

As discussed in Chapter 3, the line shape of the Raman peak will be used to quantify scattering rates and localization in the aforementioned SiGe samples. The

linewidth (FWHM) of the Raman peak is proportional to the scattering rate of the Raman active vibrations through Eq. 3.7. Equation 3.7 is applicable to highly ordered materials where the only Raman active vibrations lay at the zone center of the Brillouin zone. However, in disordered and nanoscaled samples, confinement of the modes leads to an additional asymmetric broadening which is caused by breaking of the Raman selection rules so that modes away from the Brillouin zone center contribute to the Raman signal. The width of wavevectors in the Brillouin zone that contribute to the Raman spectrum, Δq , is inversely proportional to the spatial extent of the vibration which is dictated by the limiting dimension of the crystal, d (e.g., thickness of a thin film, the grain size in a poly-crystalline material or the effective crystallite size in an alloy). Therefore, the magnitude of the asymmetry was used as a metric for the localization of the Raman modes.

In order to fit the linewidth and asymmetry of the Raman peaks simultaneously², the Fano function was used, as discussed in Chapter 3. The asymmetry is most commonly presented in literature as a ratio of half linewidths on the left side of the peak, Γ_L and right side of the peak, Γ_R . After fitting to the Fano function, we adhere to this convention by plotting the ratio of half widths instead of the Fano asymmetry parameter, Q , in order to facilitate easy comparison with literature.

Raman spectra were collected on a Renishaw InVia Raman microscope using a 405 nm diode laser and 1800 g/mm grating in the -2 order yielding a spectral resolution of 0.7 cm^{-1}/px . The 405 nm laser was chosen due to its small penetration depth, approximately 60 nm, in $\text{Si}_{80}\text{Ge}_{20}$. The small penetration depth reduces the Raman signal generated and collected from the Si substrate, the peak ($\sim 520 \text{ cm}^{-1}$) from which is very near the Si-Si vibration peak in the SiGe films ($\sim 515 \text{ cm}^{-1}$). As discussed in Chapter 4, minimizing the relative intensity of the substrate peak to the film peak is crucial to minimizing the uncertainty of the measured linewidths and asymmetry.

Room temperature and temperature dependent measurements were collected on

²The overall FWHM of the peak is only significantly influenced by the asymmetry when $5 > Q > -5$, so that Γ and Q are largely independent parameters.

all samples. Room temperature measurements allow for investigations of how scattering rates and localizations are influenced when breaking the periodicity of the crystal. Temperature dependent measurements of scattering rates allow fitting to model functions to determine if alloying, dislocations and boundaries can be considered static scattering sites, or if they also influence phonon-phonon interactions. Simultaneous temperature dependent measurements of vibrational localization were collected to investigate how modes evolve with temperature.

Temperature dependent measurements were taken using a Linkam THMS600 cryogenic stage. Measurements were taken from 78 K to 473 K at 25 K increments, with 5 spectra at 5 different sample locations collected at each temperature. Each temperature was allowed to equilibrate for a minimum of 20 minutes before collecting data. In order to minimize biases caused by drift, spectra were taken first from 78 K to 473 K in 50 K increments and then from 448 K to 98 K in 50 K increments.

Raman spectra were collected using a 50x 0.5 NA objective which yields a spot diameter of roughly 4 μm diameter, with incident laser power chosen to minimize heating, ≈ 1 mW. Laser heating can cause the linewidth and asymmetry to increase, masking the effects of material properties[92], especially, in nanoscaled low thermal conductivity materials[160, 163, 164]. Room temperature measurements were taken outside the temperature stage using a 50x 0.75 NA objective to improve signal collection, with 25 spectra collected from each sample at 25 different locations.

6.3 Results

The results of the Raman measurements allow for investigations of both the changes in behavior and nature of vibrations with a change in the periodicity of material systems. Room temperature results are used to compare how disorder and nanoscaling influence the overall scattering rate and mode localization. Temperature

dependent measurements are then used to separate the temperature dependent and independent components of the linewidth. These two components will provide insight into whether a change in material property influences static elastic scattering (temperature independent), or whether inelastic phonon-phonon scattering is mediated through static scattering sites and disorder (temperature dependent). The effects of alloying and dislocations are presented first, followed by nanoscaling.

6.3.1 Alloy and Dislocation Disorder

Scattering rate equations for disordered alloys and for dislocations have been derived for use with the phonon gas model for decades. These equations are nearly unanimously temperature independent. They also predict that the scattering rate is proportional to the phonon frequency to the n^{th} power and to the density of the alloy species or dislocation sites. When they are applied to the PGM, it is under the assumption that scattering sites do not change the plane wave nature of modes. In order to test these trends and assumptions in non-periodic systems, the scattering rate and localization was measured in a set of alloy and dislocation disordered SiGe alloys. Specifically two series of samples are used for these investigation (Fig. 6.3): (left) alloy series with Ge fraction ranging from 14-24% and (right) a series with a constant Ge composition but different levels of dislocations. The color of the text corresponds to the color of its respective data presented in the figures of this discussion.

Room Temperature

Figure 6.4(a) plots the linewidth of the Raman peak as a function of Ge fraction. As the concentration of alloy species increases, a corresponding increase in linewidth is observed. This is because as randomly placed Ge atoms are added to the Si crystal, the relative disorder increases leading to an increase in scattering rates. This is exactly what is expected by alloy scattering rate equations. However, what is not predicted

then the phonons will not feel its localizing effect unless the smaller cage (alloy disorder) is removed. As we can see from Table 6.2, the dislocation spacing, σ_{dis} , is larger than the Ge atom spacing, σ_{Ge} . Therefore, the localizing effects of dislocations are weak due to the presence of the stronger alloy disorder effect. However, dislocations still create scattering sites and thus the increased scattering rate observed via the linewidth.

Temperature Dependent Scattering

When disorder changes the nature of vibrations, as we saw for the alloy series above, scattering rate equations derived for plane waves may not be applicable. In this case, the frequency and temperature trends of scattering rate equations may not be accurate. This hypothesis can be tested by measuring the temperature dependence of the scattering rates with varying degrees of disorder. The temperature trends of the linewidth can then be used to determine whether disorder scattering is a temperature independent effect (i.e. elastic or harmonic scattering) consistent with perturbation theory or if disorder influences multi-phonon scattering processes (i.e. inelastic or anharmonic scattering).

If any of the scattering types being investigated are temperature dependent, then a change in material property will yield a change in slope of the temperature trend. However, if the scattering type is temperature independent, then the scattering rate will change equally for all temperatures. To determine the change in slope quantitatively, each temperature series was fit to two models: the PGM scattering rate model and the Klemens phonon decay rate model. Very similar results were found for each fit, but the former yielded greater uncertainties than the latter. Therefore, only the fit results from the Klemens 3-phonon decay model, Eq. 3.9, are plotted in Fig. 6.5.

Figure 6.5 (a) presents the temperature independent decay contribution to the linewidth, Γ_0^I , while Fig. 6.5 (b) presents the temperature dependent contribution,

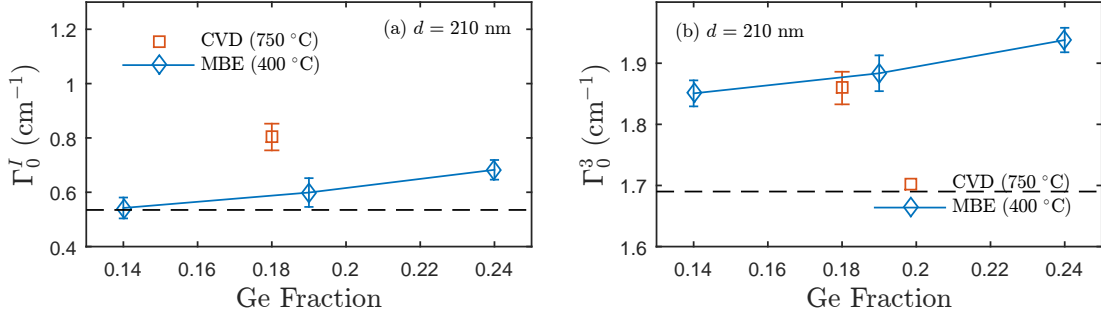


FIGURE 6.5: Temperature (a) independent, Γ_0^I , and (b) dependent, Γ_0^3 , components of the scattering rate extracted from temperature dependent linewidth measurements of the alloy and dislocation series, Fig. 6.3, using the Klemens 3-phonon decay model, Eq. 3.9. Dashed line are the results of the fit for bulk Si(100).

Γ_0^3 . The dashed lines represent fit values for bulk Si used for comparison. Notice that temperature independent results are very similar to the room temperature linewidth results shown in Fig. 6.4 (a). As Ge fraction increases, so does the temperature independent scattering rate. Introduction of dislocations leads to a further increase in scattering rate. The reasons for the temperature independent trends are the same as arguments made for room temperature linewidth results above.

Figure 6.5 (b) plots the temperature dependent linewidth contribution versus composition. As the Ge fraction, and disorder, increases, the temperature dependent term also increases. The trend is similar to the room temperature localization trend, Fig. 6.4 (b), and so is speculated to be due to dispersion blurring. When disorder is introduced into a system the plane wave nature of vibrations decreases. This means that some level of uncertainty exists in the wavevector, leading to a broadening of the dispersion where modes are localized[17, 46]. This broadening makes it easier to satisfy conservation of momentum and energy relations, which in turn leads to more inelastic “phonon-phonon” scattering. Furthermore, notice that compared to bulk silicon, alloying primarily increases the temperature dependent scattering rate. This implies that the primary cause of optical mode scattering in disordered alloys is disorder induced “phonon-phonon” scattering. The introduction of dislocations does not further increase localization, as

previously discussed for the room temperature results, and therefore does not strongly influence the temperature dependence of the scattering rate.

These results show that alloying has a strong effect on localization and scattering, while dislocations only influence scattering rates. However, this may only be true in this case. If alloy disorder is reduced to the point that it is not the primary localizing effect, dislocation may contribute to localization of vibrations. These results also show that alloying increases the disorder of a material which localizes the modes leading to an increase in anharmonic scattering. However, since dislocations do not effect localization the anharmonic scattering is not affected. In summary not all disorder effects the nature and behavior of vibrations similarly.

6.3.2 Size Effects

Owing to the strong scattering induced by the alloying, size effects may have only a minimal effect on the linewidth (scattering) and asymmetry of the Raman modes (localization). However, several efforts have shown that nanoconfinement localizes the modes. Since localization was shown to influence inelastic scattering in the previous section, size effects may manifest in a similar manner here despite the small effect expected from the PGM. To test this hypothesis temperature dependent measurements of the linewidth were performed for two series of SiGe alloy films with varying thickness diagramed in Fig. 6.6 and described in Section 6.2.1.

Room Temperature

Scattering rate equations predict that optical modes should not feel the effects of boundaries since alloy scattering is predicted to be much stronger[48]. However, Fig. 6.7 (a) shows that as the film thickness increases the linewidth of both sample sets generally decreases, implying that boundary scattering decreases with film thickness. The increase in scattering rate between the 39 nm and 88 nm film is likely due to the onset of dislocation fault formation as shown by XRD measurements of relaxation and

localization trend with film thickness. The two material properties that are known to change in the four CVD films are the thickness and dislocation density. One could initially hypothesize that as the film thickness increases and the dislocation density increases there are counter effects on the localization of the modes that leads to a flat trend in the localization. However, in the previous disorder discussions it was shown that dislocations do not localize modes. It is possible that another material property is changing in the CVD films with thickness that is masking size effects.

Due to the conflicting result of the MBE and CVD size dependent studies, I recommend that these results be extended to more thicknesses and compositions. This will allow for a more systematic investigations into the competition between alloy disorder and boundary scattering effects. As previously mentioned, the current series of MBE films were grown for a wide range of compositions and 3 thicknesses. Therefore, no new samples would need to be grown to complete these extended studies. At the time of writing this dissertation, the 405 nm Raman laser was inoperable. However, I intend to perform these studies upon acquisition of a replacement laser.

Temperature Dependent Scattering

As was done for the alloy disorder investigations, the temperature dependent scattering rates were fit to the Klemens 3-phonon decay model to extract the effects of nanoscaling on temperature dependent and independent scattering. Figure 6.8 plots the (a) temperature independent and (b) dependent components of the linewidth. Similar to the alloy series, the temperature independent linewidth follows very similar trends as the room temperature result; as the film thickness decreases boundary scattering increases.

Unlike the alloy case, however, the temperature dependent component of the linewidth does not follow the localization trend. The localization decreases with film

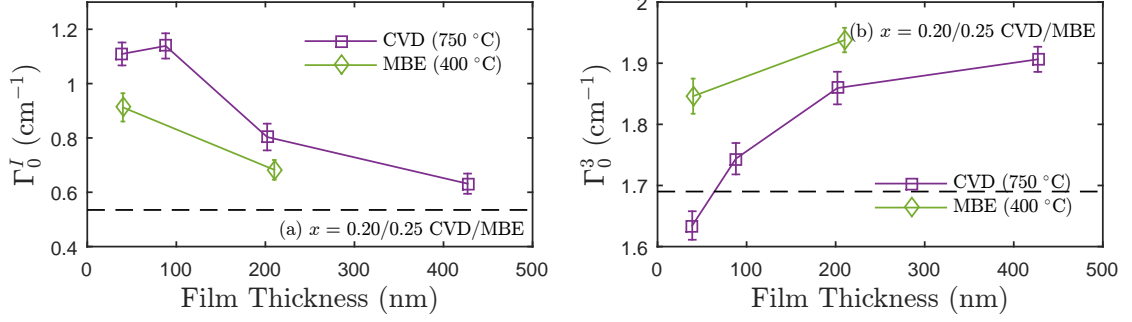


FIGURE 6.8: Temperature (a) independent, Γ_0^I , and (b) dependent, Γ_0^3 , components of the scattering rate extracted from temperature dependent linewidth measurements of the size effects series, Fig. 6.6, using the Klemens 3-phonon decay model, Eq. 3.9. Dashed lines are the results of the fit for bulk Si(100).

thickness for the MBE series (diamonds), while Γ_0^3 increases. In the CVD films (squares), a similar increasing trend of Γ_0^3 with thickness is seen. This suggests that nanoscaling decreases inelastic scattering, which is counter to the results of the disorder studies. This suggests that different localization mechanisms (i.e., disorder and nanoscaling) effect scattering differently. The cause of these changes is speculated to be due to nanoscaling reducing the number of modes available for the Raman mode to scattering into rather than to increase the number as in the alloying case.

These results show that nanoscaling affects both localization and scattering of vibrations, which in turn influences “phonon-phonon” scattering. However, as nanoscaling localizes the modes through confinement the “phonon-phonon” scattering decreases, counter to the alloying case. This result suggests that different localization mechanisms influence temperature dependent scattering differently.

6.3.3 Localization Temperature Trends

The previous section showed that large perturbations away from a periodic atomic structure influence the behavior of vibrations more than just through a temperature independent scattering rate. In order to complete the story, the temperature dependence of the nature of the modes is investigated. The room

temperature results have already shown that disorder localizes these modes, here the focus centers on understanding the degree to which this localization varies with temperature.

Figure 6.9 plots the Raman peak asymmetry, Γ_L/Γ_R , as a function of temperature for the (a) MBE thickness series, (b) dislocation series, (c) alloy series and (d) dislocation and thickness series. The first thing that is apparent is that the asymmetry parameter, and thus localization, is not constant with temperature. This means that as temperature increases, the modes become less plane-wave like. Since localization reduces thermal conductivity³, temperature dependent localization implies that the temperature dependence of a localized modes thermal conductivity is a function of both the scattering rates and vibrational localization. This is counter to the conventional thought that reductions in vibrational energy transport occurs through scattering.

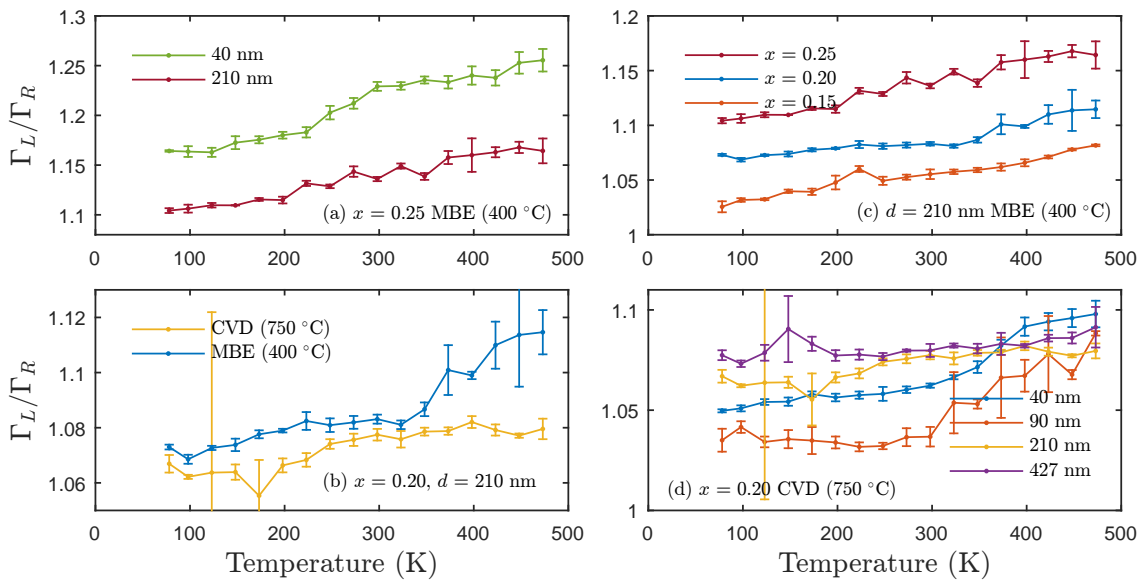


FIGURE 6.9: Localization as a function of temperature for the (a) MBE size effects series, Fig. 6.6, (b) dislocation series, Fig. 6.3, (c) alloy series, Fig. 6.3, and (d) the CVD size and dislocation effects series, Fig.6.6.

Looking more closely at the individual series we can see that most of the

³Localization does not necessarily reduce thermal conductivity in superlattices.

temperature trends are a roughly linear function of temperature. Since there is currently no model to predict the temperature dependence of the mode localization, discussions of the temperature trends must be qualitative. For the size effects series, Fig. 6.9 (a), a decrease in thickness results in a roughly constant increase in asymmetry over all temperatures. Since the slope of the curve does not change, this indicates that alloying is a temperature independent localization effect.

Contrary to the alloy and thickness series, temperature trends in the dislocation series, and size and dislocation series are not constant. In Fig. 6.9 (b), we see that the trend flattens with the addition of dislocations, especially at high temperature. Furthermore, we can see that as the film thickness increases in the size and dislocation series, Fig. 6.9 (d), the temperature trend decreases. Since we know from Fig. 6.9 (a) that boundary localization is temperature independent, the trend change must come from dislocations, indicating dislocation localization does not occur until high temperature (> 300 K). This might also be the reason we do observe strong dislocation localizing effects in the room temperature measurements. Without a model for how modes should localize with temperature, it is not possible to definitively comment on the cause of the localization temperature dependence. However, if we think about what happens to the atomic positions as temperature increases it is possible to hypothesize a cause for the localization temperature dependence.

The normal vibrational modes of a system are often calculated using lattice dynamics[184]. The most common procedure when using lattice dynamics for modal analysis is to define a system of masses which interact through an empirical potential. The system is then relaxed to the lowest energy state and then the dynamical matrix describing the system is solved to yield the vibrational eigenvectors and energies. Since atomic positions are set to the minimum of the respective potential wells, these modes are calculated for the absolute zero condition, 0 K. However, above 0 K, the atoms have a finite energy and thus a finite

amplitude of oscillation about the potential minimum. If we take a snap shot of these oscillations, then the atoms will have a small amount of spatial disorder due to the finite amplitudes of oscillation. If we calculate the normal modes of the system in the temperature induced disorder state, then the normal modes will not all be planewaves since the periodicity of the system has been broken. As temperature rises and the oscillations increase, then the spatial disorder at any given time will also increase leading to a further departure of the modes from plane wave nature. I hypothesize that this is the reason for the localization temperature dependence seen in the Raman spectra.

6.4 Conclusions

Most often thermal conductivity in non-metals is modeled using the phonon gas model, which treats vibrational thermal transport as diffusion of vibrational particles (phonons). This description is predicated on the assumption of a periodic arrangement of atoms. Any disruption of the periodicity, such as mass impurities, dislocations or boundaries is treated as a perturbation to the periodic structure through temperature independent scattering rate term. These assumptions work well for highly periodic systems, but when the periodicity is broken through high levels of disorder, such as in an amorphous material or disorder alloy, this treatment breaks down. The reason for the break down is that the modes can no longer be thought of as particles which can diffuse through the entire system. Instead disorder localizes the modes to finite regions in the materials system while also creating scattering sites for the modes. In the alloy case studied in this chapter, thermal transport is dominated by acoustic modes which were not studied. However, these results show how localization and scattering work in conjunction to influence the thermal transport of a particular vibration.

This work investigated the effects of alloy and dislocation disorder, and

nanoscaling on both the nature and behavior of vibrational modes experimentally using the lineshape of the Raman spectrum in SiGe alloy thin films. Of particular interest was understanding how vibrational physics transitions away from the phonon perspective with disorder and nanoscaling.

This work showed that alloy disorder, dislocation disorder, and nanoscaling influence both the scattering rates and localization simultaneously. It was first shown that optical modes scatter with boundaries counter to the predictions of conventional scattering rate equations, Eqs. 2.3-2.6. It was also shown that alloy, dislocation and boundary scattering rates are not temperature independent. Alloying increases temperature dependent scattering by localizing modes which makes it easier to satisfy conservation of energy and momentum rules and in turn increases inelastic scattering. On the other hand dislocations do not influence the temperature dependence of the scattering rate since dislocations do not increase localization, but do strongly increase temperature independent scattering. This implies that not all disorder is not created equally when considering its effects on temperature dependent inelastic scattering. Nanoscaling increases temperature independent scattering but decreased the temperature dependence. Furthermore, alloying and nanoscaling have a temperature independent localization effect, while dislocations flatten localization temperature trends.

For the first time experimentally, this work measured both scattering rates and localization as a function of temperature versus a systematically varied set of material properties and showed that moderate levels of disorder influence both the nature and behavior of vibrations. Future investigations should be performed to ascertain the cause of the localization temperature dependence with specific emphasis on developing models to predict the temperature and material property dependencies. Future work should also be performed experimentally to measure scattering and localization in other material systems. A first experimental step would be to use the current MBE samples which have varying alloy composition across the grown wafer to look at size

effects at various compositions. Thinner film thickness or nanograined samples should also be investigated to add data points to the thickness series and push investigations into the ultra-thin regime. Finally, the effects of alloy order at a specific composition should be investigated to see how the behavior and nature evolve with increasing disorder but without the addition of impurities or additional alloy atoms.

Chapter 7

Conclusions

7.1 Summary of Conclusions

Nanoscaled and disordered material systems have aided in the advancement of a range of devices, such as transistors, quantum cascade lasers and thermoelectrics. Understanding how to optimize thermal transport in these systems is critical to their advancement. This optimization will hinge on the detailed understanding of vibrational physics outside of the regime applicable to the phonon gas model. The primary goal of this dissertation is to advance the understanding of vibrational physics in the transition region between fully crystalline and amorphous materials where the PGM begins to break down. Chapter 6 used the lineshape of the Raman spectra as a metric for the nature and behavior of Raman active vibrations with the aim of probing the vibrational physics of disordered and nanoscaled materials. Before that was possible, however, the ideal experimental condition to minimize uncertainties in measurements needed to be selected in Chapter 4 and the origin of the Raman peak asymmetry needed to be ascertained in Chapter 5.

Chapter 4 investigated how properly selecting the experimental condition can minimize uncertainties of linewidth studies. Specifically, the effects of spectral resolution, spatial resolution and noise on uncertainties was tested through selection

of the laser wavelength, grating and integration time. It was found that the relative intensities of the film and substrate peaks was the most important parameter for minimizing uncertainties. Therefore, maximizing the spatial resolution of the system through selection of the laser wavelength is the first priority for minimizing uncertainties. For this reason, the 405 nm laser with the 1800 g/mm (-2) grating was selected for linewidth studies in Chapter 6. The small penetration depth, 60 nm, of the 405 nm laser minimized the Si substrate signal while operating the 1800 g/mm grating in the -2 order reduced the resolution to $0.7 \text{ cm}^{-1}/\text{px}$. Resolution was then found to have a stronger effect on minimizing uncertainties than noise. Therefore, improving the resolution through selection of the grating is the second priority. Finally, noise can be minimized as the third priority through the experimental integration time.

Chapter 5 investigated the origins of the asymmetry of the SiGe Raman peak and the effects of laser heating. Since the asymmetry of the Raman peak was utilized as a metric for the localization of the Raman mode, it was imperative that the origin of the mode be known. Previous studies had found that the asymmetry of the Raman spectra in nanoscaled Si depended on the power density of the probing Raman laser. These studies attributed the observed asymmetry to several phenomena, most notably (1) Fano resonance, (2) inhomogeneous laser heating and (3) an overlap of disorder/surface and bulk-like modes in the spectrum. Using various laser wavelengths and SiGe samples with various film thicknesses and compositions, several hypotheses were tested in Chapter 5. Fano resonance was ruled out, but experimental evidence was not sufficient to determine if the asymmetry originated from a dual mode peak or from inhomogeneous heating. However, inhomogeneous heating was supported by modeling the effect of laser heating using a custom written FEA code. However, replicating the experimental results required increasing the simulated laser power density by a factor of four over experiment. Regardless of which hypothesis is correct, the Raman peak asymmetry

could still be used as a metric for the localization of modes. If the change in asymmetry is due to inhomogeneous heating, then as long as the laser power is low enough to prevent heating, the peak asymmetry results from disorder induced breakdown of selection rules similar to phonon confinement. Alternatively, if the hypothesis of a dual mode peak is correct then the asymmetry can still be used since the asymmetry is caused by the appearance of localized disorder modes in the spectrum. However, to mitigate any unwanted effects from laser heating, the 405 nm laser, which did not affect the asymmetry, was used in the linewidth and asymmetry studies in Chapter 6.

Chapter 6 applied the knowledge gained in Chapters 4 and 5 to measurements of Raman peak linewidths and asymmetries in nanoscaled and disordered SiGe alloys. These measurement were used to investigate the physics of vibrational nature and behavior as material properties were varied. It was found that breaking the periodicity of a crystal influences both the scattering rates and the localization of vibrations. However, different material properties effect the scattering and localization differently. For example, alloying creates scattering sites by introducing randomly spaced impurities masses. Additionally, the alloy disorder breaks the symmetry of the crystal leading to a breakdown of the plane wave nature of the modes, i.e., localization. Dislocations on the other hand only influence scattering rates as the disorder is more strongly affected by the alloying. Furthermore, disorder and nanoscaling influence the temperature dependence of the scattering rates through a change in the anharmonic scattering. Finally, it was found that the localization was not constant with a change in temperature. Since localization reduces thermal conductivity by sequestering thermal energy into finite reions of the material, it is partially responsible for the temperature dependence of the thermal conductivity. These results along with result from various computation studies of thermal physics in disordered materials underscores the importance of understanding not only the behavior (scattering) of vibrations, but also their nature

(localization).

7.2 Suggested Future Studies

The concept of localized modes is relatively new and unexplored in the thermal community. Therefore, while many questions were answered by the work in this dissertation, many were also formed. This section outlines some of the work that could be performed in the future to further investigate the vibrational physics of disordered systems.

- *Assess uncertainty in linewidth measurements including asymmetric modes.* In Chapter 4, simulations of the Raman spectra were performed ignoring the asymmetry of the SiGe peak. While it is speculated that this will not change the trends of the uncertainties, adding an additional fitting parameter will likely lead to an increase in the predicted uncertainties. Additionally, the asymmetry will compete with the linewidth to some extent during a fit changing the Jacobian of the fit and thus fit parameter uncertainties. Therefore, the experimental conditions which minimize uncertainties could be more accurately predicted following this study.
- *Measure the change in asymmetry for high powers using the 405 nm laser.* When the hypothesis that inhomogeneous laser heating caused the Raman peak asymmetry was being tested in Chapter 5, the Raman peak asymmetry was found to be insensitive to the 405 nm laser power. Even though the maximum power densities of the 488 and 405 nm lasers were similar, it is possible that 405 nm absolute power was not high enough to induce changes in the peak asymmetry. Using a high powered 405 nm laser would answer many questions left open in Chapter 5. If the high laser power did induce a change in the peak asymmetry, then the asymmetry is likely due to inhomogeneous

heating. This could be further investigated through changes in the SiGe film thickness since the penetration depth is less than or equal to the film thicknesses, unlike when using the 488 nm laser. On the other hand, if no asymmetry change was observed at high laser power, then it would support the hypothesis of a dual mode peak. Therefore, the asymmetry could be attributed to disorder activated Raman modes.

- *Calculate the Raman tensor of SiGe alloys.* When attempting to use the polarization to separate the signals from the disorder and bulk-like modes in Chapter 5, the symmetry of the disorder modes were unknown. Lattice dynamic or density functional theory (DFT) can be used to calculate the Raman tensor of a material in order to identify properties of the Raman active modes, such as symmetry and depolarization. These would then allow us to know for certain if changing polarization should separate the disorder and bulk-like modes, or if they have the same symmetry. Furthermore, either lattice dynamics or DFT would provide the frequencies of the Raman active modes, which would identify which modes lie near the bulk-like modes in frequency. This would allow for investigations of the change in the number of Raman active modes near the bulk-like modes as a function of disorder level, thereby providing evidence for or against the dual mode peak hypothesis.
- *Use a commercial FEA code to re-simulate the effects of laser heating.* One of the major simplifications of the laser heating FEA simulations performed in Chapter 5, was that the material properties were held constant with temperature. Because a steady state FEA code was used, thermal conductivity, reflectivity and penetration depth could not be adjusted with temperature. This may have been the reason that a factor of four increase in simulated over experimental laser power was necessary to reproduce the experimental results of laser heating tests. However, in non-equilibrium FEA

models, the material properties can be temperature dependent making the model more accurate, thus providing a more conclusive result.

- *Extend studies of size effects on scattering and localization to more thicknesses and compositions.* In the size effects study in Chapter 6, localization increased with film thickness for the size and dislocation series while it decreased for the size effects series. Also, the size effects series only had two data points due to one of the three samples having significantly larger Ge fraction. This left the question of how nanoscaling influences the nature of modes unanswered. However, since the Ge fraction varies by 15% across the growth wafer, it is possible to fill in the gaps of this study without any additional growth. Note that it would be recommended that a 10-20 nm sample be grown. The size investigations could also be extended to different compositions to study the interplay between alloy disorder and size effects. Some of these investigations are planned before submitting the results of Chapter 6 for publication. However, much of the parameter space will be left for future work.
- *Reinvestigate the effects of disorder and size in different alloy systems.* This is the first experimental work where scattering and localization were investigated simultaneously using Raman spectroscopy. The results may, therefore, be specific to the systems investigated. Through investigations of scattering and localization in a wide range of materials, a more complete understanding of vibrational physics and the effect of material properties on the nature and behavior of vibrations can be had. One particular study could be to investigate the effects of ternary alloys. This would begin answering the question of how different types and magnitudes of disorder effect scattering and localization.

An alternative direction would be to study the effects of ordering an alloy. As the order changes, the localization of the modes would also change, but would

this also lead to a change in scattering rates? The scattering rate equations used in the PGM would suggest not, but they were not derived to account for the alloy order parameter. This was the originally intended focus of this dissertation, but growth difficulties made it unachievable in SiGe alloys.

- *Investigate how disorder changes the nature of vibrational modes using lattice dynamics.* No model currently exists to predict the change in vibrational localization with disorder or temperature. However, using lattice dynamics, it is possible to calculate the eigenvector of a model system, which can be used to measure localization. As the properties of a model system change (e.g., composition, order parameter, etc.) the localization of each mode in the system can be monitored using the eigenvectors. Localization in the optical Raman modes can then be correlated to localization at lower frequency acoustic modes, where the majority of thermal transport takes place. These correlations will make the experimental Raman measurements of scattering and localization more influential since they can then be directly related back to thermal properties.

References

- [1] DOLLING, G., AND COWLEY, R. A. The thermodynamic and optical properties of germanium, silicon, diamond and gallium arsenide. *Proceedings of the Physical Society* 88, 2 (1966), 463.
- [2] CAHILL, D. G., AND POHL, R. O. Lattice vibrations and heat transport in crystals and glasses. *Ann. Rev. Phys. Chem.* (1988).
- [3] LEE, S.-M., CAHILL, D. G., AND VENKATASUBRAMANIAN, R. Thermal conductivity of Si-Ge superlattices. *Applied Physics Letters* 70, 22 (1997), 2957–2959.
- [4] BÉRAUD, A., KULDA, J., YONENAGA, I., FORET, M., SALCE, B., AND COURTENS, E. Disorder-induced broadening of transverse acoustic phonons in $\text{Si}_x\text{Ge}_{1-x}$ mixed crystals. *Physica B: Condensed Matter* 350, 1-3 (2004), 254 – 257. Proceedings of the Third European Conference on Neutron Scattering.
- [5] PICCO, A., BONERA, E., GRILLI, E., GUZZI, M., GIAROLA, M., MARIOTTO, G., CHRASTINA, D., AND ISELLA, G. Raman efficiency in SiGe alloys. *Phys. Rev. B* 82 (Sep 2010), 115317.
- [6] AHUJA, R., PERSSON, C., FERREIRA DA SILVA, A., SOUZA DE ALMEIDA, J., MOYSES ARAUJO, C., AND JOHANSSON, B. Optical properties of SiGe alloys. *Journal of Applied Physics* 93, 7 (2003), 3832–3836.
- [7] ASPNES, D., AND STUDNA, A. Dielectric functions and optical parameters of Si, Ge, GaP, GaAs, GaSb, InP, InAs, and InSb from 1.5 to 6.0 eV. *Phys. Rev. B* 27 (Jan 1983), 985–1009.
- [8] ULDRICH, J., AND NEWBERRY, D. *The Next Big Thing Is Really Small: How Nanotechnology Will Change the Future of Your Business*. Crown Business, New York, New York, 2003.
- [9] CHEN, G. *Nanoscale Energy Transport and Conversion: A Parallel Treatment of Electrons, Molecules, Phonons and Photons*. Oxford University Press, New York, New York, 2005.
- [10] PATTON, G., IYER, S., DELAGE, S., TIWARI, S., AND STORK, J. Silicon-germanium base heterojunction bipolar transistors by molecular beam epitaxy. *Electron Device Letters, IEEE* 9, 4 (April 1988), 165–167.

- [11] ASHCROFT, N. W., AND MERMIN, N. D. *Solid State Physics*. Brooks and Cole, Cengage Learning, 1976.
- [12] ALLEN, P. B., FELDMAN, J. L., FABIAN, J., AND WOOTEN, F. Diffusons, locons and propagons: Character of atomic vibrations in amorphous Si. *Philosophical Magazine Part B* 79, 11-12 (1999), 1715–1731.
- [13] ALLEN, P. B., AND FELDMAN, J. L. Thermal conductivity of disordered harmonic solids. *Phys. Rev. B* 48 (Nov 1993), 12581–12588.
- [14] NOROUZZADEH, P., NOZARIASBMARZ, A., KRASINSKI, J. S., AND VASHAEE, D. Thermal conductivity of nanostructured $\text{Si}_x\text{Ge}_{1-x}$ in amorphous limit by molecular dynamics simulation. *Journal of Applied Physics* 117, 21 (2015), –.
- [15] LV, W., AND HENRY, A. S. Non-negligible contributions to thermal conductivity from localized modes in amorphous silicon dioxide. *arXiv 1504* (2015), 03567.
- [16] LV, W., AND HENRY, A. S. Direct calculation of modal contributions to thermal conductivity via green-kubo modal analysis: Crystalline and amorphous silicon. *arXiv 1503* (2015), 08178.
- [17] ALAM, A., CHOUHAN, R. K., AND MOOKERJEE, A. Phonon modes and vibrational entropy of disordered alloys with short-range order: A first-principles calculation. *Phys. Rev. B* 83 (Feb 2011), 054201.
- [18] MOORE, G. Cramming more components onto integrated circuits. *Proceedings of the IEEE* 86, 1 (Jan 1998), 82–85.
- [19] WU, J., SHEN, Y.-L., REINHARDT, K., SZU, H., AND DONG, B. A nanotechnology enhancement to moore’s law. *Applied Computational Intelligence and Soft Computing 2013* (2013), 426962.
- [20] SRINIVASAN, J., ADVE, S., BOSE, P., AND RIVERS, J. The impact of technology scaling on lifetime reliability. In *Dependable Systems and Networks, 2004 International Conference on* (June 2004), pp. 177–186.
- [21] SRINIVASAN, J., ADVE, S., BOSE, P., AND RIVERS, J. Lifetime reliability: toward an architectural solution. *Micro, IEEE* 25, 3 (May 2005), 70–80.
- [22] KRISHNAN, S., GARIMELLA, S. V., CHRYSLER, G., AND MAHAJAN, R. Towards a thermal moore’s law. *Advanced Packaging, IEEE Transactions on* 30, 3 (Aug 2007), 462–474.
- [23] SIEMENS, M. E., LI, Q., YANG, R., NELSON, K. A., ANDERSON, E. H., MURNANE, M. M., AND KAPTEYN, H. C. Quasi-ballistic thermal transport from nanoscale interfaces observed using ultrafast coherent soft x-ray beams. *Nature Materials* 9 (2009), 26–30.

- [24] KOSTEREV, A., WYSOCKI, G., BAKHIRKIN, Y., SO, S., LEWICKI, R., FRASER, M., TITTEL, F., AND CURL, R. Application of quantum cascade lasers to trace gas analysis. *Applied Physics B* 90, 2 (2008), 165–176.
- [25] KHANAL, S., ZHAO, L., RENO, J. L., AND KUMAR, S. Temperature performance of terahertz quantum-cascade lasers with resonant-phonon active-regions. *Journal of Optics* 16, 9 (2014), 094001.
- [26] YAO, Y., HOFFMAN, A. J., AND GMACHL, C. F. Mid-infrared quantum cascade lasers. *Nature Photonics* 6 (2012), 432–439.
- [27] XU, G., AND LI, A. Interface phonons in the active region of a quantum cascade laser. *Phys. Rev. B* 71 (Jun 2005), 235304.
- [28] BAI, Y., SLIVKEN, S., KUBOYA, S., DARVISH, S. R., AND RAZEGHI, M. Quantum cascade lasers that emit more light than heat. *Nature Photonics* 4 (2010), 99–102.
- [29] WILLIAMS, B. S., CALLEBAUT, H., KUMAR, S., HU, Q., AND RENO, J. L. 3.4-THz quantum cascade laser based on longitudinal-optical-phonon scattering for depopulation. *Applied Physics Letters* 82, 7 (2003), 1015–1017.
- [30] HU, Q., WILLIAMS, B. S., KUMAR, S., CALLEBAUT, H., KOHEN, S., AND RENO, J. L. Resonant-phonon-assisted THz quantum-cascade lasers with metal-metal waveguides. *Semiconductor Science and Technology* 20, 7 (2005), S228.
- [31] RATTNER, A. S., AND GARIMELLA, S. Energy harvesting, reuse and upgrade to reduce primary energy usage in the USA. *Energy* 36, 10 (2011), 6172 – 6183.
- [32] VINING, C. B. An inconvenient truth about thermoelectrics. *Nature Materials* 8 (2009), 83–85.
- [33] SALTONSTALL, C. B., DUDA, J. C., HOPKINS, P. E., AND NORRIS, P. M. Assessment of vibrational coupling at solid-SAM interfaces. In *ASME/JSME Thermal Engineering Joint Conference, 8th* (2011), no. AJTEC2011-44313.
- [34] SALTONSTALL, C. B., POLANCO, C. A., DUDA, J. C., GHOSH, A. W., NORRIS, P. M., AND HOPKINS, P. E. Effect of interface adhesion and impurity mass on phonon transport at atomic junctions. *Journal of Applied Physics* 113, 1 (2013), 013516.
- [35] POLANCO, C. A., SALTONSTALL, C. B., NORRIS, P. M., HOPKINS, P. E., AND GHOSH, A. W. Impedance matching of atomic thermal interfaces using primitive block decomposition. *Nanoscale and Microscale Thermophysical Engineering* 17, 3 (2013), 263–279.

- [36] DUDA, J. C., HOPKINS, P. E., SMOYER, J. L., BAUER, M. L., ENGLISH, T. S., SALTONSTALL, C. B., AND NORRIS, P. M. On the assumption of detailed balance in prediction of diffuse transmission probability during interfacial transport. *Nanoscale and Microscale Thermophysical Engineering* 14 (2010), 21–33.
- [37] DUDA, J. C., SALTONSTALL, C. B., NORRIS, P. M., AND HOPKINS, P. E. Assessment and prediction of thermal transport at solid–self-assembled monolayer junctions. *The Journal of Chemical Physics* 134, 9 (2011), 094704.
- [38] SALTONSTALL, C. B., SERRANO, J., NORRIS, P. M., HOPKINS, P. E., AND BEECHEM, T. E. Single element Raman thermometry. *Review of Scientific Instruments* 84, 6 (2013), 064903.
- [39] BAUER, M. L., PHAM, Q. N., SALTONSTALL, C. B., AND NORRIS, P. M. Thermal conductivity of vertically aligned carbon nanotube arrays: Growth conditions and tube inhomogeneity. *Applied Physics Letters* 105, 15 (2014), –.
- [40] BAUER, M. L., SALTONSTALL, C. B., LESEMAN, Z. C., BEECHEM, T. E., HOPKINS, P. E., AND NORRIS, P. M. Thermal conductivity of turbostratic carbon nanofiber networks. *Journal of Heat Transfer* 138 (2016), 061302.
- [41] KITTEL, C. *Introduction to Solid State Physics*. John Wiley and Sons, Inc., 2005.
- [42] SRIVASTAVA, G. P. *The physics of phonons*. Taylor and Francis Group, New York, NY, 1990.
- [43] BROCKHOUSE, B. N. Lattice vibrations in silicon and germanium. *Phys. Rev. Lett.* 2, 6 (Mar 1959), 256–258.
- [44] ESFARJANI, K., CHEN, G., AND STOKES, H. T. Heat transport in silicon from first-principles calculations. *Phys. Rev. B* 84 (Aug 2011), 085204.
- [45] MURPHY-ARMANDO, F., AND FAHY, S. First-principles calculation of alloy scattering in $\text{Ge}_x\text{Si}_{(1-x)}$. *Phys. Rev. Lett.* 97 (Sep 2006), 096606.
- [46] HORI, T., SHIGA, T., AND SHIOMI, J. Phonon transport analysis of silicon germanium alloys using molecular dynamics simulations. *Journal of Applied Physics* 113, 20 (2013), –.
- [47] CHEN, G., AND TIEN, C. L. Thermal conductivities of quantum well structures. *Journal of Thermophysics and Heat Transfer* 7 (1993), 311–318.
- [48] CHEAITO, R., DUDA, J. C., BEECHEM, T. E., HATTAR, K., IHLEFELD, J. F., MEDLIN, D. L., RODRIGUEZ, M. A., CAMPION, M. J., PIEKOS, E. S., AND HOPKINS, P. E. Experimental investigation of size effects on the thermal conductivity of silicon-germanium alloy thin films. *Phys. Rev. Lett.* 109 (Nov 2012), 195901.

- [49] CASIMIR, H. Note on the conduction of heat in crystals. *Physica* 5, 6 (1938), 495 – 500.
- [50] KLEMENS, P. G. The scattering of low-frequency lattice waves by static imperfections. *Proceedings of the Physical Society. Section A* 68, 12 (1955), 1113.
- [51] CALLAWAY, J. Model for lattice thermal conductivity at low temperatures. *Phys. Rev.* 113 (Feb 1959), 1046–1051.
- [52] HOLLAND, M. G. Phonon scattering in semiconductors from thermal conductivity studies. *Phys. Rev.* 134 (Apr 1964), A471–A480.
- [53] WANG, Y., ZACHERL, C. L., SHANG, S., CHEN, L.-Q., AND LIU, Z.-K. Phonon dispersions in random alloys: a method based on special quasi-random structure force constants. *Journal of Physics: Condensed Matter* 23, 48 (2011), 485403.
- [54] MCGAUGHEY, A. J. H., LANDRY, E. S., SELLAN, D. P., AND AMON, C. H. Size-dependent model for thin film and nanowire thermal conductivity. *Applied Physics Letters* 99, 13 (2011), –.
- [55] ZOU, J., AND BALANDIN, A. Phonon heat conduction in a semiconductor nanowire. *Journal of Applied Physics* 89, 5 (2001), 2932–2938.
- [56] ABELES, B. Lattice thermal conductivity of disordered semiconductor alloys at high temperatures. *Phys. Rev.* 131 (Sep 1963), 1906–1911.
- [57] DUDA, J. C., BEECHEM, T. E., SMOYER, J. L., NORRIS, P. M., AND HOPKINS, P. E. Role of dispersion on phononic thermal boundary conductance. *Journal of Applied Physics* 108, 7 (2010), 073515.
- [58] HOPKINS, P. E. Dispersion considerations affecting phonon-mass impurity scattering rates. vol. 1, AIP, p. 041705.
- [59] TAMURA, S.-I. Isotope scattering of dispersive phonons in Ge. *Phys. Rev. B* 27 (Jan 1983), 858–866.
- [60] GORDIZ, K., AND HENRY, A. Phonon transport at interfaces: Determining the correct modes of vibration. *Journal of Applied Physics* 119, 1 (2016).
- [61] ZOU, J., AND BALANDIN, A. Excess heat removal from nanoscale devices. *Quantum Confinement VI: Nanostructured Materials and Devices: Proceedings of the International Symposium 2001* (2001), 70.
- [62] GOODSON, K. E., , AND JU, Y. S. Heat conduction in novel electronic films. *Annual Review of Materials Science* 29, 1 (1999), 261–293.

- [63] BALANDIN, A., AND WANG, K. L. Significant decrease of the lattice thermal conductivity due to phonon confinement in a free-standing semiconductor quantum well. *Phys. Rev. B* 58 (Jul 1998), 1544–1549.
- [64] PONOMAREVA, I., SRIVASTAVA, D., AND MENON*, M. Thermal conductivity in thin silicon nanowires: Phonon confinement effect. *Nano Letters* 7, 5 (2007), 1155–1159. PMID: 17394370.
- [65] BALANDIN, A., AND WANG, K. L. Effect of phonon confinement on the thermoelectric figure of merit of quantum wells. *Journal of Applied Physics* 84, 11 (1998), 6149–6153.
- [66] TIAN, Z., ESFARJANI, K., SHIOMI, J., HENRY, A. S., AND CHEN, G. On the importance of optical phonons to thermal conductivity in nanostructures. *Applied Physics Letters* 99, 5 (2011), –.
- [67] SCHWAB, K., HENRIKSEN, E., WORLOCK, J., AND ROUKES, M. L. Measurement of the quantum of thermal conductance. *Nature* 404, 6781 (2000), 974–977.
- [68] SOOD, A. K., MENÉNDEZ, J., CARDONA, M., AND PLOOG, K. Interface vibrational modes in GaAs-AlAs superlattices. *Phys. Rev. Lett.* 54 (May 1985), 2115–2118.
- [69] YU, S., KIM, K. W., STROSCIO, M. A., IAFRATE, G. J., SUN, J.-P., AND HADDAD, G. I. Transfer matrix method for interface optical-phonon modes in multiple-interface heterostructure systems. *Journal of Applied Physics* 82, 7 (1997), 3363–3367.
- [70] KOSTOV, K. L., POLZIN, S., SAHA, S. K., BROVKO, O., STEPANYUK, V., AND WIDDRA, W. Surface-phonon dispersion of a NiO(100) thin film. *Phys. Rev. B* 87 (Jun 2013), 235416.
- [71] ESTREICHER, S. K., GIBBONS, T. M., KANG, B., AND BEBEK, M. B. Phonons and defects in semiconductors and nanostructures: Phonon trapping, phonon scattering, and heat flow at heterojunctions. *Journal of Applied Physics* 115, 1 (2014), –.
- [72] FERAIN, I., COLINGE, C. A., AND COLINGE, J.-P. Multigate transistors as the future of classical metal-oxide-semiconductor field-effect transistors. *Nature* 479, 7373 (2011), 310–316.
- [73] KITTEL, C. Interpretation of the thermal conductivity of glasses. *Phys. Rev.* 75 (Mar 1949), 972–974.
- [74] DUDA, J. C., ENGLISH, T. S., SOFFA, W. A., JORDAN, D. A., AND NORRIS, P. M. Controlling thermal conductivity of alloys via atomic ordering. *J. Heat Transfer* 134 (2011), 014501.

- [75] CAHILL, D. G., WATSON, S. K., AND POHL, R. O. Lower limit to the thermal conductivity of disordered crystals. *Phys. Rev. B* 46 (Sep 1992), 6131–6140.
- [76] WANG, Z., AND MINGO, N. Diameter dependence of sige nanowire thermal conductivity. *Applied Physics Letters* 97, 10 (2010), –.
- [77] ASHEGHI, M., KURABAYASHI, K., KASNAVI, R., AND GOODSON, K. E. Thermal conduction in doped single-crystal silicon films. *Journal of Applied Physics* 91, 8 (2002), 5079–5088.
- [78] ESTREICHER, S. K., GIBBONS, T. M., AND BEBEK, M. B. Thermal phonons and defects in semiconductors: The physical reason why defects reduce heat flow, and how to control it. *Journal of Applied Physics* 117, 11 (2015), –.
- [79] WHITEAKER, K. L., ROBINSON, I. K., VAN NOSTRAND, J. E., AND CAHILL, D. G. Compositional ordering in SiGe alloy thin films. *Phys. Rev. B* 57 (May 1998), 12410–12420.
- [80] LOCKWOOD, D., RAJAN, K., FENTON, E., BARIBEAU, J.-M., AND DENHOFF, M. Ordering in $\text{Si}_{1-x}\text{Ge}_x$ crystals. *Solid State Communications* 61, 8 (1987), 465 – 467.
- [81] WANG, H., STRAIT, J. H., GEORGE, P. A., SHIVARAMAN, S., SHIELDS, V. B., CHANDRASHEKHAR, M., HWANG, J., RANA, F., SPENCER, M. G., RUIZ-VARGAS, C. S., AND PARK, J. Ultrafast relaxation dynamics of hot optical phonons in graphene. *Applied Physics Letters* 96, 8 (2010), 081917.
- [82] CAHILL, D. G., AND POHL, R. Heat flow and lattice vibrations in glasses. *Solid State Communications* 70, 10 (1989), 927 – 930.
- [83] EUCKEN, A. über die temperaturabhängigkeit der wärmeleitfähigkeit fester nichtmetalle. *Annalen der Physik* 339, 2 (1911), 185–221.
- [84] SLACK, G. A. The thermal conductivity of nonmetallic crystals. vol. 34 of *Solid State Physics*. Academic Press, 1979, pp. 1 – 71.
- [85] EINSTEIN, A. Elementare betrachtungen über die thermische molekularbewegung in festen körpern [AdP 35, 679 (1911)]. *Ann. Phys.* 14 (2005), 408–424.
- [86] ZELLER, R. C., AND POHL, R. O. Thermal conductivity and specific heat of noncrystalline solids. *Phys. Rev. B* 4 (Sep 1971), 2029–2041.
- [87] ANDERSON, P. W., HALPERIN, B. I., AND C. M. VARMA. Anomalous low-temperature thermal properties of glasses and spin glasses. *Philosophical Magazine* 25, 1 (1972), 1–9.
- [88] GRANNAN, E. R., RANDEIRA, M., AND SETHNA, J. P. Low-temperature properties of a model glass. *Phys. Rev. Lett.* 60 (Apr 1988), 1402–1405.

- [89] ALLEN, P. B., AND FELDMAN, J. L. Thermal conductivity of glasses: Theory and application to amorphous Si. *Phys. Rev. Lett.* *62* (Feb 1989), 645–648.
- [90] FELDMAN, J. L., KLUGE, M. D., ALLEN, P. B., AND WOOTEN, F. Thermal conductivity and localization in glasses: Numerical study of a model of amorphous silicon. *Phys. Rev. B* *48* (Nov 1993), 12589–12602.
- [91] YAMAMOTO, T., AND WATANABE, K. Nonequilibrium green's function approach to phonon transport in defective carbon nanotubes. *Phys. Rev. Lett.* *96* (Jun 2006), 255503.
- [92] BEECHEM, T. E., AND SERRANO, J. R. Raman thermometry of micro devices: Comparing methods to minimize error. *Spectroscopy* *33* (2011), 26.
- [93] LONG, D. A. *The Raman Effect: A Unified Treatment of the Theory of Raman Scattering by Molecules*. John Wiley and Sons, 2002.
- [94] KONIGSTEIN, J. A. *Introduction to the Theory of the Raman Effect*. D. Reidel Publishing Company, 1972.
- [95] HARRIS, D. C., AND BERTOLUCCI, M. D. *Symmetry and Spectroscopy: An Introduction to Vibrational and Electronic Spectroscopy*. Dover, 1978.
- [96] DRESSELHAUS, M. S. *Group Theory, Application to the Physics of Matter*. Springer, 2008.
- [97] COHEN-TANNOUJJI, C., DIU, B., AND LALOË, F. *Quantum Mechanics*. John Wiley & Sons, Ltd., 1977.
- [98] FERRARI, A. C., AND ROBERTSON, J. Interpretation of raman spectra of disordered and amorphous carbon. *Phys. Rev. B* *61* (May 2000), 14095–14107.
- [99] FERRARI, A. C. Raman spectroscopy of graphene and graphite: Disorder, electron-phonon coupling, doping and nonadiabatic effects. *Solid State Communications* *143*, 1-2 (2007), 47 – 57. Exploring grapheneRecent research advances.
- [100] RICHTER, H., WANG, Z., AND LEY, L. The one phonon Raman spectrum in microcrystalline silicon. *Solid State Communications* *39*, 5 (1981), 625 – 629.
- [101] CAMPBELL, I., AND FAUCHET, P. The effects of microcrystal size and shape on the one phonon Raman spectra of crystalline semiconductors. *Solid State Communications* *58*, 10 (1986), 739 – 741.
- [102] FAUCHET, P. M., AND CAMPBELL, I. H. Raman spectroscopy of low-dimensional semiconductors. *Critical Reviews in Solid State & Materials Sciences* *14* (Jan. 1988), 79.

- [103] ZHANG, P., FENG, Y., ANTHONY, R., KORTSHAGEN, U., CONIBEER, G., AND HUANG, S. Size-dependent evolution of phonon confinement in colloidal Si nanoparticles. *Journal of Raman Spectroscopy* 46, 11 (2015), 1110–1116.
- [104] LEJON, C., AND OSTERLUND, L. Influence of phonon confinement, surface stress, and zirconium doping on the Raman vibrational properties of anatase TiO₂ nanoparticles. *Journal of Raman Spectroscopy* 42, 11 (2011), 2026–2035.
- [105] FUKATA, N., SATO, K., MITOME, M., BANDO, Y., SEKIGUCHI, T., KIRKHAM, M., HONG, J.-I., WANG, Z. L., AND SNYDER, R. L. Doping and Raman characterization of boron and phosphorus atoms in germanium nanowires. *ACS Nano* 4, 7 (2010), 3807–3816. PMID: 20565120.
- [106] ROODENKO, K., GOLDTHORPE, I. A., MCINTYRE, P. C., AND CHABAL, Y. J. Modified phonon confinement model for Raman spectroscopy of nanostructured materials. *Phys. Rev. B* 82 (Sep 2010), 115210.
- [107] OSSWALD, S., MOCHALIN, V. N., HAVEL, M., YUSHIN, G., AND GOGOTSI, Y. Phonon confinement effects in the Raman spectrum of nanodiamond. *Phys. Rev. B* 80 (Aug 2009), 075419.
- [108] ARORA, A. K., RAJALAKSHMI, M., RAVINDRAN, T. R., AND SIVASUBRAMANIAN, V. Raman spectroscopy of optical phonon confinement in nanostructured materials. *Journal of Raman Spectroscopy* 38, 6 (2007), 604–617.
- [109] GOUADEC, G., AND COLOMBAN, P. Raman spectroscopy of nanomaterials: How spectra relate to disorder, particle size and mechanical properties. *Progress in Crystal Growth and Characterization of Materials* 53, 1 (2007), 1–56.
- [110] FARACI, G., GIBILISCO, S., RUSSO, P., PENNISI, A. R., AND LA ROSA, S. Modified Raman confinement model for Si nanocrystals. *Phys. Rev. B* 73 (Jan 2006), 033307.
- [111] ADU, K. W., GUTIERREZ, H. R., KIM, U. J., SUMANASEKERA, G. U., AND EKLUND, P. C. Confined phonons in Si nanowires. *Nano Letters* 5, 3 (2005), 409–414. PMID: 15755085.
- [112] YANG, Y., WU, X., HUANG, G., HU, D., AND SIU, G. Confinement effect of optical phonons in SiGe alloy nanocrystals. *Physics Letters A* 338, 3-5 (2005), 379 – 384.
- [113] OLIVARES, J., MARTÍN, P., RODRÍGUEZ, A., SANGRADOR, J., JIMEÍNEZ, J., AND RODRÍGUEZ, T. Raman spectroscopy study of amorphous SiGe films deposited by low pressure chemical vapor deposition and polycrystalline SiGe films obtained by solid-phase crystallization. *Thin Solid Films* 358, 1-2 (2000), 56–61.

- [114] BRODSKY, M., AND CARDONA, M. Local order as determined by electronic and vibrational spectroscopy: Amorphous semiconductors. *Journal of Non-Crystalline Solids* 31, 1-2 (1978), 81 – 108. Proceedings of the Topical Conference on Atomic Scale Structure of Amorphous Solids.
- [115] PARAYANTHAL, P., AND POLLAK, F. H. Raman scattering in alloy semiconductors: "spatial correlation" model. *Phys. Rev. Lett.* 52 (May 1984), 1822–1825.
- [116] TIONG, K. K., AMIRTHARAJ, P. M., POLLAK, F. H., AND ASPNES, D. E. Effects of As+ ion implantation on the Raman spectra of GaAs: "spatial correlation" interpretation. *Applied Physics Letters* 44, 1 (1984), 122–124.
- [117] BRAFMAN, O., AND MANOR, R. Raman line asymmetry in alloys and in ion-implanted polar crystals. *Phys. Rev. B* 51 (Mar 1995), 6940–6946.
- [118] KASH, J. A., HVAM, J. M., TSANG, J. C., AND KUECH, T. F. Localization and wave-vector conservation for optical phonons in $\text{Al}_x\text{Ga}_{(1-x)}\text{As}$ and thin layers of GaAs. *Phys. Rev. B* 38 (Sep 1988), 5776–5779.
- [119] MCGLINN, T. C., KRABACH, T. N., KLEIN, M. V., BAJOR, G., GREENE, J. E., KRAMER, B., BARNETT, S. A., LASTRAS, A., AND GORBATKIN, S. Raman scattering and optical-absorption studies of the metastable alloy system $\text{GaAs}_x\text{Sb}_{(1-x)}$. *Phys. Rev. B* 33 (Jun 1986), 8396–8401.
- [120] ALONSO, M. I., AND WINER, K. Raman spectra of c- $\text{Si}_{(1-x)}\text{Ge}_x$ alloys. *Phys. Rev. B* 39 (May 1989), 10056–10062.
- [121] VASIN, A. S., VIKHROVA, O. V., AND VASILEVSKIY, M. I. Effects of alloy disorder and confinement on phonon modes and Raman scattering in $\text{Si}_x\text{Ge}_{(1-x)}$ nanocrystals: A microscopic modeling. *Journal of Applied Physics* 115, 14 (2014).
- [122] HOWIE, R. T., MAGDĂU, I. B., GONCHAROV, A. F., ACKLAND, G. J., AND GREGORYANZ, E. Phonon localization by mass disorder in dense hydrogen-deuterium binary alloy. *Phys. Rev. Lett.* 113 (Oct 2014), 175501.
- [123] NAKAMURA, K., AND KITAJIMA, M. Ion-irradiation effects on the phonon correlation length of graphite studied by Raman spectroscopy. *Phys. Rev. B* 45 (Jan 1992), 78–82.
- [124] JIMÉNEZ, J., WOLF, I. D., AND LANDESMAN, J. P. *Microprobe Characterizations of Optoelectronic Materials*. Taylor and Francis Books, Inc, 2003, ch. Micro-Raman Spectroscopy of Semiconductors: Principles and Applications, pp. 89–198.
- [125] JESPERSEN, T. S. *Raman Scattering in Carbon Nanotubes*. PhD thesis, University of Copenhagen, 2003.

- [126] DRESSELHAUS, M., DRESSELHAUS, G., SAITO, R., AND JORIO, A. Raman spectroscopy of carbon nanotubes. *Physics Reports* 409, 2 (2005), 47 – 99.
- [127] ARAUJO, P., PESCE, P., DRESSELHAUS, M., SATO, K., SAITO, R., AND JORIO, A. Resonance Raman spectroscopy of the radial breathing modes in carbon nanotubes. *Physica E: Low-dimensional Systems and Nanostructures* 42, 5 (2010), 1251 – 1261.
- [128] RENUCCI, J. B., TYTE, R. N., AND CARDONA, M. Resonant Raman scattering in silicon. *Phys. Rev. B* 11 (May 1975), 3885–3895.
- [129] PICCO, A. *Resonance Effects in the Raman Analysis of SiGe Nanostructures*. PhD thesis, Università Degli Studi Di Milano-Bicocca, 2011.
- [130] BEECHEM, T., GRAHAM, S., KEARNEY, S. P., PHINNEY, L. M., AND SERRANO, J. R. Invited article: Simultaneous mapping of temperature and stress in microdevices using micro-raman spectroscopy. *Review of Scientific Instruments* 78, 6 (2007), 061301.
- [131] BURKE, H. H., AND HERMAN, I. P. Temperature dependence of Raman scattering in $\text{Ge}_{(1-x)}\text{Si}_x$ alloys. *Phys. Rev. B* 48 (Nov 1993), 15016–15024.
- [132] CUSCÓ, R., ALARCÓN-LLADÓ, E., IBÁÑEZ, J., ARTÚS, L., JIMÉNEZ, J., WANG, B., AND CALLAHAN, M. J. Temperature dependence of raman scattering in ZnO. *Phys. Rev. B* 75 (Apr 2007), 165202.
- [133] ANAND, S., VERMA, P., JAIN, K., AND ABBI, S. Temperature dependence of optical phonon lifetimes in ZnSe. *Physica B: Condensed Matter* 226, 4 (1996), 331 – 337.
- [134] HART, T. R., AGGARWAL, R. L., AND LAX, B. Temperature dependence of Raman scattering in silicon. *Phys. Rev. B* 1 (Jan 1970), 638–642.
- [135] MENÉNDEZ, J., AND CARDONA, M. Temperature dependence of the first-order Raman scattering by phonons in Si, Ge, and α -S: Anharmonic effects. *Phys. Rev. B* 29 (Feb 1984), 2051–2059.
- [136] JIMÉNEZ, J., MARTÍN, E., TORRES, A., AND LANDESMAN, J. P. Temperature dependence of the Raman spectrum of $\text{Al}_x\text{Ga}_{(1-x)}\text{As}$ ternary alloys. *Phys. Rev. B* 58 (Oct 1998), 10463–10469.
- [137] LUCAZEAU, G. Effect of pressure and temperature on Raman spectra of solids: anharmonicity. *Journal of Raman Spectroscopy* 34, 7-8 (2003), 478–496.
- [138] PEROVA, T. S., WASYLUK, J., LYUTOVICH, K., KASPER, E., OEHME, M., RODE, K., AND WALDRON, A. Composition and strain in thin $\text{Si}_{(1-x)}\text{Ge}_x$ virtual substrates measured by micro-raman spectroscopy and x-ray diffraction. *Journal of Applied Physics* 109, 3 (2011), –.

- [139] FOURNIER-LUPIEN, J.-H., MUKHERJEE, S., WIRTHS, S., PIPPEL, E., HAYAZAWA, N., MUSSLER, G., HARTMANN, J. M., DESJARDINS, P., BUCA, D., AND MOUTANABBIR, O. Strain and composition effects on Raman vibrational modes of silicon-germanium-tin ternary alloys. *Applied Physics Letters* 103, 26 (2013), –.
- [140] TSANG, J. C., MOONEY, P. M., DACOL, F., AND CHU, J. O. Measurements of alloy composition and strain in thin $\text{Ge}_x\text{Si}_{(1-x)}$ layers. *Journal of Applied Physics* 75, 12 (1994), 8098–8108.
- [141] MAITI, C. K., BERA, L. K., MAIKAP, S., RAY, S. K., CHAKRABARTI, N. B., KESAVAN, R., AND KUMAR, V. Growth of silicon-germanium alloy layers. *Defence Science Journal* 50 (2000), 299–315.
- [142] PAUL, D. J. Si/SiGe heterostructures: from material and physics to devices and circuits. *Semiconductor Science and Technology* 19, 10 (2004), R75.
- [143] BEECHEM, T. E. *Metrology of GaN Electronics Using Micro-Raman Spectroscopy*. PhD thesis, Georgia Institute of Technology, 2008.
- [144] DI BARTOLO, B. *Optical Interactions in Solids*. John Wiley and Sons, Inc., 1968.
- [145] KLEMENS, P. G. Anharmonic decay of optical phonons. *Phys. Rev.* 148 (Aug 1966), 845–848.
- [146] BALKANSKI, M., WALLIS, R. F., AND HARO, E. Anharmonic effects in light scattering due to optical phonons in silicon. *Phys. Rev. B* 28 (Aug 1983), 1928–1934.
- [147] POSENER, D. W. The shape of spectral lines: Tables of the Voigt profile. *Australian Journal of Physics* 12 (1959), 184.
- [148] FANO, U. Effects of configuration interaction on intensities and phase shifts. *Phys. Rev.* 124 (Dec 1961), 1866–1878.
- [149] CERDEIRA, F., FJELDLY, T. A., AND CARDONA, M. Interaction between electronic and vibronic Raman scattering in heavily doped silicon. *Solid State Communications* 13, 3 (1973), 325 – 328.
- [150] PUSEP, Y. A., RODRIGUES, A. D., BORRERO-GONZLEZ, L. J., ACQUAROLI, L. N., URTEAGA, R., ARCE, R. D., KOROPECKI, R. R., TIRADO, M., AND COMEDI, D. Fano resonance in heavily doped porous silicon. *Journal of Raman Spectroscopy* 42, 6 (2011), 1405–1407.
- [151] GEURTS, J. Analysis of band bending at iiii semiconductor interfaces by Raman spectroscopy. *Surface science reports* 18 (1993), 1–89.

- [152] HOLTZ, M., DUNCAN, W. M., ZOLLNER, S., AND LIU, R. Visible and ultraviolet Raman scattering studies of $\text{Si}_{(1-x)}\text{Ge}_x$ alloys. *Journal of Applied Physics* 88, 5 (2000), 2523–2528.
- [153] BORN, M., AND WOLF, E. *Principles of Optics: Electromagnetic Theory of Propagation, Interference and Diffraction of Light*. Cambridge University Press, 1999.
- [154] ZHENG, Y., YI, S., JIAN-LIN, L., BO, Y., ZHUANG-XIONG, H., LIN, P., YOU-DOU, Z., AND KANG-LONG, W. Strain and phonon confinement in self-assembled Ge quantum dot superlattices. *Chinese Physics Letters* 20, 11 (2003), 2001.
- [155] ADU, K. W., WILLIAMS, M. D., REBER, M., JAYASINGHA, R., GUTIERREZ, H. R., AND SUMANASEKERA, G. U. Probing phonons in nonpolar semiconducting nanowires with raman spectroscopy. *Journal of Nanotechnology* 2012 (2012).
- [156] NEMANICH, R. J., SOLIN, S. A., AND MARTIN, R. M. Light scattering study of boron nitride microcrystals. *Phys. Rev. B* 23 (Jun 1981), 6348–6356.
- [157] CHAIGNEAU, M., PICARDI, G., GIRARD, H., ARNAULT, J.-C., AND OSSIKOVSKI, R. Laser heating versus phonon confinement effect in the raman spectra of diamond nanoparticles. *Journal of Nanoparticle Research* 14, 6 (2012).
- [158] SOOD, A. K. Phonons in semiconductor superlattices. *Defence Science Journal* 39, 4 (Oct 1989), 411–423.
- [159] PISCANEC, S., CANTORO, M., FERRARI, A. C., ZAPIEN, J. A., LIFSHITZ, Y., LEE, S. T., HOFMANN, S., AND ROBERTSON, J. Raman spectroscopy of silicon nanowires. *Phys. Rev. B* 68 (Dec 2003), 241312.
- [160] ADU, K., XIONG, Q., GUTIERREZ, H., CHEN, G., AND EKLUND, P. Raman scattering as a probe of phonon confinement and surface optical modes in semiconducting nanowires. *Applied Physics A* 85, 3 (2006), 287–297.
- [161] ADU, K. W., GUTIÉRREZ, H. R., KIM, U. J., AND EKLUND, P. C. Inhomogeneous laser heating and phonon confinement in silicon nanowires: A micro-Raman scattering study. *Phys. Rev. B* 73 (Apr 2006), 155333.
- [162] NIKOLENKO, A. S. Laser heating effect on Raman spectra of Si nanocrystals embedded into SiO_x matrix. *Semiconductor Physics, Quantum Electronics and Optoelectronics* 16 (2013), 86–90.
- [163] FARACI, G., GIBILISCO, S., AND PENNISI, A. R. Superheating of silicon nanocrystals observed by Raman spectroscopy. *Physics Letters A* 373, 41 (2009), 3779 – 3782.

- [164] GIBILISCO, S., FARACI, G., PENNISI, A., AND IRRERA, A. Laser induced heating of Si nanocrystals. *Journal of Non-Crystalline Solids* 356, 3740 (2010), 1948 – 1950. Joint Conferences on Advanced Materials: Functional and Nanonstructured Materials FNMA09; Intermolecular and Magnetic Interactions in Matter IMIM09.
- [165] SAXENA, S. K., BORAH, R., KUMAR, V., RAI, H. M., LATE, R., SATHE, V., KUMAR, A., SAGDEO, P. R., AND KUMAR, R. Raman spectroscopy for study of interplay between phonon confinement and fano effect in silicon nanowires. *Journal of Raman Spectroscopy early view* (2015).
- [166] GUPTA, R., XIONG, Q., ADU, C. K., KIM, U. J., AND EKLUND, P. C. Laser-induced Fano resonance scattering in silicon nanowires. *Nano Letters* 3, 5 (2003), 627–631.
- [167] MAGIDSON, V., AND BESERMAN, R. Fano-type interference in the Raman spectrum of photoexcited Si. *Phys. Rev. B* 66 (Nov 2002), 195206.
- [168] KUMAR, R., SHUKLA, A., MAVI, H., AND VANKAR, V. Size-dependent fano interaction in the laser-etched silicon nanostructures. *Nanoscale Research Letters* 3 (2008), 105–108.
- [169] SHANKS, H. R., MAYCOCK, P. D., SIDLES, P. H., AND DANIELSON, G. C. Thermal conductivity of silicon from 300 to 1400k. *Phys. Rev.* 130 (Jun 1963), 1743–1748.
- [170] POP, E., SINHA, S., AND GOODSON, K. E. Heat generation and transport in nanometer-scale transistors. *Proceedings of the IEEE* 94, 8 (Aug 2006), 1587–1601.
- [171] POMEROY, J. W., KUBALL, M., UREN, M. J., AND MARTIN, T. Direct optical measurement of hot-phonons in active algan/gan devices. *physica status solidi (b)* 245, 5 (2008), 910–912.
- [172] TEMPLE, P. A., AND HATHAWAY, C. E. Multiphonon raman spectrum of silicon. *Phys. Rev. B* 7 (Apr 1973), 3685–3697.
- [173] KLAR, P., LIDORIKIS, E., ECKMANN, A., VERZHBITSKIY, I. A., FERRARI, A. C., AND CASIRAGHI, C. Raman scattering efficiency of graphene. *Phys. Rev. B* 87 (May 2013), 205435.
- [174] LARKIN, J. M. *Vibrational Mode Properties of Disordered Solids from High-Performance Atomistic Simulations and Calculations*. PhD thesis, Carnegie Mellon Univerisity, 2013.
- [175] SHIGA, T., HORI, T., AND SHIOMI, J. Influence of mass contrast in alloy phonon scattering. *Japanese Journal of Applied Physics* 53, 2 (2014), 021802.

- [176] XIA, H., HE, Y. L., WANG, L. C., ZHANG, W., LIU, X. N., ZHANG, X. K., FENG, D., AND JACKSON, H. E. Phonon mode study of Si nanocrystals using micro-Raman spectroscopy. *Journal of Applied Physics* 78, 11 (1995), 6705–6708.
- [177] EBERL, K., WEGSCHEIDER, W., SCHORER, R., AND ABSTREITER, G. Microscopic symmetry properties of (001) Si/Ge monolayer superlattices. *Phys. Rev. B* 43 (Feb 1991), 5188–5191.
- [178] BEECHEM, T., AND GRAHAM, S. Temperature and doping dependence of phonon lifetimes and decay pathways in GaN. *Journal of Applied Physics* 103, 9 (2008), –.
- [179] KASSIM, J., NOLPH, C., JAMET, M., REINKE, P., AND FLORO, J. $\text{Ge}_{(1-x)}\text{Mn}_x$ heteroepitaxial quantum dots: Growth, morphology, and magnetism. *Journal of Applied Physics* 113, 7 (2013), 073910.
- [180] WATKINS, T. R., CAVIN, O. B., HUBBARD, C. R., MATLOCK, B., AND ENGLAND, R. D. Considerations regarding the alignment of diffractometers for residual stress analysis. *Rigaku Journal* 23, 1 (2006), 52.
- [181] HARTMANN, J. M., GALLAS, B., FERGUSON, R., FERNÁNDEZ, J., ZHANG, J., AND HARRIS, J. J. Gas-source molecular beam epitaxy of SiGe virtual substrates: I. growth kinetics and doping. *Semiconductor Science and Technology* 15, 4 (2000), 362.
- [182] ZAUMSEIL, P. A fast x-ray method to determine Ge content and relaxation of partly relaxed $\text{Si}_{(1-x)}\text{Ge}_x$ layers on silicon substrates. *physica status solidi (a)* 141, 1 (1994), 155–161.
- [183] HIRTH, J., AND LOTHE, J. *Theory of dislocations*. New York McGraw-Hill, 1967.
- [184] GALE, J. D., AND ROHL, A. L. The general utility lattice program (GULP). *Molecular Simulation* 5 (2003), 291–341.